THE UNIVERSITY OF TOKYO

Search for UHECR sources considering the deflection by the galactic magnetic field
銀河磁場偏向を考慮した最高エネルギー宇宙線起源の探索

A DISSERTATION SUBMITTED TO
THE PHYSICAL SCIENCES
IN CANDIDACY FOR THE DEGREE OF
DOCTOR OF SCIENCE

DEPARTMENT OF THE SCHOOL OF SCIENCE

BY
RYO HIGUCHI　(樋口 諒)

TOKYO, JAPAN
DECEMBER 2021

ABSTRACT

Ultrahigh-energy cosmic-ray (UHECR) anisotropies are said to correlate with the distribution of UHECR sources. Many studies have investigated the association between the arrival directions of UHECR events and their source candidates. Ultrahigh-energy cosmic-ray (UHECR) anisotropies are said to correlate with the distribution of UHECR sources. Many studies have investigated the association between the arrival directions of UHECR events and their source candidates. If we assume the steady sources for the UHECR origin, it is a reasonable way to assume the anisotropic fraction $f_{\rm ani}$ (which is defined as a fraction of observed UHECR events due to the assumed sources) and the isotropic fraction of UHECRs. A maximum-likelihood analysis with assumption of the anisotropic fraction $f_{\rm ani}$ and separation angular scale θ (which is defined as the mean angular separation between UHECRs and their assumed origins) is one of the commonly used parameter estimations (Abreu et al. 2010; Aab et al. 2018; Abbasi et al. 2018). In these previous parameter estimations, they assume the model CR flux pattern expected from the assumed source model and search the best-fit parameter $(f_{\rm ani}, \theta)$. In a maximum-likelihood analysis with an assumption of a starburst galaxy (SBG) source model, the Auger experiment derived the best-fit parameters of $(f_{\rm ani}, \theta) = (9.7\%, 12.9\,{\rm deg})$ and suggested that the nearby SBGs could be possible UHECR sources (Aab et al. 2018, the SBG model). The Telescope Array (TA) experiment also involved the same analysis for the UHECR events observed in the north sky and suggested that the result is consistent with the report obtained from the Auger experiment (Abbasi et al. 2018). These studies proposed that the SBG model is an interesting choice for the source model of UHECRs.

In previous parameter estimations, however, the deflection caused by magnetic fields is approximated to a Gaussian-like scattering, and the coherent deflection caused by the structure of the galactic magnetic field (GMF) is not considered.

In this study, I investigated the bias created due to the coherent deflection caused by the GMF (the GMF bias) using a known GMF model. I also developed a new analysis technique to reduce the GMF bias and applied it to the observational datasets obtained through the Auger and TA experiments.

I first generated mock UHECR datasets assuming the SBG model, a regular component of the GMF model (Jansson & Farrar 2012a,b, JF12), the observed energy spectrum, the mass composition, and the sky coverage of each experiment. I have conducted the maximum-likelihood analysis in the same manner as previous parameter estimations. I found that in the previous parameter estimations performed by Aab et al. (2018) and Abbasi et al. (2018), the true value $(f_{\rm ani}^{\rm true}, \theta^{\rm true})$ cannot be correctly estimated. Particularly, in south-sky datasets, any true value of $f_{\rm ani}^{\rm true}$ reproduces the best-fit parameter close to the result of Aab et al. (2018). Even if the SBG model is correct, it has been found that a strongly biased result is obtained if the GMF bias is ignored.

Then, I developed a new technique to reduce the GMF bias with consideration of cosmic ray (CR) flux patterns through the GMF. In this technique, I assume a dependence of the CR flux pattern on the rigidity of each UHECR event. To take the unknown event-by-event mass into account, I introduced a weighted likelihood according to the mass composition determined from the Auger observations. Using the mock datasets, I found that the new technique can significantly reduce the GMF bias in the parameter estimation. Through a comparison of the test statistics (TS), I also found that the new technique can determine the source models in a certain parameter space $(f_{\rm ani}^{\rm true}, \theta^{\rm true})$. I then apply the new technique to the observational datasets from the TA and Auger experiments and obtain the observational test statistics $TS_{\rm obs}$. Because the $TS_{\rm obs}$ values are consistent with the isotropic assumption over the parameter space, I estimated the 95% exclusion region of the SBG models of Aab et al. (2018) from the observational datasets obtained from the TA and Auger experiments. For example, $\theta < 12$ (37) deg at $f_{\rm ani} = 20\%$ (100%) and $\theta < 20$ (45) deg at $f_{\rm ani} = 20\%$ (100%) are excluded from the TA and Auger data, respectively.

As extensions of the TA and Auger experiments and next-generation plans, UHECR observations with large statistics and high-mass resolution are planned. For prospects, I execute the new technique with an assumption of a limited event-by-event mass resolution $\Delta\ln(A)$ (Method 3) and estimate the necessary number of events N and mass resolution $\Delta\ln(A)$ to separate the isotropic and SBG models. I concluded that we need more than 4000 events all sky and high-mass resolution with $\Delta\ln(A) < 0.3$

to separate the isotropic and SBG models at $(f_{\rm ani}^{\rm true}, \theta^{\rm true}) = (20\%, 30\ {\rm deg})$. Thus the higher event-by-event mass resolution observation will take an important role in future UHECR observations.

Although this study is applied to a specific set of assumptions, the technique is applicable for any model and can be updated based on future observations. The techniques developed in this study and the future observations will reveal the origin of UHECRs.

TABLE OF CONTENTS

CHAPTER 1
OUTLINE OF THIS STUDY

In this chapter, I introduce the motivation and the goals for this study.

Cosmic rays (CRs) are nuclei that come throughout the universe. Specifically, it is known that extremely high-energy CRs have been observed whose energies are around 10^{20} eV. We call these ultrahigh-energy cosmic rays (UHECRs). UHECRs have been said to be related to the high-energy objects or phenomena that exist in the universe. Although many candidates and scenarios for these have been suggested, no observational evidence has been found to support them. Understanding the origin of UHECRs is important not only for astronomical interests but also for a new kind of physics that goes beyond the standard model and acceleration mechanisms whose energies exceed the maximum energy that human beings can realize.

Today, the Telescope Array (TA) experiment and the Auger experiment provide the leading UHECR observations in the northern and southern hemispheres, respectively. The distribution of the reported UHECR arrival directions indicates that the UHECRs come from specific regions in the sky. We call these UHECR anisotropies, which have been said to be correlated with the distributions of UHECR origins.

Many studies investigate the correlations between the arrival directions of UHECRs and the possible candidates for UHECR origins. In recent studies, a maximum-likelihood method is employed which assumes the population of UHECR origins and investigates the correlation between the observed UHECRs and the model CR flux patterns expected from the source model. In these studies, the maximum-likelihood method estimates the anisotropic fraction $f_{\rm ani}$ (a fraction of observed UHECR events due to the assumed sources) and the separation angular scale θ (the mean angular separation between UHECRs and their assumed origins). For example, Aab et al. (2018) assumed the nearby starburst galaxies (SBGs) to be the origin of UHECRs (SBG model) and applied a maximum-likelihood analysis to the observed UHECR events and CR flux patterns based on the SBG model (see Section 3.1 for detail). Aab et al. (2018) calculated the best-fit parameter to be $(f_{\rm ani}, \theta) = (9.7\%, 12.9\,{\rm deg})$ and suggested that the nearby SBGs contribute the UHECR anisotropies. These recent

studies suggest that the SBG model is one of the most interesting models with regard to UHECR origins.

However, in their study, the effect of the coherent deflections caused by the galactic magnetic field (GMF) is not taken into account (Rouillé d'Orfeuil et al. 2014). Figure 1.1 shows the prediction of the deflection angles of UHECRs that are caused by the GMF. UHECRs with rigidities of $R = 60$ EV are deflected more than 10 degrees at the most (larger than the best fit parameter $\theta = 12.9\,\mathrm{deg}$), where rigidity R is defined as $R = E/Ze$ with the particle energy E, atomic number Z, and the elementary charge e. The deflection is coherent to the structure of the galaxy and depends on the arrival direction of each UHECR. Previous studies do not consider the coherent deflection caused by the GMF and only treat it as Gaussian-like smearing (von Mises-Fisher function, see detail in Section 3.1) by the random magnetic field. Although we can assume an unknown intergalactic magnetic field (IGMF) to be smearing, we cannot approximate the effects of the coherent deflection caused by the GMF on the smearing.

In addition to the dependence on the arrival directions of UHECRs, the coherent deflection angle related to the GMF is inversely proportional to the rigidities of the UHECRs. Figure 1.2 shows the distributions of the simulated mock UHECRs through a GMF from the same source model with an energy spectrum taken into account. The left and right panels show the distribution of protons and irons, respectively. The distribution of UHECRs differs based on the dependence of their rigidities. Due to the dependence of the deflections caused by the GMF on the rigidity ($R = E/Ze$) of the particle, we need to take into account the continuous spectrum of rigidity and the mass composition of UHECRs. We call these effects that are caused by the GMF "the GMF bias".

In addition to the GMF bias, there is the problem of the limitation in the sky coverage on each experiment (Sommers 2001). Due to the difference in the structure of the GMF in the northern and southern hemispheres, the GMF bias has been said to exhibit a different feature in the north sky (TA experiment) and the south sky (Auger experiment). Although this difference affects the results of the previous analyses, it has not been considered in the previous studies.

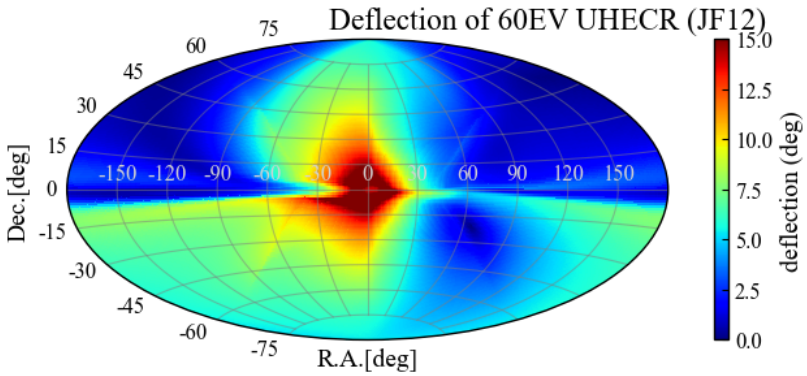

Figure 1.1: Coherent deflection of 60 EV UHECRs through the GMF (galactic coordinates, reproduced based on Figure 11 in Jansson & Farrar (2012a)). The color indicates the coherent deflection angles [deg].

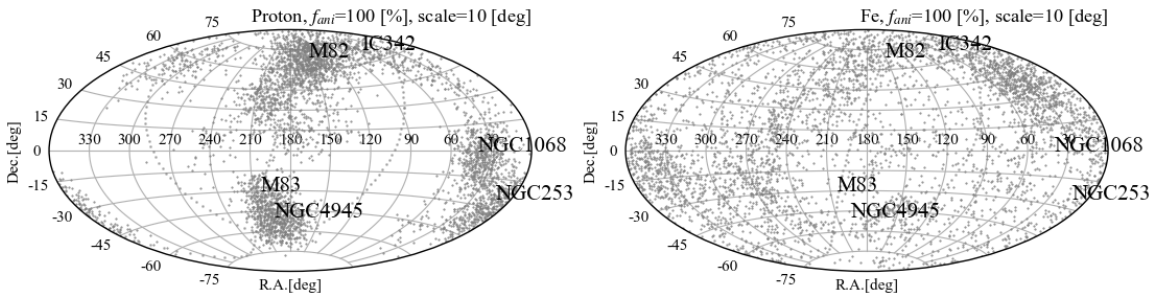

Figure 1.2: Comparison of deflections for UHECR distributions through the GMF (in equatorial coordinates). The gray dots illustrate the simulated distribution of the mock UHECR events through the GMF that are generated with the same source model and an energy spectrum. The left and right panels show the distribution of the mock UHECR events with the pure-proton assumption and the pure-iron assumption, respectively. The distributions of the UHECRs change with a dependence on their rigidities R.

In this study, I use a GMF model and investigate the GMF bias in the previous studies on UHECR anisotropies. To consider the GMF bias, I take the energy E and the mass A (charge Z) of each UHECR into account in the investigation. We also propose a new method for reducing the GMF bias and apply it to the observational UHECR datasets of the TA and Auger experiments. For the future plans of UHECR observatories, we test the new method and estimate the necessary mass resolutions and statistics.

The contents of this study are as follows: In Chapter 2, I introduce the theoretical and observational backgrounds of UHECRs and the current UHECR observations. In Chapter 3, I introduce the backgrounds of certain techniques: the maximum-likelihood method in the previous studies and GMF models. In Chapter 4, I estimate the GMF bias in the previous parameter estimation based on the calculation performed with mock UHECR events. In Chapter 5, I develop a new analysis method with the convolution of GMF bias and apply it to the actual observational dataset. In Chapter 6, I discuss the future plans for large UHECR observations and analyses. I summarize all topics in Chapter 7.

CHAPTER 2
INTRODUCTION TO UHECR STUDIES

In this chapter, I provide a theoretical and experimental introduction to UHECR studies and discuss the motivations and the role of this study.

2.1 Cosmic rays

Cosmic rays (CRs) are nuclei from the universe. They were discovered by Victor Hess in 1912 through an observation obtained using a balloon (historical review in Grupen (2013)). The overview of the CR energy spectrum is presented in Figure 2.1 (Swordy 2001). In a large energy scale, the spectrum scales a power-law E^{α}, where $\alpha \sim 2.5 - -3$. In particular, it is known that extremely high-energy CRs come to the earth whose energies are around or above the GZK limit (Greisen 1966; Zatsepin & Kuz'min 1966, see Section 2.2.1). In this study, I define UHECRs as CRs whose energies are above 10^{18} eV.

2.2 Ultra high energy cosmic rays

2.2.1 GZK limit

CRs interact with the cosmic microwave background (CMB). For example, a proton with energy 100 EeV experiences a photo-pion generation with a mean-free path of 100 Mpc.

$$p + \gamma \rightarrow \Delta^{+} \rightarrow p + \pi^{0},\ n + \pi^{+} \tag{2.1}$$

Due to the energy loss through the photo-pion generation, most UHECRs cannot propagate more than 30 – 100 Mpc (Figure 2.2). Due to this effect, it is suggested that the CRs whose energies are more than $\sim 10^{20}$ eV cannot be observed on the earth. This effect is called the GZK effect, and it is suggested that the limit of the

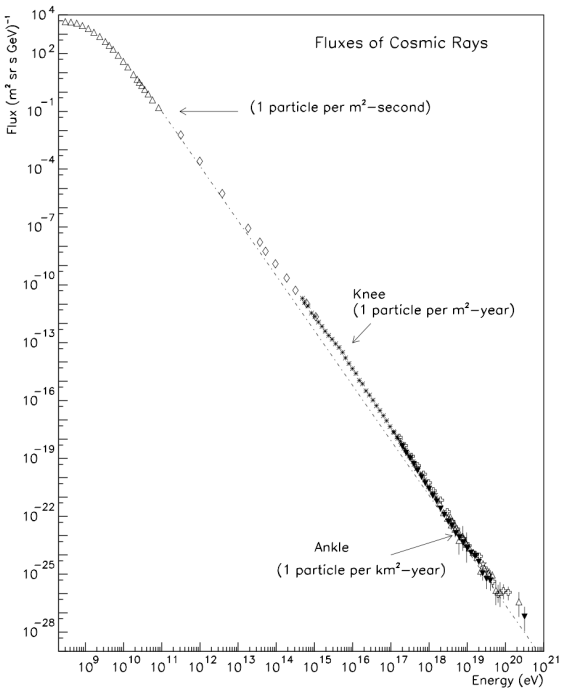

Figure 2.1: Energy spectrum of CRs (Swordy 2001). Different markers indicate different observations.

energy (the GZK limit) makes a steep cutoff of the CR energy spectrum around it (Greisen 1966; Zatsepin & Kuz'min 1966, GZK cutoff).

2.2.2 Discovery of super-GZK events

In 1991, the Fly's Eye air shower detector in Utah detected the highest energy CR ever observed whose energy is 3.2×10^{20}eV (Bird et al. 1995, Oh-My-God particle). The Akeno Giant Air Shower Array (AGASA) experiment (whose 111 surface detectors covered 100 km^2 of the town of Akeno in Yamanashi prefecture, Japan during 1991-2004) also reported extremely high-energy CRs that were above the GZK limit (Hayashida et al. 1994; Takeda et al. 1998). The AGASA experiment is the first experiment that collected UHECR events for statistical studies. These results motivated discussions regarding the exotic origin of UHECRs, such as the Lorenz invariance violation and so on (Tinyakov & Tkachev 2001). On the other hand, the High-Resolution Fly's Eye (HiRes) experiment conducted during the period of 1997-

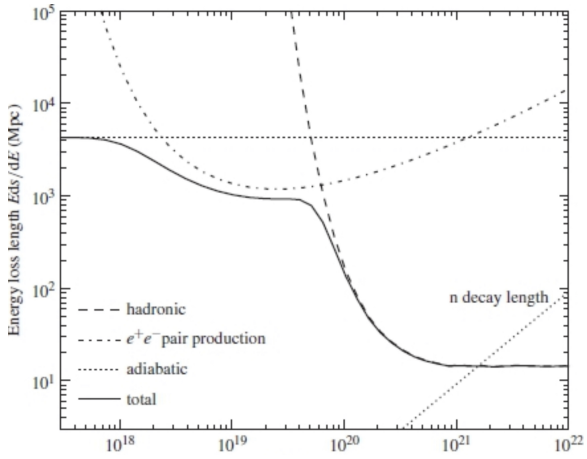

Figure 2.2: Energy loss length for protons in the CMB (Gaisser et al. 2016). The black solid line shows the total energy loss length.

2006 reported the GZK cutoff from fluorescence detectors (Abbasi et al. 2008). This inconsistency was one of the biggest problems in astroparticle physics in the 2010s and motivated researchers to start collecting hybrid UHECR observations using surface detectors (SDs) and fluorescence detectors (FDs) over a 1000 km^2 scale: Telescope Array (TA) and Auger experiments.

2.3 Origin of UHECRs

In this section, I introduce the possible candidates for UHECR origins.

To explain the existence of super-GZK events and the presence or absence of the GZK effect, we need to consider the following scenarios:

1. There are origins of UHECRs located $\sim$ Mpc from the earth. In this case, we can see a correlation between UHECRs and known active astronomical objects.

2. If there are no known origins for astronomical objects, there should be other sources, such as transient objects or exotic scenarios that disable the GZK process (exotic model, including the top-down scenario).

There are two categories for UHECR origins overall: bottom-up models and exotic models. In bottom-up models, we assume the known celestial objects that accelerate

particles to ultrahigh energies. In exotic models, we assume the top-down models that generate the ultrahigh-energy particles without acceleration or assume particle accelerations that involve exotic scenarios to avoid the GZK process.

2.3.1 Bottom-up models

In bottom-up models, we need to consider the accelerating mechanisms related to ultrahigh-energy and the escape of the particle from its origin.

Shock acceleration mechanism

As Figure 2.1 shows, the CR energy spectrum has the shape of a power-law function. To interpret the energy spectrum of CRs from observations, the bottom-up models need acceleration mechanisms that can explain the power-law feature. Fermi (1949) proposed a mechanism of the statistical acceleration process of particles that explains the power law of the CR energy spectrum (Fermi mechanism of 2nd order). For more efficient acceleration, particles likely accelerated through the astronomical shock (Fermi mechanism of 1st order). In this acceleration mechanism, a particle can gain a small amount of energy every time it is scattered across the front of an astronomical shock. If the particle is confined to the shock by a strong magnetic field, it can experience a significant amount of scattering and, eventually, becomes a high-energy particle. Here, I refer to a simple model of shock acceleration summarized by Grupen (2020). Assuming the initial energy of a particle E_0 and obtained energy through one cycle ϵE_0, the accelerated energy E_n after n-th scattering cycle is calculated as

$$E_n = E_0(1+\epsilon)^n. \tag{2.2}$$

The number of cycles required to accelerate to the energy of E is

$$n = \frac{\ln(E/E_0)}{\ln(1+\epsilon)}. \tag{2.3}$$

If one assumes the escape probability of a particle in one cycle to be P, the number of particles whose energies would be above E is derived as

$$N(>E) \propto \sum_{m=n}^{\infty}(1-P)^m = (1-P)^n/P. \tag{2.4}$$

With a substitution of n in Equation 2.3, an energy spectrum is obtained as

$$N(>E) \sim \frac{1}{P}(\frac{E}{E_0})^{-\gamma} \sim E^{-\gamma}, \tag{2.5}$$

where a spectrum index of γ is shown as

$$\gamma = -\frac{\ln(1/(1-P)}{\ln(1+\epsilon)}. \tag{2.6}$$

This model explains the power-law shape of the CR energy spectrum. Because astronomical shocks are ubiquitous in the universe, shock-like particle accelerations are expected and observed throughout the various scales of astronomical objects, such as solar flares, supernova remnants, and jets from active galactic nuclei (AGNs).

Hillas plot

To contain CRs during acceleration, the object that accelerates them needs to have a larger area than the Larmor radius of the CR in the magnetic field. The objects' size L, strength of magnetic field B, energy E, and particle charge Ze are constrained as follows (Hillas 1984; Letessier-Selvon & Stanev 2011):

$$\left(\frac{E}{\mathrm{EeV}}\right) < \beta Ze \left(\frac{B}{1\,\mu\mathrm{G}}\right)\left(\frac{L}{1\,\mathrm{kpc}}\right) \tag{2.7}$$

where $\beta = v/c$ is a shock velocity. This constraint is visualized in the Hillas plot (Figure 2.3). The objects that are on the upper-right side of the line in Figure 2.3 can be candidates of UHECRs. The Hillas plot suggests many populations of UHECR origin candidates on many size scales.

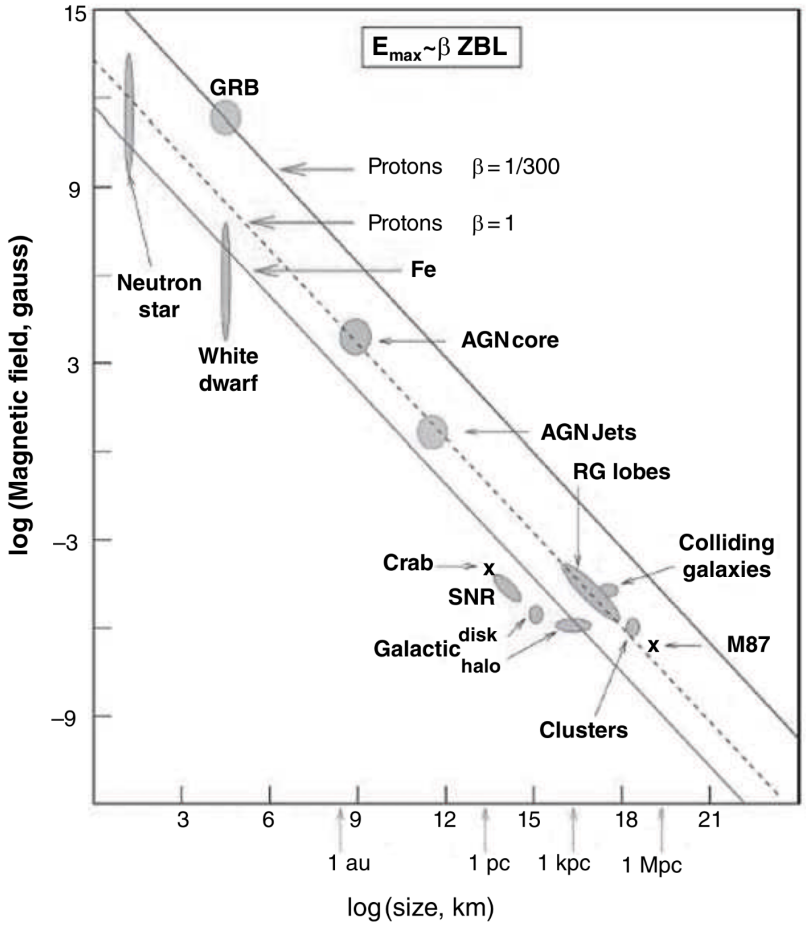

Figure 2.3: Hillas plot (Sokolsky & Thomson 2020, based on Hillas (1984)). The x-axis shows the typical size of the objects, and the y-axis shows the strength of their magnetic fields. The gray regions indicate the population of the candidates for UHECR origins. The gray regions on the upper-right side of the line can be candidates for UHECRs.

2.3.2 Steady objects

Here, I explain the possible candidates in bottom-up models. First, I introduce the steady objects that are suggested to constantly emit high-energy particles.

SBGs

SBGs are star-forming galaxies whose star formation rate (SFR) is extremely high. SBGs are usually defined as galaxies whose infrared luminosity is more than 10 times brighter than a normal galaxy (Batista et al. 2019). The frequent star-formation activities (ex. GRBs, supernovas, etc.) and nuclear outflow in SBGs are possible candidates for origins of UHECRs (Zhang et al. 2018; Zhang & Murase 2019). Recent UHECR observations report excesses of arrival directions around SBGs (ex. M82 and NGC4945), and they are said to be one of the most likely source candidates. As discussed later in this work, certain nearby SBGs within a few Mpc from the earth are suggested to be the origin of UHECR anisotropies (Table 2.1).

AGNs

An AGN is the central region of active galaxies that emit strong electromagnetic waves. AGNs are supposed to contain a massive accreting black hole. Radio galaxies, quasars, and Seyfert galaxies are types of AGNs. Further, jets and radio robes in AGNs are said to be the origin of UHECRs (Batista et al. 2019; Anchordoqui 2019). Although the bursts in them are transient, I introduce AGNs as steady objects due to their frequent activities. Blazars (which are supposed to be a type of quasar) on the arrival direction of neutrinos are known to generate γ-ray flares with the same timing of them. IceCube Collaboration et al. (2018) reported the coincidence of a γ-ray flaring blazars (which are supposed to be quasars) and the high-energy neutrino observed during the IceCube experiment. This implies that blazars accelerate hadrons and they could be possible candidates for UHECR acceleration.

Galaxy clusters

Galaxy clusters are defined as groups of galaxies that include more than ~ 100 galaxies on the Mpc scale. Even if their magnetic field is weak, a large-scale structure (on the Mpc scale) may enable the acceleration of CRs to UHECRs (Fang & Olinto 2016; Fang & Murase 2018). Some of the current reports suggest that the UHECR anisotropies follow the direction of galaxy clusters (Abbasi et al. 2021c). However, I also note that both the TA and Auger experiments do not report the significantly excessive number of UHECR events from the Virgo cluster, which is one of the closest galaxy clusters.

2.3.3 Transient objects

When we cannot explain the UHECRs origin by steady objects, we need to consider transient objects.

γ-ray bursts

γ-ray bursts (GRBs) are phenomena that emit high-energy γ-rays in short periods (from $\sim$ 10ms to $\sim$ 100 s). Based on the observations of afterglows in the X-ray range and optical/infrared follow-up, the origin of GRBs is known to be extragalactic objects (ex. Frail et al. (1999)). GRBs are classified into two categories: long-duration bursts and short-duration bursts (Grupen 2020). The long-duration bursts are believed to originate from supernova activities. One of the origins of short-duration bursts is thought to be magnetars, which are neutrons stars with extremely strong magnetic fields. Neutron stars are also possible candidates for UHECR origins, having another acceleration mechanism of shock acceleration. Recently, from a multi-messenger observation including gravitational waves (Abbott et al. 2017, GW170817), a neutron star merger is also suggested to be one of the origins of short-duration bursts.

Fast radio bursts

Fast radio bursts (FRBs) are known to produce radio emissions in short periods of time (millisecond scale). The first detection of an FRB was reported in 2007

(Lorimer et al. 2007). Although their source remains unknown, certain populations are suggested to have extragalactic origins (Cordes & Chatterjee 2019). Magnetars, which are neutron stars with extremely strong magnetic fields, are suggested to be the source of FRBs.

2.3.4 Exotic Models

I briefly summarize examples of exotic models (Stecker 2003).

"$X-$ particles": superheavy particles and topological defects

For famous examples of top-down models, there are scenarios of superheavy particles or topological defects (Berezinsky et al. 1998) that generate "X-particles" through annihilations, and the super-heavy dark matter (SHDM) scenario is one of them. Supanitsky & Medina-Tanco (2019) investigated a SHDM scenario with a mass of $10^{22.3}$ eV and suggest the main contribution to be from the Andromeda galaxy. The authors also suggested that the next-generation UHECRs, with a coverage of 10^6 km^2, would constrain the scenario.

Z-bursts

It is thought that the cosmic neutrino background (CNB) and high-energy neutrinos interact through the Z boson and generate hadrons by decaying into quarks. Although the Z-bursts scenario can explain the UHECR origins that are at a great distance over the GZK horizon (Fargion et al. 1999), it needs the assumption of extremely high-energy neutrinos. The direct detection of the CNB has not been achieved to date.

Violation of the Lorentz invariance (LI)

Assuming a violation of the Lorentz invariance (LI) at the ultrahigh-energy scale, we can explain the non-existence of the GZK cutoff (Coleman & Glashow 1999).

2.4 Current experiments

The direct observation of UHECRs is difficult due to their low flux density (1 event/100 yr $\cdot$ km^2). A UHECR is known to produce an air shower, which is a phenomenon in which the primary CR interacts with nuclei in the atmosphere and creates many secondary particles (extensive air shower, EAS). An extensive air shower extends to the $\sim$ 10 km scale, which enables the indirect observation of UHECRs. As the secondary particles in an extensive air shower spread on a 10 km scale, one can obtain an effective area for the observation of UHECRs using a particle detector array whose detectors are placed with a 1 km-scale dispersion. This array is called a surface detector (SD) array. The CRs in the atmosphere emit fluorescent lights due to the excitation of molecules (ex. N, O_2). An extensive air shower emits fluorescent lights along its trajectory, the intensity scales to the energy of the primary CR. One can observe the fluorescent light with an optical telescope and photosensors. We call this instrument a fluorescence detector (FD). A primary method used to observe UHECRs involves utilizing a hybrid of SDs and FDs in the same experiment. The TA experiment and the Pierre Auger Observatory (Auger experiment) currently lead the observations of UHECRs in the northern and southern hemispheres, respectively.

2.4.1 TA experiment

The TA experiment (Kawai et al. 2008; Sagawa 2020) was constructed in Utah, USA (39.3° N, 112.9° W) to observe the air showers induced by UHECRs. The experiment is composed of 507 SDs (Figure 2.5, Abu-Zayyad et al. (2012)) and three FD stations (Tokuno et al. 2012). The SDs used in the TA experiment are composed of plastic scintillators and placed in a 1.2 km-interval grid that covers 700 km^2 (Figure 2.4). Three FD stations are placed in a triangle at a distance of approximately 30 km (Figure 2.4). The observations of the TA experiment began on May 11, 2008.

For observing CRs with an energy threshold 10^{16} eV, the Telescope Array Low-energy Extension (TALE) experiment was started in 2013 (Ogio 2018). As an extension of the TA experiment, the construction and observation of the TA$\times$4 experiment is on-going (Abbasi et al. 2021a, Section 6).

Although SDs can produce observations regardless of weather and time of day, the resolutions of the energy and the mass of the primary particles are not high as those detected by FDs. Although the stereo observation of more than two FDs enables high-resolution energy and mass estimation, the duty cycle is $\sim 10\%$ of that of SDs, due to the limited observation time possible on clear nights without the moon. The raw data of an extensive air shower recorded by SDs is reconstructed with a comparison to Monte Carlo (MC) shower simulations.

Data analysis of the TA experiment

I briefly summarize the data analysis method of the SD/FDs of the TA experiment. The principle is the same for the Auger experiment. For the SDs, first, we determine the geometrical parameters of EAS (direction vector of the shower, time to reach the ground, the position vector of the core of the extensive air shower) by a geometrical fitting. Next, we derive the lateral distribution of particles and determine the number density at a distance of 800 m from the air shower core (S800). S800 is a parameter that is determined by the energy of a primary particle and the zenith angle of the air shower. We compare the S800 derived from the observation and that obtained by the MC calculation to determine the energy of the primary particle. CORSIKA (Heck et al. 1998), which is one of the most commonly used programs for MC shower simulations, is used for the air shower simulation of the TA experiment. In a hybrid observation using SDs and FDs in the TA experiment, it is known that the reconstructed energy of a UHECR with SDs is 27% higher than that observed using FDs (Abu-Zayyad et al. 2013). Due to the difference in the energy between SDs and FDs, the energies observed by SDs are rescaled to the FD energy scale by dividing them 1.27. The angular resolution of the arrival directions of UHECRs is $\sim$ 1-2°.

It is not possible to know the types of the nucleus of primary CRs directly from SD observations. The depth of the maximum development of EAS $X_{\rm max}$ observed by FDs is an important variable for estimating the mass A of a primary particle. An intensity of fluorescence light from an EAS scales the energy of the primary particle E. Because $X_{\rm max}$ scales to the log-scale of the energy per nucleon $\log(E/A)$, it is a

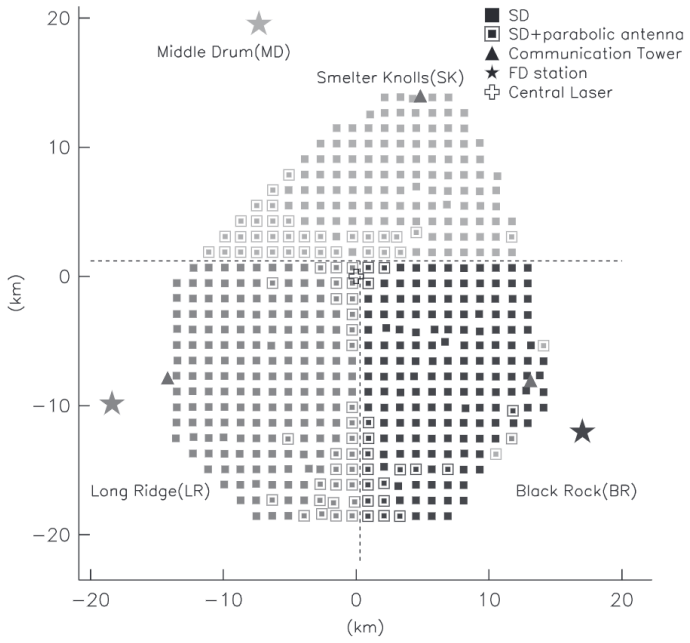

Figure 2.4: SD map of the TA experiment (Abu-Zayyad et al. 2012). The black and gray squares show the position of the SDs, and the stars indicate the FD stations (Middle Drum, Long Ridge, and Black Rock). The white cross represents the position of the central laser facility (CLF).

good indicator of mass composition estimation. We compare the $X_{\max}$ distribution obtained from the observation and MC calculation with an assumption of the mass A. This also depends on the hadron interaction model.

2.4.2 Auger experiment

The Pierre Auger Observatory (Aab et al. 2015a, Auger experiment) is located in Argentina (latitude 35.2° S, longitude 69.5° W). Similar to the TA experiment, the Auger experiment is also composed of SDs and FDs. The SDs used in the Auger experiment are water Cherenkov detectors (the right panel in Figure 2.7), which are different from those used in the TA experiment. The SDs used in the Auger experiment are also trying to estimate mass due to the high sensitivity of the water Cherenkov detectors to muons (Aab et al. 2017). In total, 1600 SDs are placed at 1.6 km intervals and cover 3000 km^2. The observations for the Auger experiment started

Figure 2.5: An SD for the TA experiment (photo by the author, July 2019).

Figure 2.6: (Left) the dome of the FD station used in the TA experiment at Black Rock (photo by the author, January 2020). (Right) the FDs inside the dome (photo by Takashi Sako, January 2018).

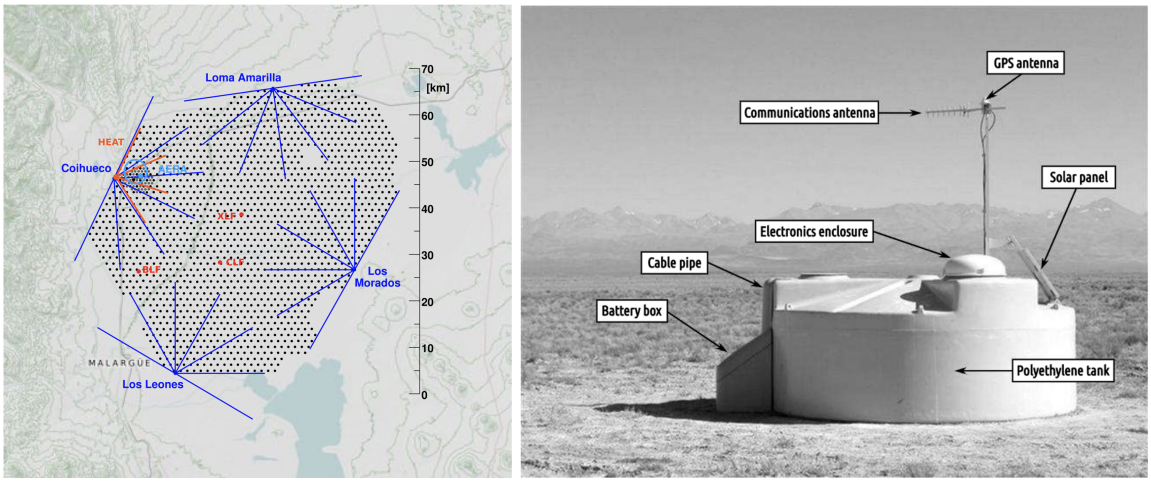

Figure 2.7: (Left) the layout for the Auger experiment (The Pierre Auger Collaboration et al. 2016). The black circles show the positions of the SDs, while the blue lines indicate the field of view (FoV) of the FDs. (Right) an SD station used in the Auger experiment (Figure 3. from Aab et al. (2015a)).

on January 1st 2004.

2.5 The current results of the UHECR observations

Now, I present the main results from the TA and Auger experiments. The most important results involve three topics: energy spectrum, mass composition, and anisotropies.

2.5.1 Energy spectrum

The TA and Auger experiments measured the energy spectrum of UHECRs (Abu-Zayyad et al. 2012; Aab et al. 2015a; Ivanov 2017). I have shown the combined energy spectrum of UHECRs observed through the TA and Auger experiments (Sokolsky & Thomson 2020; Ivanov 2019, Figure 2.8). Based on a comparison of the TA and Auger datasets in the same declination band, it can be seen that the estimated energies of UHECR show systematic differences of 10%. In Figure 2.8, the spectra of TA and Auger datasets are combined by scaling the energies by 10%. The spectrum shows the specific features called the "knee," "second knee," and "ankle." We can see the

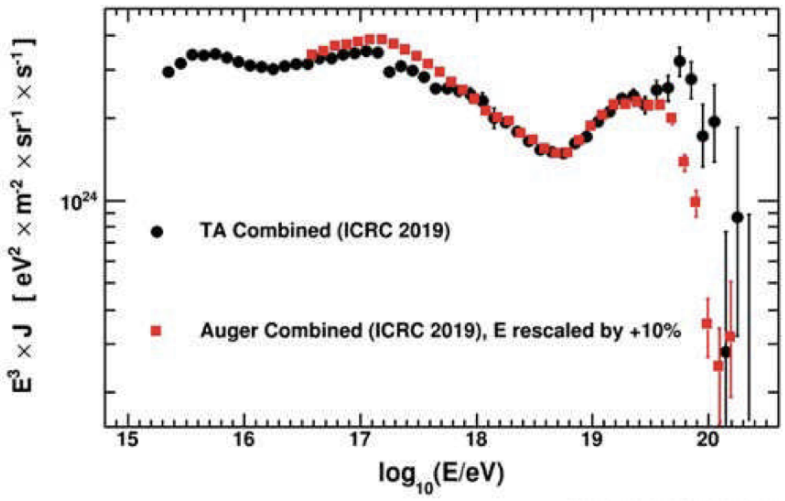

Figure 2.8: Combined energy spectrum for the TA and Auger experiments (Sokolsky & Thomson 2020). The black circles show the combined spectrum with the TA and TALE experiments (Ivanov 2019). The red squares indicate the spectrum of the Auger experiment. The energies measured by the Auger experiment are rescaled by +10%.

cutoff of the spectrum above $10^{19.81}$ eV (Tsunesada et al. 2017, broken-power law), which is consistent with the GZK prediction. However, note that the cutoff of the energy spectrum does not directly prove the GZK prediction (Ogio et al. 2019). It is not clear whether the cutoff of the spectrum is produced by the GZK effect or the limit of the acceleration mechanism.

Due to the consistency with the GZK prediction, bottom-up models have become more possible explanations for the UHECR origins. To search for the UHECR source in the bottom-up models, an investigation of the mass composition and anisotropies of UHECRs would take an important role.

2.5.2 Mass composition

The TA and Auger experiments estimated the mass of UHECRs through the measurement of the mean maximum development of an EAS $\langle X_{\rm max} \rangle$ using FDs. The energy dependence of $\langle X_{\rm max} \rangle$ is shown in Figure 2.9. The result of the TA experiment suggests that the average mass number of UHECRs is around the mass of helium (Abbasi

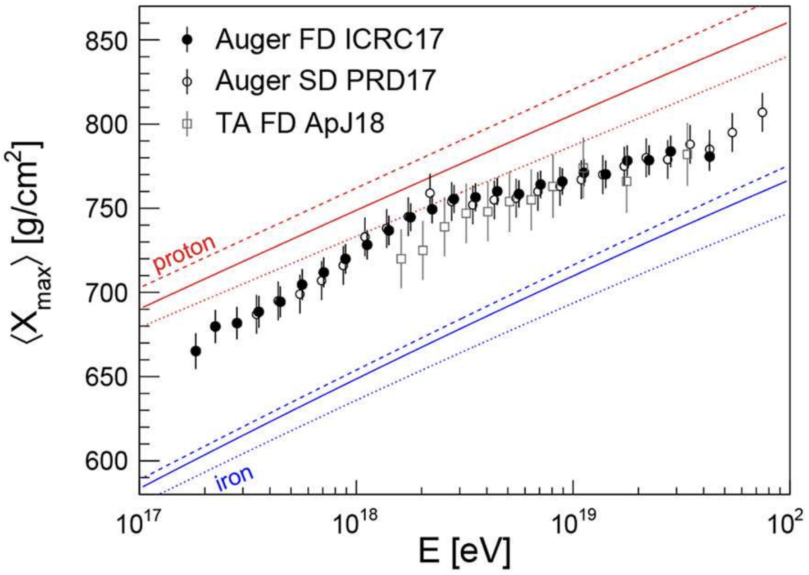

Figure 2.9: $\langle X_{\max} \rangle$ plot reported by the TA and Auger experiments (Batista et al. 2019). The black and white circles indicate the result obtained using the Auger FDs (Bellido & Pierre Auger Collaboration 2017) and Auger SDs (Aab et al. 2017), respectively. The white squares represent the results obtained using the TA FDs (Abbasi et al. 2018).

et al. 2018, Figure 2.9). The Auger experiment suggests that the mass composition of UHECRs becomes heavier with an increase in energy (Batista et al. 2019; Heinze & Fedynitch 2019, Figure 2.10). On the other hand, it is reported that the results of the mass measurements in the TA and Auger experiments are consistent with regard to their uncertainty (Abbasi et al. 2019).

2.5.3 UHECR anisotropy

Due to the larger statistics of observed UHECRs with current experiments, it is available to see the local excess of arrival directions of UHECRs and their distributions (UHECR anisotropy). In this section, I introduce examples of the UHECR anisotropies reported by the TA and Auger experiments.

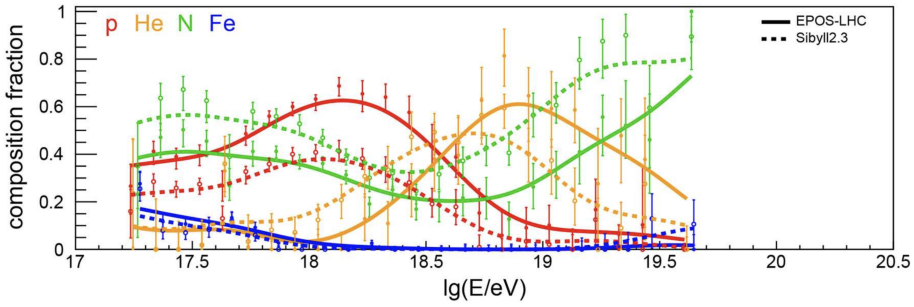

Figure 2.10: The mass fraction with the fitting of the observed $\langle X_{\rm max} \rangle$ in the Auger experiment (Batista et al. 2019).

TA 5yr dataset and TA hotspot

In the study conducted by Abbasi et al. (2014), the TA collaboration analyzed the data recorded from May 11, 2008 to May 4, 2013 (TA 5yr dataset). The TA 5yr dataset contains 72 UHECR events whose energy was above 57 EeV (panel (a) in Figure 2.11). Out of the 72 UHECRs in the TA 5yr dataset, $\sim$ 20 events were found to come from the same region within 20° radius (panel (b) in Figure 2.11). To evaluate the number excess of UHECRs, Abbasi et al. (2014) calculated the Li-Ma significance, which indicates the significance of number excess with contrast to the isotropic distribution. Abbasi et al. (2014) generated 10^5 MC events with an assumption of the isotropic distribution of UHECRs (panel (c) in Figure 2.11) for the background. The Li-Ma significance is given as

$$S_{\rm LM} = \sqrt{2}\left[N_{\rm on}\ln\left(\frac{(1+\eta)N_{\rm on}}{\eta(N_{\rm on}+N_{\rm off})}\right) + N_{\rm off}\ln\left(\frac{(1+\eta)N_{\rm off}}{N_{\rm on}+N_{\rm off}}\right)\right]^{1/2}, \tag{2.8}$$

where $N_{\rm on}$ ($N_{\rm off}$) is a number of observational (isotropic MC) events in the search radius. The normalization factor η is defined as the quotient obtained when the total number of observational events (72 events) is divided by that of isotropic MC events (10^5 events).

The distribution of the arrival directions of the TA 5yr data and the Li-Ma significance map showing a deviation from isotropy with a search radius of 20° are shown in Figure 2.11. The significance map shows the specific region whose significance

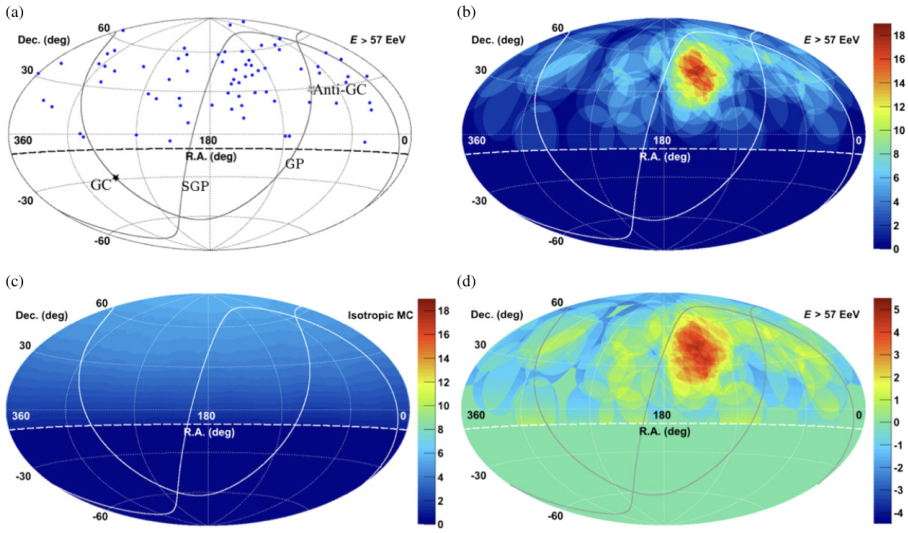

Figure 2.11: Maps of the TA 5yr dataset in equatorial coordinates. The top-left panel (a) shows the distribution of the events whose energies are above 57 EeV. The top-right panel (b) shows the number of events within a radius of 20°. The bottom-left panel (c) is the same as (b), but for isotropic MC events (10^5 events in total). The bottom-right panel (b) is the Li-Ma significance map of the dataset. The red region in panel (d) indicates the TA hotspot.

exceeds 5 σ. This region is called the "hotspot" (Abbasi et al. 2014, Figure 2.11). TA hotspot is centered at R.A.=146.7°,decl.=43.2°. This excess is also confirmed in the TA 11yr dataset generated from May 2008 to May 2019 (Kawata et al. 2019).

From the same calculation of the Li-Ma significance with a lower energy threshold, the TA collaboration also reports another excess of UHECRs (Abbasi et al. 2021c).

Auger warm spot and all-sky anisotropies

In addition to the TA hotspot, the Auger experiment reports an excess of UHECR events around Centaurus A and NGC4945 in the southern hemisphere called the "warm spot" (Abreu et al. 2012; Aab et al. 2015b, Figure 2.12).

Figure 2.13 shows the all-sky distribution of the arrival directions of the UHECRs observed in the TA and Auger experiments (di Matteo et al. 2020). These anisotropies are important because they are considered to be correlated with the distribution of

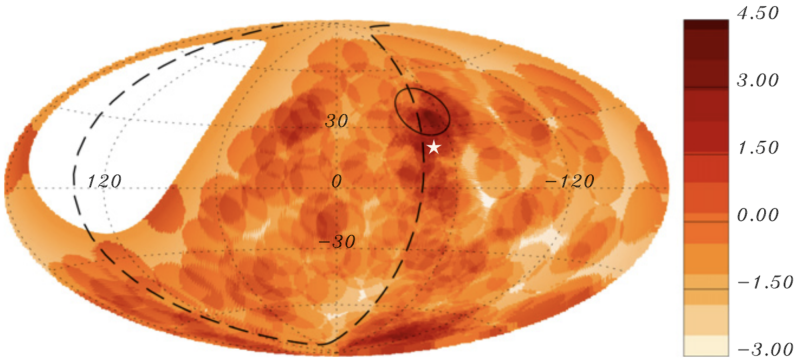

Figure 2.12: Li-Ma significance of the Auger 2015 dataset with a threshold energy of 54 EeV (Aab et al. 2015b, in galactic coordinates). The position of the "warm spot" is indicated by a black circle. The white star indicates the position of Centaurus A. The black dashed line shows the super-galactic plane (SGP).

the origin of UHECRs.

2.6 Previous studies on UHECR source association

2.6.1 Brief summary of UHECR source associations from the 2000s to the early 2010s

Considering the GZK limit, it is reasonable to think the UHECR anisotropies correlate with a distribution of nearby-extragalactic steady sources. There are many studies that investigated the correlations between UHECR anisotropy and the possible candidates for UHECR origins. Abreu et al. (2007) investigated the correlation between the distribution of AGNs and the 3.7-yr dataset of the UHECRs observed in the Auger experiment (whose energies were more than 60 EeV) and suggested a strong correlation between AGNs and UHECRs (Figure 2.14). However, this correlation has gotten weaker with the evolution of the number of UHECR events, and the current reports of the experiments do not support the association of UHECRs with AGNs (Abreu et al. 2010). Abreu et al. (2007) also suggested a correlation between UHECRs and the super-galactic plane (SGP). Abreu et al. (2010) conducted a maximum-likelihood method for nearby AGNs and galaxies, which is also used in

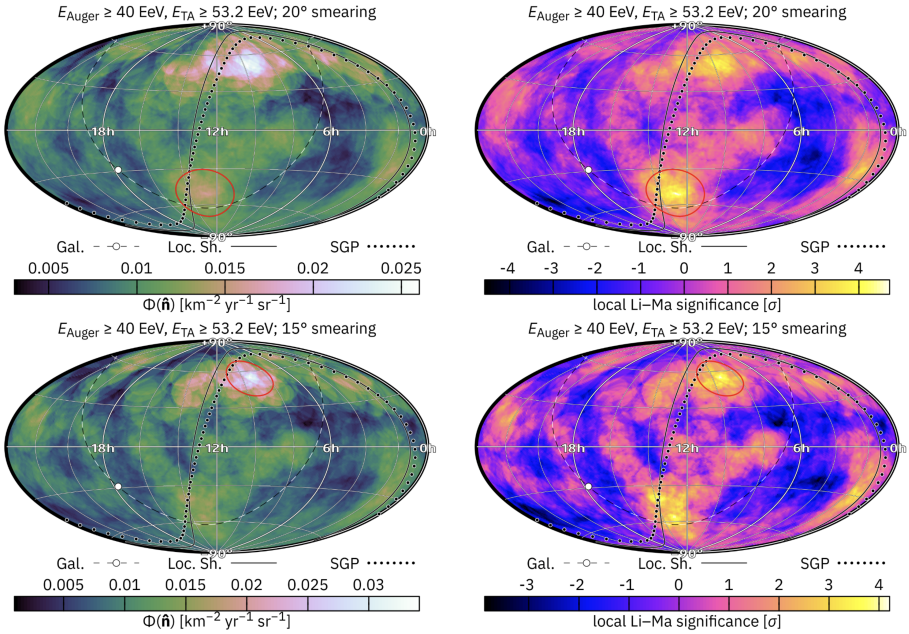

Figure 2.13: All-sky maps of UHECR anisotropy from the TA and Auger experiments in equatorial coordinates (di Matteo et al. 2020). The left panels show the CR flux map with a smearing of a 20° radius (top) and a 15° radius (bottom). The right panels are the same maps as the left but for the Li-Ma significance. The red circles indicate the regions whose excess is the most significant.

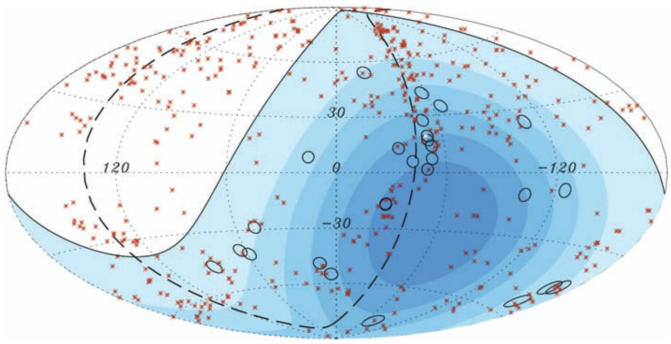

Figure 2.14: Distribution of 3.7-yr dataset of the UHECRs in the Auger experiment and the AGNs in the galactic coordinates (Abreu et al. 2007). The 27 arrival directions of the UHECRs are shown by the black circles. The red asterisks show the position of the AGNs within a distance of 75 Mpc from the earth. The blue contour indicates the same exposure that depends on the declination. The SGP is shown as a black dashed line.

recent studies (Aab et al. 2018; Abbasi et al. 2018, see in Section 3.1 for detail).

Fang et al. (2014) investigated the correlation between UHECRs in the TA 5yr dataset and the neutrino events from IceCube and suggested that a single star-forming galaxy could be the common origin of the UHECRs and neutrinos.

Through Bayesian estimation, He et al. (2016), with a single-source assumption, suggest that the highest contribution to the TA hotspot comes from M82.

2.6.2 Previous parameter estimations: the SBG and isotropic models

Starting from the late 2010s, the SBG models were believed to offer a possible explanation for the origin of UHECRs. Aab et al. (2018) calculated the model CR flux patterns of nearby SBGs/AGNs based on their distribution and contributions (Table 2.1). The model CR flux pattern indicates the probability of UHECR arrival directions expected from the assumed source model. The CR flux pattern is calculated as a convolution of the contributions from the assumed sources and isotropic component (Abreu et al. 2010; Aab et al. 2018, See also Section 3.1). The fraction of the source contribution, anisotropic fraction, is designated with a parameter $f_{\rm ani}$. To determine the effect of magnetic fields (including both the GMF and IGMF), the authors in

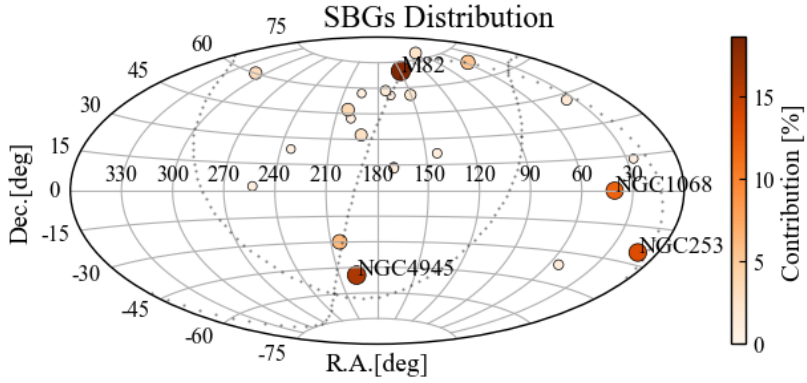

Figure 2.15: Distribution and contribution of SBGs in Table 2.1 from Aab et al. (2018) (equatorial coordinates). Circles are plotted at the positions of SBGs. The colors and sizes of markers show their relative contribution to the flux patterns.

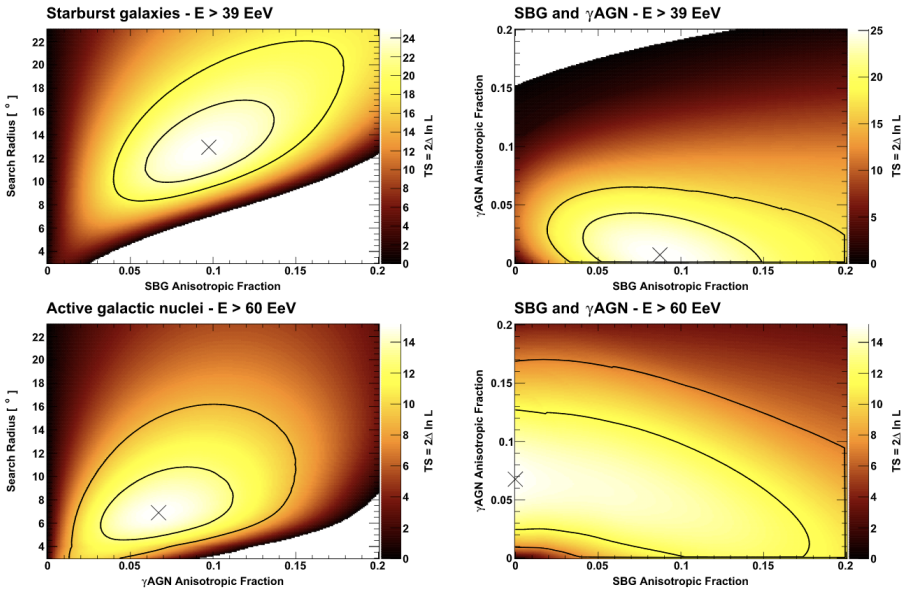

Figure 2.16: Likelihood distribution in Aab et al. (2018). The left panels show the TS distributions of the SBG model (top) and the AGN model (bottom). The right panels show the TS distributions of the combined models of SBGs and AGNs with $E > 39$ EeV and $E > 60$ EeV, respectively. The black cross indicates the best-fit parameter $(f_{\rm ani}, \theta)$ (see Section 3.1). The black lines show significance levels of 1 and 2 σ.

Aab et al. (2018) assumed the isotropic scattering of CRs given by the von Mises-Fisher (VMF) function (Fisher 1953). The von Mises-Fisher function represents the Gaussian distribution on the sphere (see also Section 3.1). The range of the isotropic scattering is determined by the separation angular scale θ, which indicates the mean angular separation between UHECRs and their assumed origins (See also section 3.1).

For nearby SBGs, they selected 23 SBGs based on the γ-ray selected $Fermi$-LAT data (Ackermann et al. 2012; Tang et al. 2014; Peng et al. 2016; Hayashida et al. 2013, Table 2.1 and Figure 2.15). As a condition for selection, Aab et al. (2018) imposed that the flux is more than 0.3 Jy and the distance from the earth is less than 250 Mpc. The contribution of each SBG was normalized by radio flux at 1.4 GHz. For nearby AGNs, they selected γ-ray AGNs (γ AGNs) from the 2FHL catalog also detected by $Fermi$-LAT (Ackermann et al. 2016). The contribution of each AGN was normalized by an integral flux between 50 GeV to 2 TeV.

Using the maximum-likelihood method (see Section 3.1 for detail), Aab et al. (2018) estimated the anisotropic fraction $f_{\rm ani}$ and the separation angular scale θ. Figure 2.16 shows the TS distribution calculated from the source model of SBGs/AGNs. As the top-left panel shows, the estimated anisotropic fraction $f_{\rm ani}$ was highest with the assumption of the SBG source. The best-fit parameters that explain the observed UHECR distribution by SBGs were estimated to be $(f_{\rm ani}, \theta) = (9.7\%, 12.9\,{\rm deg})$, and the nearby SBGs were suggested to be the most likely candidates for the origin of UHECRs (the SBG model).

To verify the result obtained by Aab et al. (2018), Abbasi et al. (2018) attempted the same analysis with the UHECRs observed by the TA experiment using the best-fit SBG model. In their analysis, 284 UHECR events were used whose energies were more than 43 EeV and which occurred between 2008 May to 2017 May (TA 9yr dataset). Abbasi et al. (2018) calculate the test statistics (TS) in case of the best-fit parameter $(f_{\rm ani}, \theta) = (9.7\%, 12.9\,{\rm deg})$ to study the significance of the SBG model in contrast with the isotropic distributions (the isotropic model). The TS was calculated to be -1.0. Figure 2.17 shows the TS distributions of the MC datasets with isotropic distribution and the SBG model. The derived TS deviate from the isotropic model by 1.1σ and the SBG model by 1.4σ. The results obtained by Abbasi et al. (2018) do

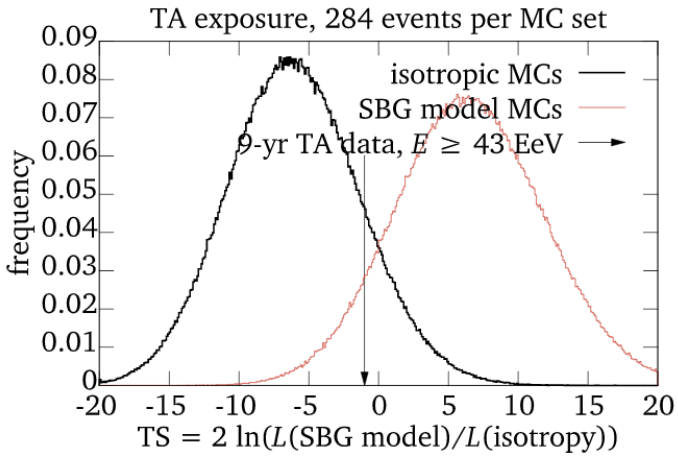

Figure 2.17: TS distribution of the TA 9yr dataset (Abbasi et al. 2018). The black line and the red line show the TS distribution of the mock UHECR datasets generated assuming the isotropic model and the SBG model, respectively. The black arrow indicates the TS calculated from the TA 9yr dataset. The TS are calculated in case of the Auger best-fit parameter $(f_{\rm ani}, \theta) = (9.7\%,\ 12.9\,{\rm deg})$.

not contradict those of Aab et al. (2018), but the number of events is not enough to conclude which model is correct.

Table 2.1: List of SBGs in Aab et al. (2018)

ID[a]	l [°] [b]	b [°] [c]	D [Mpc] [d]	f [%] [e]
NGC 253	97.4	-88	2.7	13.6
M82	141.4	40.6	3.6	18.6
NGC 4945	305.3	13.3	4	16
M83	314.6	32	4	6.3
IC 342	138.2	10.6	4	5.5
NGC 6946	95.7	11.7	5.9	3.4
NGC 2903	208.7	44.5	6.6	1.1
NGC 5055	106	74.3	7.8	0.9
NGC 3628	240.9	64.8	8.1	1.3
NGC 3627	242	64.4	8.1	1.1
NGC 4631	142.8	84.2	8.7	2.9
M51	104.9	68.6	10.3	3.6
NGC 891	140.4	-17.4	11	1.7
NGC 3556	148.3	56.3	11.4	0.7
NGC 660	141.6	-47.4	15	0.9
NGC 2146	135.7	24.9	16.3	2.6
NGC 3079	157.8	48.4	17.4	2.1
NGC 1068	172.1	-51.9	17.9	12.1
NGC 1365	238	-54.6	22.3	1.3
Arp 299	141.9	55.4	46	1.6
Arp 220	36.6	53	80	0.8
NGC 6240	20.7	27.3	105	1
Mkn 231	121.6	60.2	183	0.8

[a] Name of each SBG.

[b, c] Direction of each SBG in galactic coordinates.

[d] Distance from the earth.

[e] Relative flux contributions normalized by a radio flux at 1.4 GHz.

2.6.3 Recent studies convoluting the SBG model and the GMF models

The UHECR anisotropy is closely related to the mass composition, the source distribution, and the magnetic field. In this section, I explain recent various studies which incorporate the mass composition model, SBG model, and the galaxy magnetic field model.

First, there are studies that tried to reproduce the arrival direction distribution of UHECR with the assumption of a source model, a magnetic field model, and a mass composition (forward-tracking). For example, Attallah & Bouchachi (2018) assumed the SBG model and pure-proton/mixed-mass composition and simulated the CR trajectory through the GMF and IGMF to reproduce the observed UHECR anisotropies. Although the method of forward-tracking is a reasonable idea, there is a problem that the calculation cost is high due to the small number of particles that can reach the earth from the source.

Another idea is constraining the GMF/IGMF from the observed UHECR anisotropy, assuming the source model and the mass composition is correct (Soriano et al. 2019; van Vliet et al. 2021). van Vliet et al. (2021) attempts to limit the IGMF from the UHECR anisotropy observed through the Auger experiment, assuming a source model.

There is another idea that motivates to estimate the mass composition of UHECRs with assumptions of the source model and the magnetic field model (Anjos et al. 2018; Kuznetsov & Tinyakov 2021).

In any idea, we need to assume more than two out of three models are correct: the mass composition, the source model, and the magnetic field. In this study, I assume all the three models and clarify the bias in the commonly used maximum-likelihood method (see Section 3.1 for detail).

2.6.4 Goal of this study: evaluation and reduction of the GMF bias in the SBG model

As Aab et al. (2018) and Abbasi et al. (2018) show, SBGs are currently one of the most interesting candidates for the origin of UHECRs. However, these studies treat

the deflections caused by magnetic fields as Gaussian-like smearing angles, which is different from the actual scenario (see Section 3.1). Although the SBGs are suggested to explain the observed UHECR anisotropy, the required contribution is only 10%. In this case, the origin of the remaining 90% isotropic contribution would be a problem. Before discussing the origin of the isotropic fraction, however, we need to rule out the possibility that the anisotropic fraction is underestimated by the ignorance of the GMF effect in the previous analysis. It is clear that the regular component of the GMF has a structure (see Figure 1.1), and we cannot approximate the coherent deflection of UHECRs by GMF (Jansson & Farrar 2012a,b) using a Gaussian-like von Mises-Fisher (VMF) function. This omission of the coherent deflection caused by the GMF has led to a bias in the previous analyses (GMF bias). In this study, I use a commonly-used GMF model (Jansson & Farrar 2012a,b, JF12 model) and investigate the GMF bias in the previous studies. To investigate the GMF bias, I consider an energy E and mass A (charge Z) of each CR. I also propose a new analysis method to reduce GMF bias and apply it to the observational datasets obtained from the TA and Auger experiments.

CHAPTER 3
THEORETICAL AND TECHNICAL BACKGROUNDS

In this chapter, I summarize the important tools used in this study: maximum-likelihood analysis (Section 3.1) and flux mapping (Section 3.4).

By comparing the UHECR dataset and flux pattern of source models, a maximum-likelihood analysis derives the best-fit parameters for the source model. I follow the maximum-likelihood analysis performed by Aab et al. (2018) and Abbasi et al. (2018) and clarify the GMF bias in the previous analyses. I first calculated trajectories of the UHECRs in the GMF (CR trajectories) and then converted the arrival directions of the UHECRs observed on the earth to those of the UHECRs observed outside the galaxy (the galaxy sphere, which is defined as 20 kpc from the galactic center). Based on the CR trajectories, I calculate the flux patterns through the GMF (flux mapping). I use CRPropa3 for the calculation of the CR trajectories.

In this chapter, I also introduce the software (Section 3.3) and a GMF model (Section 3.2) employed in this study.

3.1 Maximum-likelihood analysis and model CR flux pattern without coherent deflection by the GMF

To search the major source population of UHECRs, previous studies (Aab et al. 2018; Abbasi et al. 2018) used a maximum-likelihood analysis. The maximum-likelihood analysis estimates two parameters:

1. Anisotropic fraction $f_{\rm ani}$: the fraction of all UHECR events due to their sources
2. Separation angular scale θ: the angular separation between an event and its source

The anisotropic fraction also indicates the fraction of UHECR that can be explained by the assumed source. The separation angular scale reflects the effects of random or turbulent magnetic fields inside and outside the galaxy.

3.1.1 Model CR flux pattern from SBGs

Assuming the parameter set $(f_{\rm ani}, \theta)$, I determine the CR flux pattern using the SBG model. Aab et al. (2018) and Abbasi et al. (2018) adopted the CR flux pattern from SBGs $F_{\rm org}(\mathbf{n}, \theta)$ as the sum of the von Mises-Fisher function (the Gaussian distribution on the sphere) of each source:

$$F_{\rm org}(\mathbf{n}, \theta) = \frac{\sum_i f_i \exp(\mathbf{n}_i \cdot \mathbf{n}/\theta^2)}{\int_{4\pi} \sum_i f_i \exp(\mathbf{n}_i \cdot \mathbf{n}/\theta^2) d\Omega} \tag{3.1}$$

Where, i indicates each SBG, and $\mathbf{n_i}$ and f_i show its direction and relative flux (contribution from each source), respectively. Note that if we assume θ_i as an angle defined by $\mathbf{n_i}$ and $\mathbf{n}$, $\exp(\mathbf{n}_i \cdot \mathbf{n}/\theta^2)$ scales a Gaussian function $\sim \exp(-\frac{1}{2}(\frac{\theta_i}{\theta})^2)$ with small angle θ_i.

The authors referred to Table 2.1 in Aab et al. (2018) for the values of f_i and $\mathbf{n}_i$. The relative flux of SBGs f_i are determined by their continuum radio flux (Aab et al. 2018; Ackermann et al. 2012). An example of the original CR flux pattern $F_{\rm org}(\mathbf{n}, \theta = 13\,{\rm deg})$ is shown in Figure 3.1.

The normalized model CR flux pattern $F_{\rm norm}$ can be written as the convolution of a model CR flux pattern due to sources $F_{\rm org}$ and isotropic flux pattern $F_{\rm iso}$:

$$F_{\rm norm}(\mathbf{n}, f_{\rm ani}, \theta) = f_{\rm ani} F^{'}_{\rm org}(\mathbf{n}, \theta) + (1 - f_{\rm ani}) F_{\rm iso} \tag{3.2}$$

$$F^{'}_{\rm org}(\mathbf{n}, \theta) = \frac{F_{\rm org}(\mathbf{n}, \theta)}{\int_{4\pi} F_{\rm org} d\Omega} \text{ and } F_{\rm iso} = 1/4\pi. \tag{3.3}$$

3.1.2 Maximum-likelihood analysis

In this study, I tested two hypotheses between the SBG model and the isotropic model.

The test statistics TS between the SBG model and the isotropic model are defined as log-likelihood ratio:

$$TS = 2\ln(L(F_{\rm norm})/L(F_{\rm iso})), \tag{3.4}$$

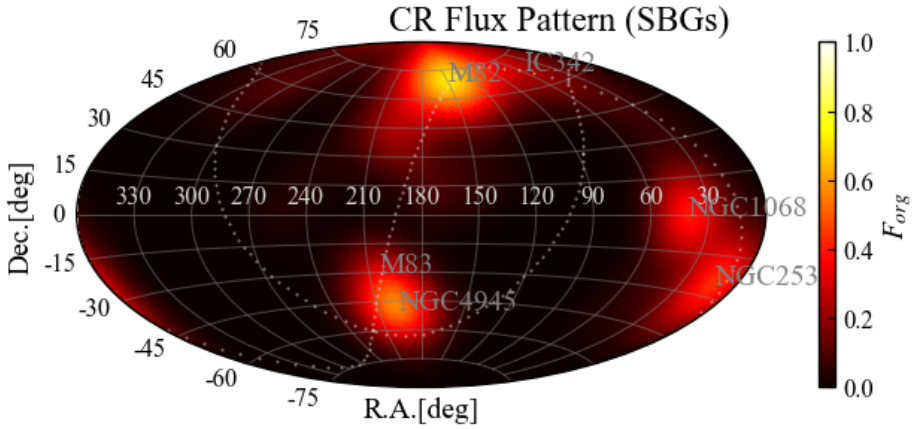

Figure 3.1: The CR flux pattern expected form the SBG model at the surface of the galaxy with $\theta = 13^\circ$ (in equatorial coordinates). The white dotted lines represent the galactic plane (GP) and the super-galactic plane (SGP). The top six contributing SBGs are mentioned in the figure.

where $L(F)$ indicates a likelihood

$$L(F) = \prod_{\mathrm{CR}} \frac{F(\mathbf{n}_{\mathrm{CR}})\omega(\mathbf{n}_{\mathrm{CR}})}{\int_{4\pi} F(\mathbf{n})\omega(\mathbf{n})d\Omega}. \tag{3.5}$$

In Equation 3.4, TS indicates the likelihood of the SBG model in contrast with the isotropic model. Here, F, $\omega(\mathbf{n}_{\mathrm{CR}})$, and $\mathbf{n}_{\mathrm{CR}}$ are the normalized model CR flux pattern, the exposure of each experiment, and the observed arrival directions of the UHECRs, respectively. In this case, the TS shows the significance of the SBG model for the null hypothesis (isotropic model). Note that the exposure of each experiment $\omega(\mathbf{n}_{\mathrm{CR}})$ varies with the latitude of the experimental site δ (Sommers 2001):

$$\omega(\delta) \propto \cos(a_0)\cos(\delta)\sin(\alpha_{\mathrm{m}}) + \alpha_{\mathrm{m}}\sin(a_0)\sin(\delta) \tag{3.6}$$

$$\alpha_{\mathrm{m}} = \begin{cases} 0\ (\xi > 1) \\ \pi\ (\xi < -1) \\ \cos^{-1}(\xi)\ (-1 < \xi < 1) \end{cases} \tag{3.7}$$

$$\xi = \frac{\cos(\theta_{\mathrm{m}}) - \sin(a_0)\sin(\delta)}{\cos(a_0)\cos(\delta)}, \tag{3.8}$$

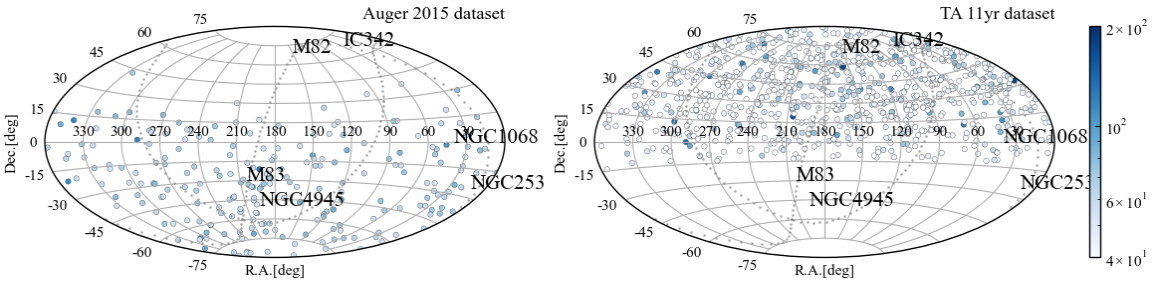

Figure 3.2: Distributions of the Auger 2015 (left panel) and the TA-11yr (right panel) datasets. The circles show the arrival direction of the observed UHECRs, and their colors indicate their energy [EeV].

where $\theta_{\rm m}$ is the maximum zenith angle and a_0 is the latitude of a detector, respectively.

By scanning the parameters $(f_{\rm ani}, \theta)$, the best-fit parameters that maximize the TS in Equation 3.4 are determined.

3.1.3 Reproduction of the estimated parameters using the Auger 2015 dataset

Table 3.1: Summary of the Auger 2015 and TA-11yr datasets

Dataset	Duration	Number of events	Threshold energy [EeV]
Auger 2015	2004 January 1– 2014 March 31	225	52.0
TA-11yr	2008 May 4 – 2019 May	279	43.0

In this section, I apply the analysis to the Auger 2015 dataset (Aab et al. 2015b). The Auger 2015 dataset is the latest public UHECR dataset of the Auger experiment. I also introduce the TA-11yr dataset in this section, which is referred to in later chapters. The TA-11yr dataset is the latest internal dataset of the TA experiment and is well-calibrated. I have summarized the duration of the observation, the number of events, and the threshold energy of each observational dataset in Table 3.1, and the UHECR distributions of both datasets are illustrated in Figure 3.2.

To test the analysis method, I conducted the maximum-likelihood analysis, in the same manner as Aab et al. (2018) for the Auger 2015 dataset (Figure 3.3). I calculated the TS with 225 UHECR events whose energies were above 52.0 EeV, and the best-fit

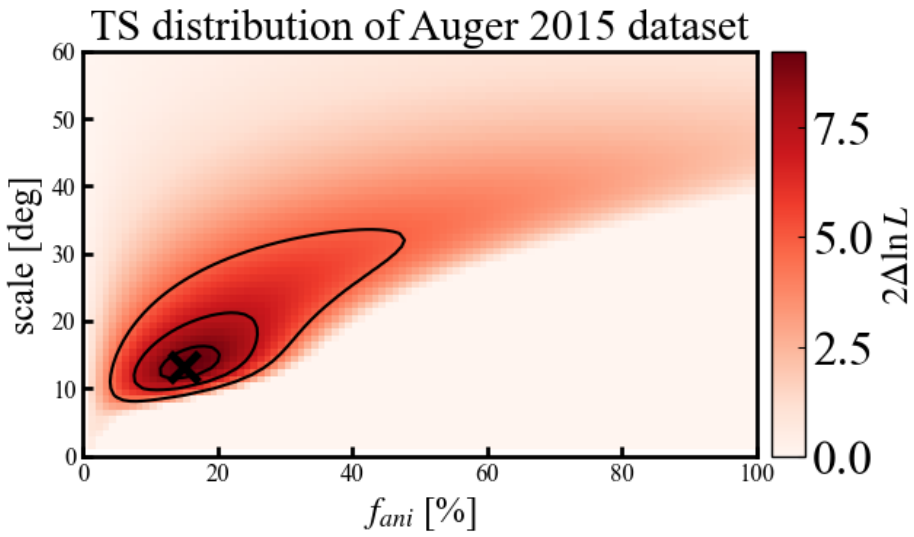

Figure 3.3: TS distribution for the Auger 2015 dataset reproduced by the author. The black cross shows the best-fit parameters of $(f_{\rm ani}, \theta) = (15\%, 13\,{\rm deg})$. The black contours indicate confidence levels of 1-3σ.

parameter for the Auger 2015 dataset was found to be $(f_{\rm ani}, \theta) = (15\%, 13\,{\rm deg})$, which is consistent with that of Aab et al. (2018) in the 2σ contour (shown in the top-left panel of Figure 2.16).

3.2 GMF models

In this section, I introduce the GMF model referred to in this paper. Although many models are suggested in literatures, the variation between the different GMF models is still large (Durrer & Neronov 2013). In this study, I use the GMF model developed in (Jansson & Farrar 2012a,b, JF12 model). The GMF is made up of a regular component and a random component (Farrar 2014). The regular component is said to be approximately $\sim \mu$G scale, and the random component is said to be the same (Sokolsky & Thomson 2020). In this study, I only consider the coherent deflection caused by the regular component of the GMF. For the random component of the GMF, we assume the smearing angle θ to be the same as that in previous studies.

3.2.1 Observational constraints on the GMF

A GMF model is constrained by the Faraday rotation measurement (RM) and polarized synchrotron emission (PI) (Klein & Fletcher 2015).

Faraday rotation

When polarized photons from background objects (ex. quasars and pulsars) travel through the galaxy to the earth, the polarized plane rotates due to the existence of the GMF structure. This is called Faraday rotation, and it is one of the most significant constraints on GMF models. Faraday rotation measurement (RM) is expressed as follows (Jansson & Farrar 2012a):

$$\mathrm{RM} = 0.81 \int_0^x n_\mathrm{e} B_\parallel dx \sim 0.81 n_\mathrm{e} B_\parallel L \, [\mathrm{rad} \cdot \mathrm{m}^{-2}] \tag{3.9}$$

Here, n_e is the thermal electron density, and L is the length of the line of sight, respectively.

Polarized synchrotron emission

When a CR electron interacts with magnetic fields, polarized synchrotron emission occurs. Observations of synchrotron emissions in the galaxy can constrain the transverse components of the GMF. The polarized intensity (PI) is written as

$$\mathrm{PI} \sim \int_0^L n_\mathrm{cre}(l) B_\perp(l)^2 dl, \tag{3.10}$$

where n_cre is the relativistic electron density. With a complement of RM, one can estimate the structure of the GMF from the value of the PI.

3.2.2 The Jansson & Farrar 2012 model

The Jansson & Farrar 2012 (JF12) model (Jansson & Farrar 2012a,b) is one of the most widely adapted current GMF models. In the study conducted by these authors,

the JF12 model is used to fit the observational data of the $WMAP7$ (Gold et al. 2011) maps of synchrotron emission, and a 40,403-extragalactic-RM dataset, which was collected from previous observations. For thermal electron density, Jansson & Farrar (2012a) adopt the standard NE2001 thermal electron density model of Cordes & Lazio (2002).

The regular components of JF12 model

The regular components of the JF12 model are composed of the disc component and the halo component. The halo component includes the toroidal halo component and the X-halo component. Here, I briefly summarize the regular component of the JF 12 model shown in Jansson & Farrar (2012a). Jansson & Farrar (2012a) use right-handed Cartesian coordinates (x, y, z), where galactic plane locates in the $x-y$ plane and the earth is located at $(x, y, z) = (-8.5\,\mathrm{kpc}, 0, 0)$. They also use cylindrical coordinates (r, ϕ, z).

The disk component is coherent with the disk of the galaxy and its arms (top panels in Figure 3.4). The disk component is divided into the "molecular ring" ($r = 3-5$ kpc) and the component of eight arms of the galaxy ($r = 5-20$ kpc). The magnetic field strength of molecular ring component is$b_{\mathrm{ring}} = 0.1 \pm 0.1\ \mu$G. The ith spiral region is written as $r = r_{-x}\exp(\tan(90^\circ - i))$ using an opening angle $i = 11.^\circ5$. Note that $r_{-x} = (5.1, 6.3, 7.1, 8.3, 9.8, 11.4, 12.7, 15.5)$ kpc indicates the position where ith arm and $-x$-axis are crossed. The magnetic field strength of ith spiral region is defined by b_i, which is a magnetic field strength at $r = 5$ kpc. The strength b_i is estimated to be $(b_1, b_2, b_3, b_4, b_5, b_6, b_7, b_8) = (0.1 \pm 1.8, 3.0 \pm 0.6, -0.9 \pm 0.8, -0.8 \pm 0.3, -2.0 \pm 0.1, -4.2 \pm 0.5, 0.0 \pm 1.8, 2.7 \pm 1.8)\ \mu$G. The transition condition between disk component and halo component is shown by a following logistic function.

$$L(z, h, w) = (1 + e^{-2(|z|-h)/w})^{-1} \tag{3.11}$$

where h is a transition hight of the disk/halo component, and w is a width of the transition region. For the disk component, they are estimated to be $h_{\mathrm{disk}} = 0.40 \pm 0.03$ kpc, $w_{\mathrm{disk}} = 0.27 \pm 0.08$.

Jansson & Farrar (2012a) defines the toroidal halo component as follows:

$$B_{\phi}^{\rm tor}(r,z) = e^{-|z|/z_0} L(z, h_{\rm disk}, w_{\rm disk}) \times \begin{cases} B_{\rm n}(1 - L(r, r_{\rm n}, w_{\rm n})) & (z > 0) \\ B_{\rm s}(1 - L(r, r_{\rm s}, w_{\rm s})) & (z < 0) \end{cases} \tag{3.12}$$

The magnetic field strength of the toroidal halo in the galactic north (south) is estimated to be $B_{\rm n} = 1.4 \pm 0.1\,\mu$G ($B_{\rm s} = -1.1 \pm 0.1\,\mu$G) with σ uncertainty. The toroidal halo field becomes the larger component at a larger scale and extends to 9.2 kpc in the northern halo and 16 kpc in the southern halo (Jansson & Farrar 2012a).

The X-halo component is an out-of-plane component that shows an X-shaped structure through radio observations (Krause 2009; Beck 2009, Figure 3.5). The X-halo component is separated to be a constant elevation angle region ($r_{\rm p} > r_{\rm X}^{\rm c}$) and varying elevation angle region ($r_{\rm p} < r_{\rm X}^{C}$), where $r_{\rm X}^{\rm c}$ is a galactocentric radius (estimated to be 4.8 ± 0.2 kpc). The constant elevation angle $\Theta_{\rm X}^{0}$ is estimated to be 49 ± 1 deg. The Jansson & Farrar (2012a) describe the magnetic field strength of the $b_{\rm X}$ X-halo using the radius $r_{\rm p}$:

$$b_{\rm X}(r_{\rm p}) = B_{\rm X} e^{-r_{\rm p}/r_{\rm X}}, \tag{3.13}$$

where $B_{\rm X}$ indicates the amplitude of the X-halo component, and $r_{\rm X}$ is an exponential scale length estimated to be 2.9± kpc. In Jansson & Farrar (2012a), the magnetic field strength of the X-halo is derived to be $B_{\rm X} = 4.6 \pm 0.3\,\mu G$ with 1σ uncertainty. In the constant elevation angle region, $r_{\rm p}$ is written as

$$r_{\rm p} = r - |z| / \tan(\Theta_{\rm X}^{0}). \tag{3.14}$$

In the varying elevation angle region, the radius $r_{\rm p}$ and the elevation angle $\Theta_{\rm X}(r,z)$ are described as

$$r_{\rm p} = \frac{r r_{\rm X}^{\rm c}}{r_{\rm X}^{\rm c} + |z| / \tan(\Theta_{\rm X}^{0})} \tag{3.15}$$

and

$$\Theta_{\rm X}(r,z) = \tan^{-1}\left(\frac{|z|}{r - r_{\rm p}}\right), \tag{3.16}$$

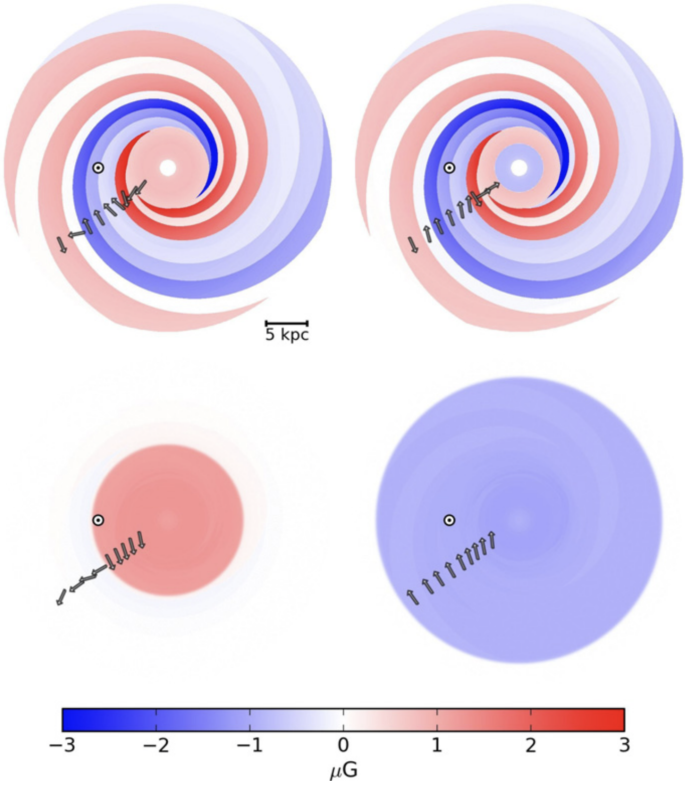

Figure 3.4: The regular coherent GMF component of the Jansson & Farrar 2012 (JF12) model (Figure 7 from Jansson & Farrar (2012a)). The model is shown parallel to the $x-y$ plane (galactic plane), with slices at $z = 10$ pc (top left), -10 pc (top right), 1 kpc (bottom left) and -1 kpc (bottom right). The black point shows the location of the earth at $(x, y, z) = (-8.5\text{kpc}, 0\text{kpc}, 0\text{kpc})$. The top and bottom panels mainly indicates the disk halo component and toroidal halo component, respectively.

respectively.

Farrar (2014) evaluated the uncertainty of the JF12 model using deflections with 60 EV UHECRs (Figure 3.6). The deflection angles are from 0.03° to 1.6°, which become greatest at the galactic plane. Compared to the absolute deflection angle shown in Figure 1.1, we can roughly assume that the uncertainty is less than 10%. In this study, I considered the effect caused by the uncertainty of the JF12 model on the analysis in Sections 4.2.3, 5.1.2, and 5.4.

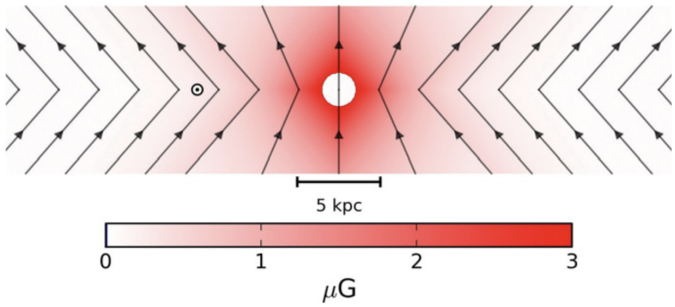

Figure 3.5: The "X-halo" component of the Jansson & Farrar 2012 (JF12) model sliced by the $x - z$ plane (Figure 5 from Jansson & Farrar (2012a)). The red color and black lines indicate the strength and directions of the magnetic field, respectively.

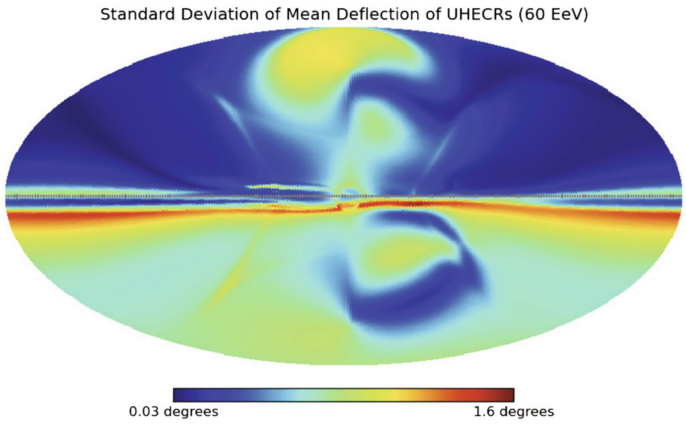

Figure 3.6: The uncertainty of the JF12 model (figure from Farrar (2014)). The colors illustrate the standard deviations of the mean deflection angle of the UHECRs at $R = 60$ EV. See also Figure 1.1 for the original deflection angle of the UHECRs at the same rigidity R.

3.2.3 The Pshirkov & Tinyakov 2011 model

For independent comparison with the JF12 model, I also refer the Pshirkov & Tinyakov 2011 model (PT11) in this study (Pshirkov et al. 2011). PT11 model is based on the two observational datasets of RMs: NRAO VLA Sky Survey (Taylor et al. 2009) and Kronberg & Newton-McGee (2011). PT11 model is also composed of disk component and halo components. I conducted the analysis with the PT11 model for independent comparison with the JF12 model in Sections 4.2.3 and 5.1.3.

3.2.4 Comparison of GMF models

In addition to the JF12 model, there are other GMF model. Although many GMF models are proposed, there are still large uncertainties in them. Farrar (2014) compares three representative GMF models, JF12 (Jansson & Farrar 2012a,b), Sun and Reich 2010 (Sun, X. H. et al. 2008; Sun & Reich 2010, SR10), and PT11 (Pshirkov et al. 2011). Figure 3.7 shows the comparison between the RM of the observational dataset and that of the GMF models. The JF12 model exhibits the best agreement with the observational dataset of the three GMF models, especially with regard to the asymmetric structure with the galactic plane. Based on this study, we adopt the JF12 model as the most commonly adapted GMF model. If there is no reference, I adapt the JF12 model as the GMF model.

3.3 Galactic backtracking of antiprotons using CRPropa3

To account for the coherent deflection caused by the GMF, I introduced a backtracking technique that propagates antiparticles from the earth. I used the cosmic ray propagation code CRPropa3 (Batista et al. 2016). To focus on the effects of the coherent defection caused by the regular component of the GMF, I did not take random components into account. Due to the proximity of the SBGs listed by Aab et al. (2018), I ignored the photodisintegration and the energy loss of UHECRs.

CRPropa3 (Batista et al. 2016) is a public software for the calculation of UHECR propagation. CRPropa3 can calculate the trajectory of primary CRs and secondary

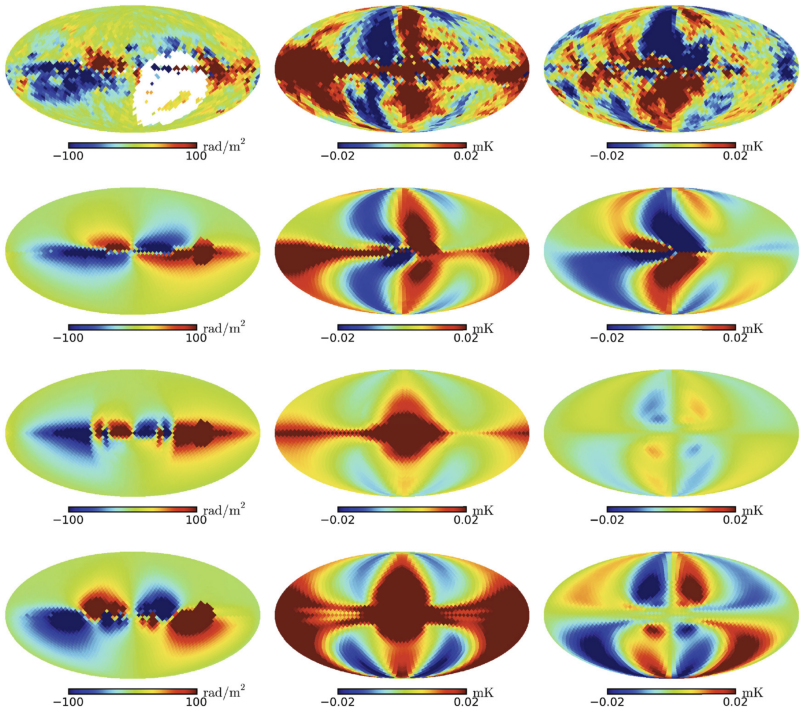

Figure 3.7: A comparison of the representative the observations and GMF models (figure from Farrar (2014)). From left to right, the panels show the RM and stokes parameters Q and U, respectively (in galactic coordinates). From the second row to the bottom row, the JF12, SR10, and PT11 models are shown, respectively.

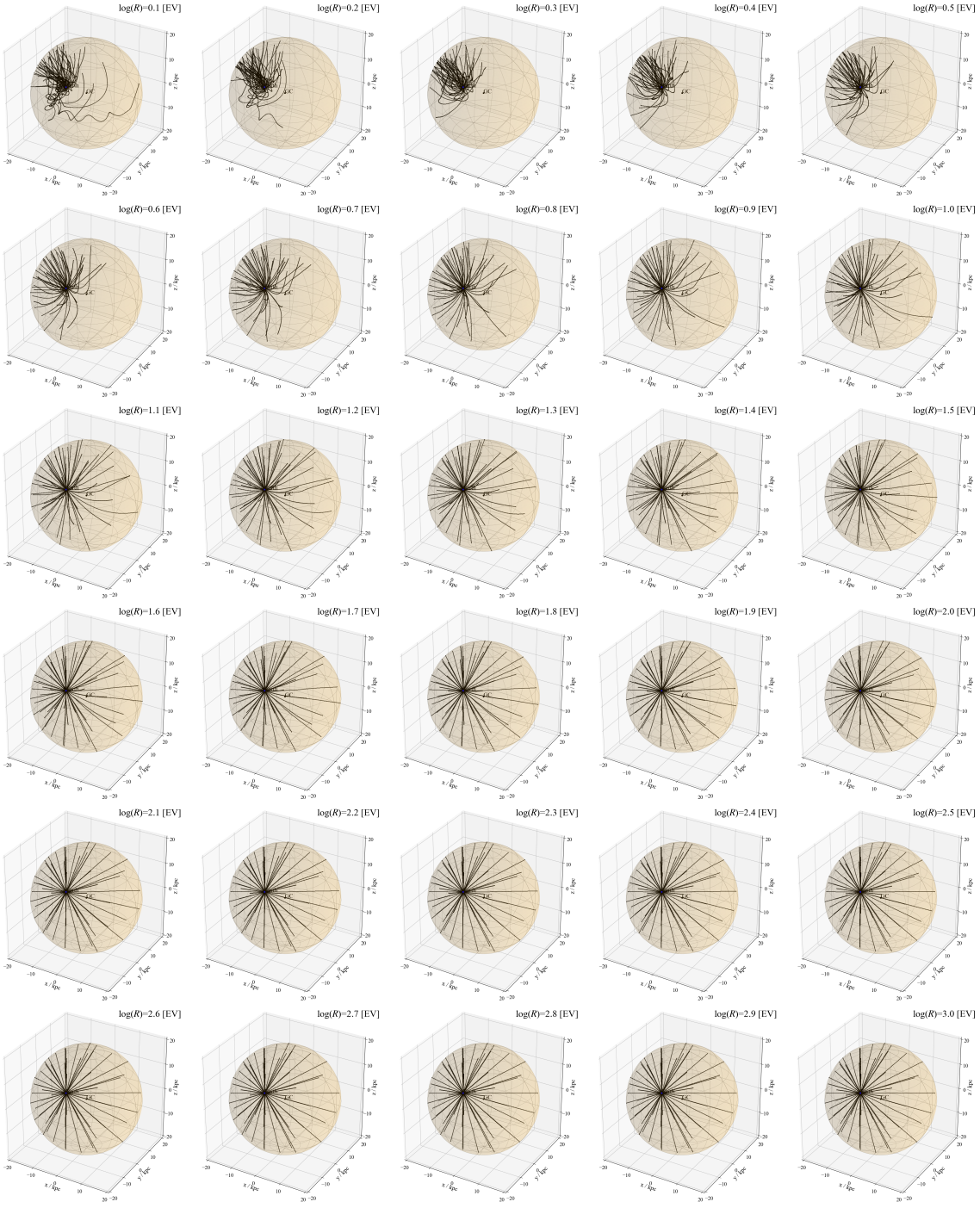

Figure 3.8: The 3D projection of the CR trajectory when $R = 10^{0.1}$ to $10^{3.0}$ EV (black lines, JF12 model). The sphere indicates the galaxy sphere (20 kpc from the GC).

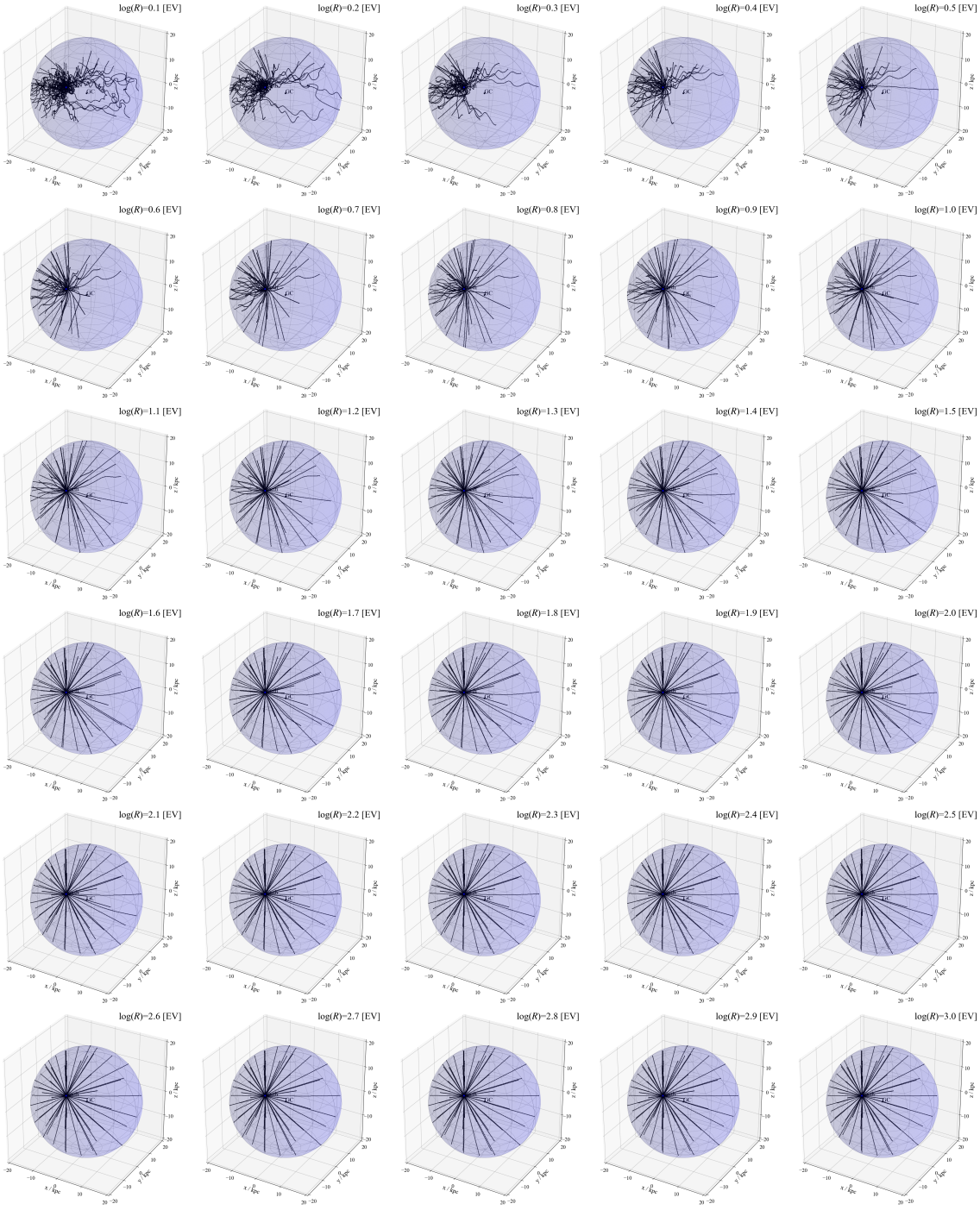

Figure 3.9: Same as Figure 3.8, but for the PT11model.

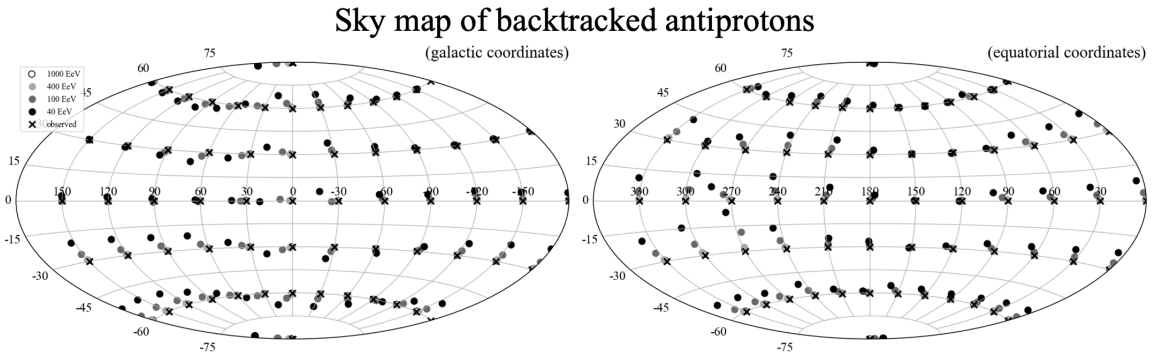

Figure 3.10: A sky distribution of backtracked antiprotons with the JF12 model (left: in galactic coordinates, right: in equatorial coordinates). The black crosses represent the arrival directions on the earth. The white, light gray, gray, and black circles indicate the directions of backtracked antiprotons with energies of 1000, 400, 100, and 40 EeV, respectively.

particles (photons and neutrinos) in a magnetic field. Further, photodisintegrations and energy losses can be included in the calculations. As the GMF models, we can use JF12 and PT11 models.

By propagating the anti-particles through a GMF model from the earth to the arrival direction of UHECRs, I can estimate the trajectory of the UHECRs. I assumed the position of the earth to be 8.5 kpc away from the galactic center (GC). In galactic backtracking, I calculated the trajectories of antiprotons from the earth to 20 kpc from the GC (the galaxy sphere). For heavier-mass particles, I assumed their rigidity R to be E/Ze. Some examples of backtracking of the antiprotons in our galaxy are presented in Figures 3.8 - 3.10. I calculated the trajectories of the antiprotons with $\delta R.A.$ and $\delta Dec. = 1$ deg resolution, with rigidity of $R = E/eZ = 10^{0.1}$ to $10^{3.0}$ EV, and called them CR trajectories. As Figure 3.8 indicates, the deflection caused by the GMF is almost negligible for highest rigidities $R = 10^{3.0}$ EV. However, for extremely low rigidities ($R = 10^{0.1}$ EV for example), the CR trajectories become coherent to the structure of the GMF. When the rigidity is lower than ~ 10EV, most CRs outside the galaxy cannot reach the earth through the GC. This tendency of the CR trajectories is also confirmed in the PT11 model (Figure 3.9). Based on the CR trajectories, I conducted flux mapping (Section 3.4).

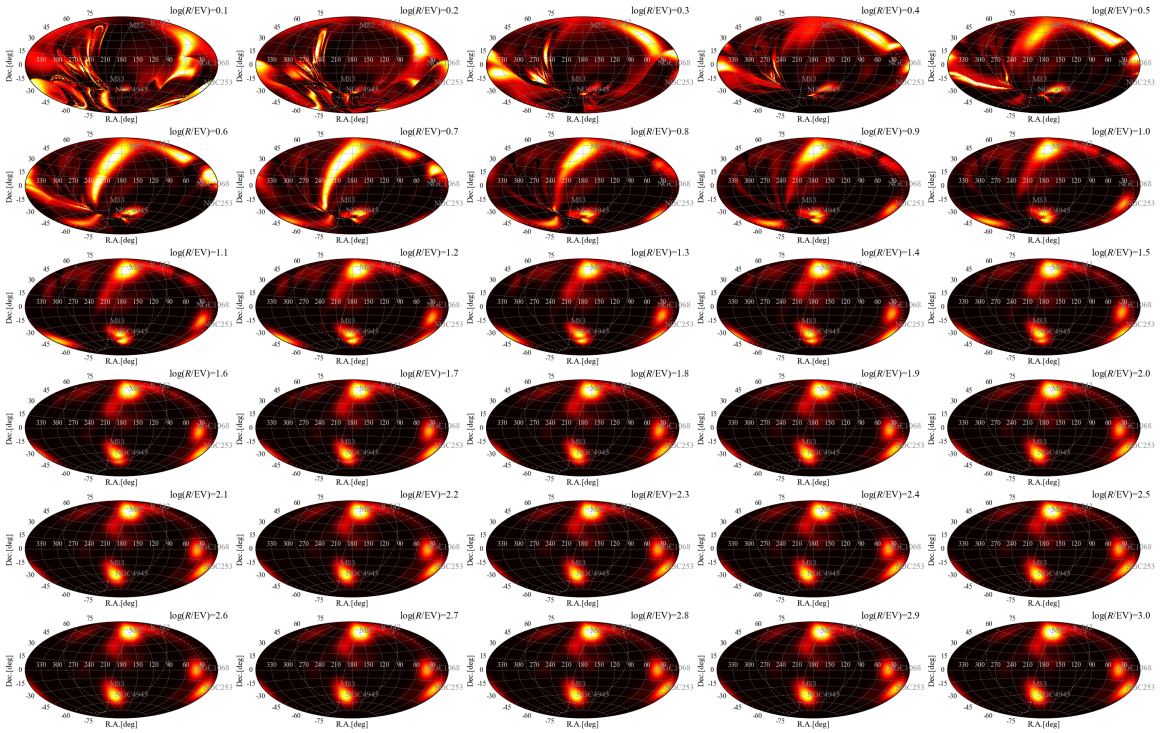

Figure 3.11: The SBG CR flux pattern on the earth when $R = 10^{0.1}$ to $10^{3.0}$ EV and $\theta = 10\,\mathrm{deg}$ (the JF12 model). The color scale is the same as that in Figure 3.1

3.4 Flux mapping: calculation of the CR flux pattern on the earth

Based on the CR trajectory obtained through the backtracking calculation, I converted the flux pattern on the galaxy sphere to that through the GMF (flux mapping). I defined the original CR flux pattern as $F_{\mathrm{org}}(\mathbf{n}_{\mathrm{org}}, \theta)$, where $\mathbf{n}_{\mathrm{org}}$ indicates the direction of the pattern on the galaxy sphere and converted the directions on the earth $\mathbf{n}_{\mathrm{earth}}$ to those on the galaxy sphere $\mathbf{n}_{\mathrm{org}}$ as

$$\mathbf{n}_{\mathrm{org}} = A_{\mathrm{BT}}(\mathbf{n}_{\mathrm{earth}}, R), \tag{3.17}$$

where A_{BT} indicates the backtracking calculation from the earth to the galaxy sphere (examples are shown in Figures 3.8). I calculated the model CR flux pattern on the

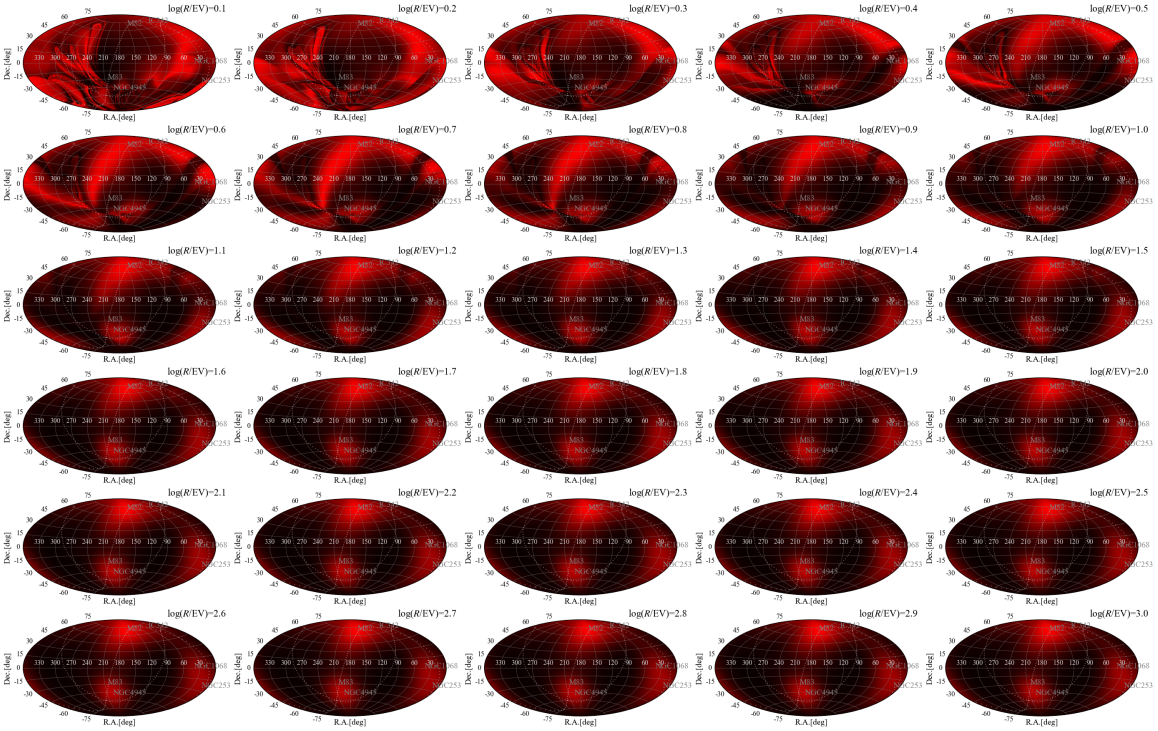

Figure 3.12: Same as Figure 3.11 but for $\theta = 20\,\mathrm{deg}$

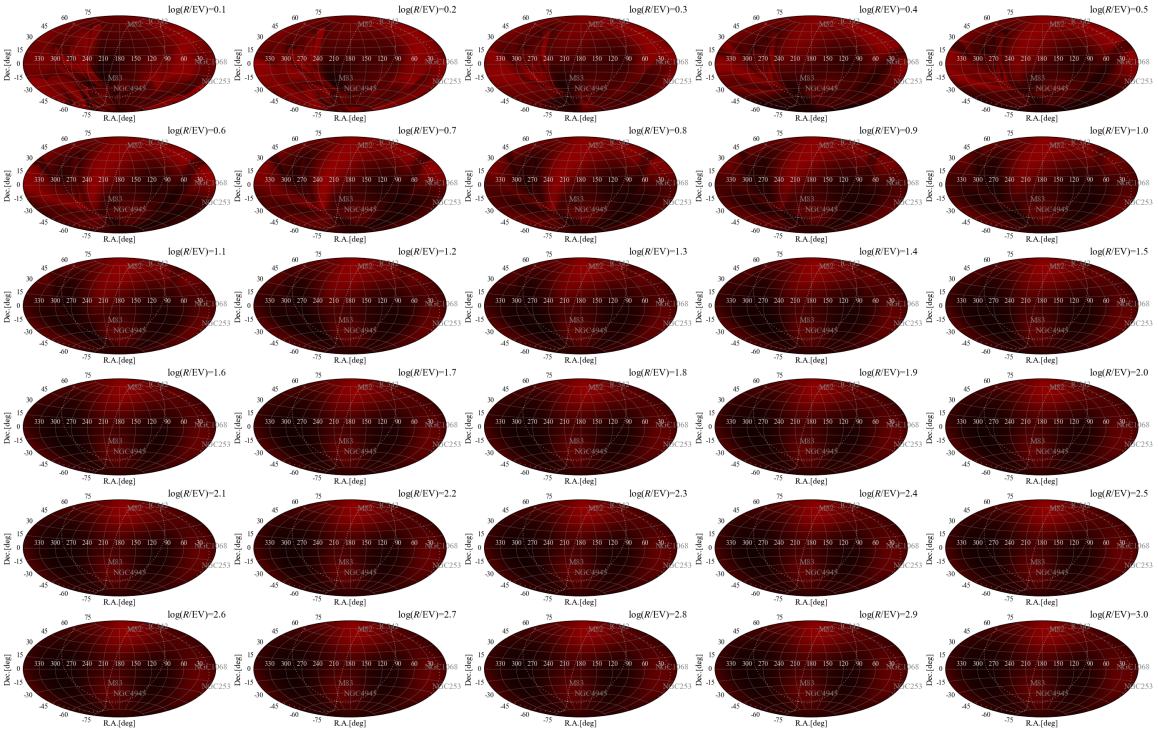

Figure 3.13: Same as Figure 3.11 but for $\theta = 30\,\mathrm{deg}$

earth $F_{\rm earth}$ as

$$F_{\rm earth}(\mathbf{n}_{\rm earth}, \theta, R) = F_{\rm org}(\mathbf{n}_{\rm org}, \theta) = F_{\rm org}(A_{\rm BT}(\mathbf{n}_{\rm earth}, R), \theta). \tag{3.18}$$

According to the Liouville's theorem, the flux value along each CR trajectory remains constant (Bradt & Olbert 2008). Note that, as per the theorem, the GMF itself does not enhance the anisotropy. If we do not assume the random component of the GMF and only consider the coherent deflections caused by the regular component of the GMF model (Equation 3.17), the sufficient condition of Liouville's theorem would be consistent (Ahlers 2014; López-Barquero et al. 2016).

I calculated the CR flux pattern on the earth from $\log_{10}(R/\mathrm{EV}) = 0.1$ to $\log_{10}(R/\mathrm{EV}) = 3.0$ with 0.1 slices with 1 deg resolution. Examples of model CR flux patterns on the earth $F_{\rm earth}$ are shown in Figures 3.11 – 3.13, which were converted from $F_{\rm org}$ in Figure 3.1.

Visually, the GMF effect seems small, above $R = 10^{1.5}$ EV, and a significant displacement of the source location and a deformation of the distribution are seen below this energy. In Chapter 4, the analysis biases present in previous studies are discussed using mock CR events generated from these rigidity-dependent flux patterns. Further, the new analysis technique, which takes these flux maps into account, is proposed in Chapter 5.

CHAPTER 4
GMF BIAS IN PREVIOUS PARAMETER ESTIMATIONS

In this chapter, I reveal how the GMF bias appears in the previous maximum-likelihood analysis discussed in Section 3.1. First, I generate mock UHECR datasets with a coherent deflection by the GMF based on the flux pattern on the galaxy sphere that was calculated by flux mapping (Section 4.1). Next, I test the maximum-likelihood technique in Section 3.1 on the mock UHECR datasets (Section 4.2). I then obtain the best-fit parameters and evaluate the GMF bias based on the difference between the true parameters and the estimated parameters. The same analysis is used in previous studies, I do not consider the deflection caused by the GMF in the maximum-likelihood method used in this chapter.

4.1 Generation of mock UHECR datasets

To generate mock events with the consideration of coherent deflections caused by the GMF, we need to assume the rigidity R of each event. I assumed the pure-mass assumption (Section 4.1.1) and mixed-mass composition (Section 4.1.2) in this study. In any case, I generated 1000 datasets, each of which contains 4000 mock UHECR events (all-sky dataset). To compare the datasets with the observed UHECR events from the TA and Auger experiments, I selected the north-sky and south-sky datasets from the all-sky datasets based on the sky coverage of each experiment (Section 4.1.3).

4.1.1 Pure-mass assumption

As the simplest case, I assumed a pure-proton, He, C, Si, and Fe assumption to produce mock UHECR datasets. I adapted a broken-power law spectrum in the spectral index with $\gamma = -2.69$ and $\gamma = -4.63$, broken at $E = 10^{19.81}$ eV (Tsunesada et al. 2017, Figure 4.1). From the broken-power law spectrum, the energies of the mock UHECRs are randomly distributed. In any case, the rigidities of the mock UHECRs are obtained through the formula $R = E/Ze$. As a minimum energy threshold of the datasets, I used $E_{\rm min} = 40$ EeV, which corresponds to $E_{\rm min}$ =39 EeV in previous

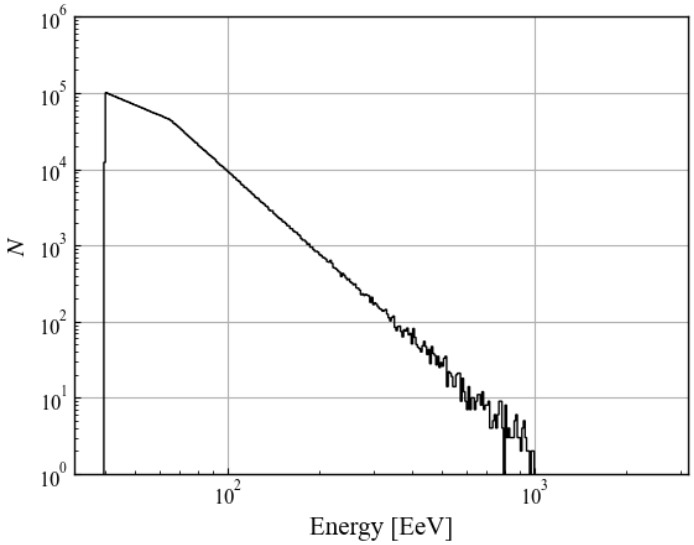

Figure 4.1: Example of energy histogram of 1000 datasets (4,000,000 events) with pure-mass assumption.

analyses (Aab et al. 2018). I have presented an example of an energy histogram for 1000 mock datasets (4,000,000 events) in Figure 4.1.

Using the randomly distributed rigidity R, I determined the arrival direction of the event based on the model CR flux pattern defined in Section 3.4. Due to the discrete values of rigidity R in the calculation of $F_{\rm earth}$, I interpolated the flux value as

$$F_{\rm earth}(\mathbf{n}_{\rm earth}, R) = (1-\alpha) * F_{\rm earth}(\mathbf{n}_{\rm earth}, R^i) + \alpha * F_{\rm earth}(\mathbf{n}_{\rm earth}, R^{i+1}), \qquad (4.1)$$

where R^i is the discrete value of a rigidity of flux patterns ($\log_{10}(R^i/{\rm EV}) = 0.0, 0.1, ..., 3.0$ for $i = 0, 1, ..., 30$) and

$$\alpha = \frac{\log_{10}(R/{\rm EV}) - \log_{10}(R^i/{\rm EV})}{\log_{10}(R^{i+1}/{\rm EV}) - \log_{10}(R^i/{\rm EV})} \ (R^i < R < R^{i+1}). \qquad (4.2)$$

Based on the interpolated model CR flux pattern $F_{\rm earth}$, I determined the arrival direction of each particle randomly.

Examples of the distribution of mock UHECR datasets with pure-mass assumption where ($f_{\rm ani}$, θ) = (100%, 10 deg) are shown in Figure 4.2. Visually in pure-P and

pure-He assumptions, the distributions of mock UHECR events reflect the original CR flux pattern $F_{\rm org}$ in Figure 3.1. In these cases, most of the mock UHECR events concentrate on the directions of the top four contributing SBGs: M82, NGC4945, NGC253, and NGC1068. In pure-C and pure-Si assumptions, the distributions of mock UHECR events from M82 move to the south. In pure-Fe assumption, we cannot see a significant excess of events around the direction of M82 and NGC 4945.

4.1.2 Mixed-mass assumption

To reflect a more realistic mass composition than the pure-mass assumption, I also generated datasets with a mixed-mass assumption. To define the energy spectrum of each kind of mass, I used a best-fit function and parameters from the work of Heinze & Fedynitch (2019), who derived best-fit functions and parameters based on UHECR data from the Auger experiment. In Heinze & Fedynitch (2019), the mass dependent energy spectrum at the source was assumed by the following function, and fitting was performed for the UHECR composition observed on the earth. The combined-fit function (CF) J_A is written as Equation 4.3 (Figure 4.3).

$$J_A(E) = \mathcal{J}_A f_{\rm cut}(E, Z_A, R_{\rm max}) n_{\rm evol}(z) \left(\frac{E}{10^9 \text{ GeV}} \right)^{-\gamma} \tag{4.3}$$

Here, $\mathcal{J}_A$ is the normalized parameter of emitted particles from the source (nuclear fraction) and $f_{\rm cut}$ cutoff function (Equation 4.4). Heinze & Fedynitch (2019) assume nuclear types A as ^{1}H, ^{4}He, ^{14}N, ^{28}Si, and ^{56}Fe. The cutoff function $f_{\rm cut}$ is written as follows:

$$f_{\rm cut} = \begin{cases} 1 & (E < Z_A R_{\rm max}) \\ \exp\left(1 - \frac{E}{Z_A R_{\rm max}}\right) & (E > Z_A R_{\rm max}) \end{cases} \tag{4.4}$$

$n_{\rm evol}(z)$ is a redshift-dependent parameter for source evolution.

$$n_{\rm evol}(z) = (1+z)^m \tag{4.5}$$

As I only considered the nearby source candidates, I ignored the redshift evolution in this study. I also assumed that the mass composition observed on the earth and that on the source are the same. This is because of the large contribution of nearby SBGs. The fractions of elements are defined as f_A=$\mathcal{J}_A/\Sigma_A\mathcal{J}_A$ at 10 EeV. I adapted the best-fit parameters from Table 3 in Heinze & Fedynitch (2019), $\gamma = -0.80$ and $R_{\rm max} = 1.6$ EeV. I also adapted the values of f_A as (^{1}H, ^{4}He, ^{14}N, ^{28}Si, ^{56}Fe) = $(0.0, 82.0, 17.3, 0.6, 2.0 \cdot 10^{-2})$[%]. To determine the mass composition of all the mock datasets, I needed to derive the integral fraction I_A, which is defined as an integral from minimum energy $E_{\rm min}$. The integral fraction I_A is defined as

$$I_A = \frac{\int_{E_{\rm min}}^{\infty} J_A(E) E dE}{\Sigma_A \int_{E_{\rm min}}^{\infty} J_A(E) E dE}, \tag{4.6}$$

where I choose $E_{\rm min}$=40 EeV (same as Section 4.1.1). The derived values of the integral fractions I_A from Equation 4.6 are (^{1}H, ^{4}He, ^{14}N, ^{28}Si, ^{56}Fe) = $(0.0, 0.01, 63.9, 30.8, 5.3)$[%].

The procedure followed for the generation of the mock UHECR datasets with the mixed-mass assumption is as follows: First, I randomly choose the nuclear type Z based on the I_A. Depending on the nuclear type Z, I assume an energy spectrum in Equation 4.3 and choose energy E at random. I calculate the rigidity ($R = E/Ze$) of an event based on derived parameters (Z, E) and generate the CR flux pattern with R from Equations 4.1 and 4.2 in Section 4.1. In the same manner as Section 4.1, I choose the arrival direction of the anisotropic event based on the generated CR flux patterns $F_{\rm earth}$. An example of an energy histogram of 1000 datasets with the mixed-mass assumption is shown in the right panel of Figure 4.3, and an example of the distribution of the mock events is provided in Figure 4.4.

I have assumed the isotropic and anisotropic events have the same mass composition, which is not a trivial assumption. It is difficult to estimate the anisotropy of the mass composition of UHECRs from the current observations. It is expected that the future improvement of event-by-event mass resolution in the observations and low-cost FD arrays can constrain the anisotropy of the mass composition (see also Chapter 6).

4.1.3 Selection of mock UHECR events based on the sky coverage of experiments

The number of CR events observed on the earth is limited by the sky coverage of experiments. The sky coverage of an experiment depends on its latitude and maximum zenith angle. To make the comparison with the analysis of the observed UHECR events (Aab et al. 2018; Abbasi et al. 2018), I considered the sky coverage of the TA and Auger experiments based on Equations 3.6 in Section 3.1 (Sommers 2001). I adopted a latitude of an experiment $a_0 = 39.^\circ3$ $(-35.^\circ2)$ and a maximum zenith angle $\theta_{\rm m} = 55^\circ$ (60°) for the TA (Auger) experiment. Figure 4.5 illustrates a declination dependence of the relative sky coverage of each experiment. The value of each coverage is scaled by the maximum value of the coverage for the north sky. From the all-sky datasets, I randomly selected mock UHECR events with the probability of each sky coverage. Out of the 4000 mock UHECR events in each dataset, approximately 1000 mock events were selected by the coverage of the TA and Auger experiments. I define the datasets selected by the sky coverage of the TA (Auger) experiment as the north-sky (south-sky) datasets.

4.1.4 Procedure of GMF bias evaluation

In this section, I describe the procedure used for the analysis of the mock UHECR datasets in the next section. I applied the maximum-likelihood analysis from Section 3.1 to each dataset generated in Section 4.1. I defined the true values as $(f_{\rm ani}^{\rm true}, \theta^{\rm true})$, which are used to generate a mock dataset in Section 4.1. I estimated the best-fit parameter $(f_{\rm ani}, \theta)$ that maximizes the TS for the north-sky, south-sky, and all-sky datasets. Next, I conducted the parameter estimation for all 1000 datasets and created a set of 1000 best-fit parameters $(f_{\rm ani}, \theta)$ for each sky. As Figure 4.6 shows, I calculated a median value $(\tilde{f_{\rm ani}}, \tilde{\theta})$ for each sky. I evaluated the effect of the GMF bias using an offset, which is defined as $(\Delta f_{\rm ani}, \Delta\theta) = (\tilde{f_{\rm ani}} - f_{\rm ani}^{\rm true}, \tilde{\theta} - \theta^{\rm true})$.

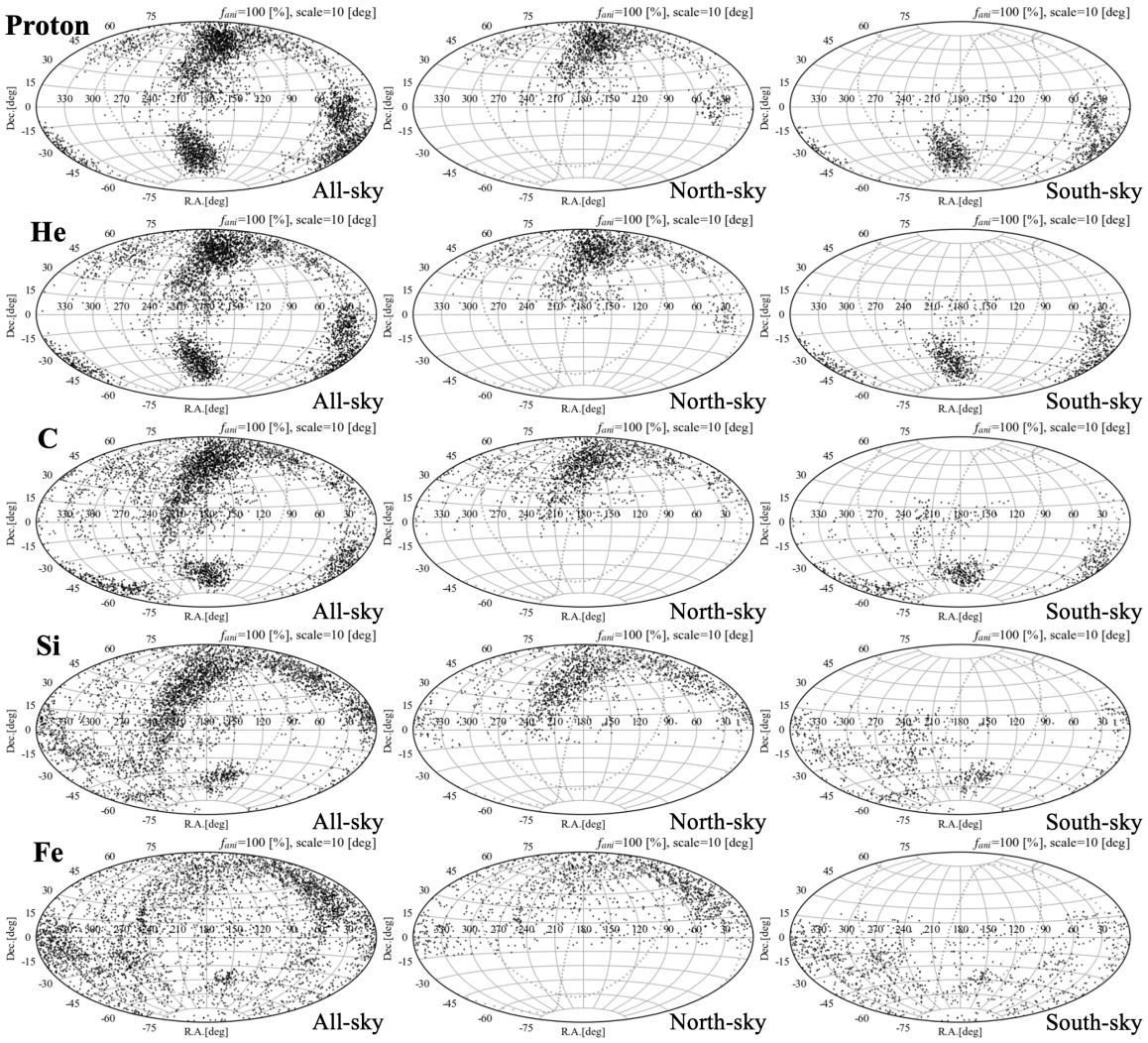

Figure 4.2: Examples of the distribution of the mock UHECR datasets ($f_{\rm ani}^{\rm true} = 100\%$, $\theta^{\rm true}$=10 deg and 4000 event over all-sky). From top to bottom, the distribution of datasets with pure-P to pure-Fe assumption are shown. The left panels indicate the distribution of the all-sky datasets. The middle and right panels show the north-sky and south-sky datasets which are selected from the all-sky datasets, respectively.

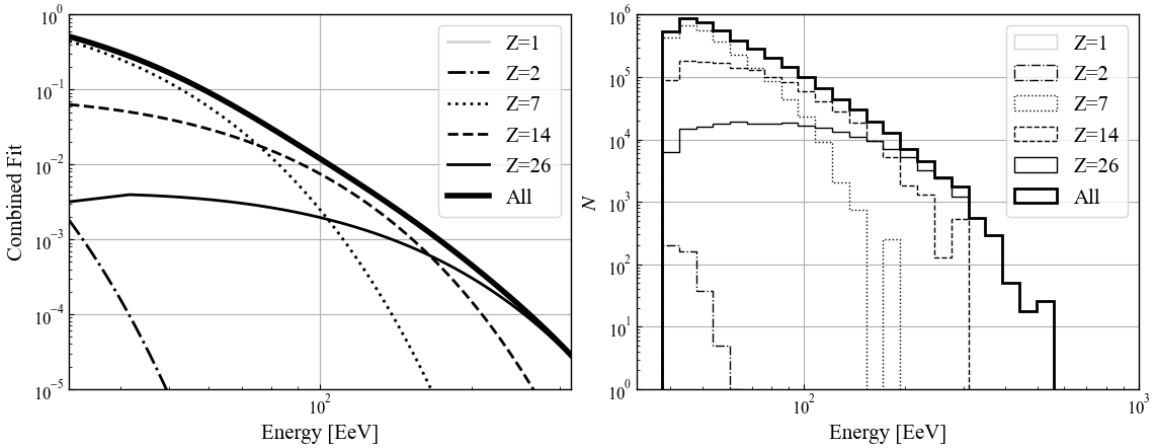

Figure 4.3: Composition of each mass group (left panel, Equation 4.3) and energy histogram of 1000 datasets (4×10^6events) based on the mass composition taken from the work of Heinze & Fedynitch (2019) (right panel). The thick black solid line shows the distribution of all mass types. The thin dash-dot, dotted, dashed, and solid lines indicate $Z = 2$, $Z = 7$, $Z = 14$, and $Z = 26$, respectively. The proton ($Z = 1$) does not exist in these figures due to the small fraction $f_A = 0\%$.

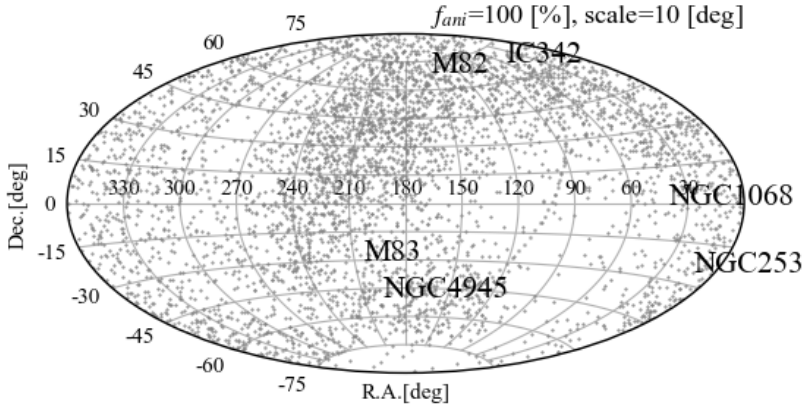

Figure 4.4: Example of the mock UHECRs distribution with the mixed-mass assumption ($f_{\rm ani}^{\rm true}$=100%, $\theta^{\rm true}$ = 10 deg). The gray dots show the arrival directions of 4000 mock UHECR events. The directions of the SBGs whose contribution is above 5% are shown.

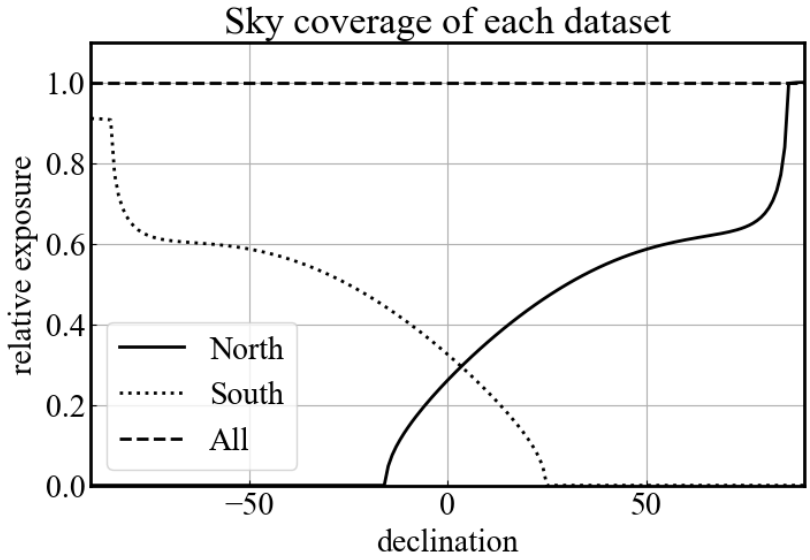

Figure 4.5: Declination dependence of the sky coverage derived from Equations 3.6 (Sommers 2001). The solid, dotted, and dashed lines show the relative sky coverage for north-, south-, and all-sky datasets, respectively. Each coverage is scaled by the maximum value of north-sky coverage.

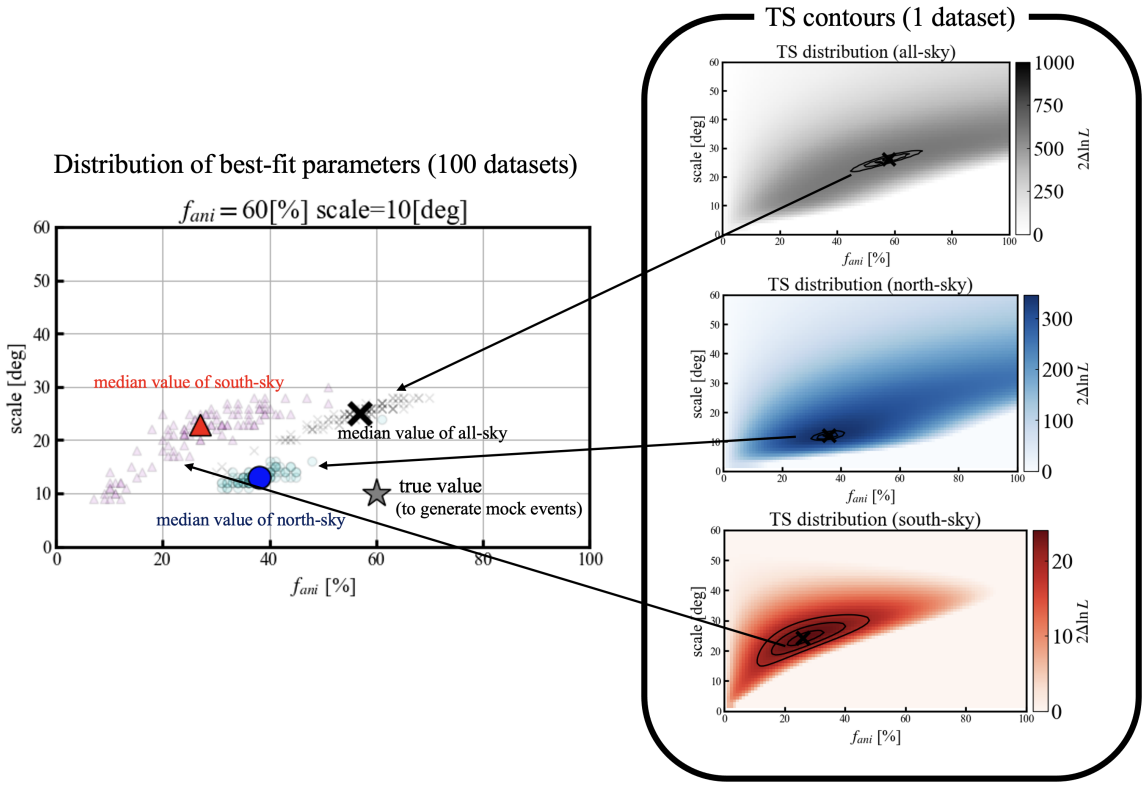

Figure 4.6: Demonstration of parameter estimation for the mock UHECR datasets (mixed-mass assumption, 100 datasets with $f_{\rm ani}^{\rm true}$=60% and $\theta^{\rm true}$ =30 deg). The right panels show the TS distributions for the all-sky, north-sky, and south-sky analysis for one example dataset. The best-fit parameter $(f_{\rm ani}, \theta)$ giving the maximum TS value is picked up as a representative of this example dataset and plotted in the left panel. In this plot, 100 datasets are analyzed and plotted in the left. Median values of 100 results are defined as $(\tilde{f_{\rm ani}}, \tilde{\theta})$ and plotted as large markers.

4.2 Features of the GMF bias in previous parameter estimations

In this section, I show the results of previous parameter estimations on the mock UHECR datasets from Section 4.1, where mock events are generated through GMF deflection but the analysis does not consider the GMF effect.

4.2.1 Estimated parameters in previous parameter estimations

Figures 4.7 -4.11 show the results of the parameter estimation for the mock UHECR datasets with the pure-mass assumption (Section 4.1.1). In the pure-proton and pure-He assumptions, there is a small GMF bias. For a larger separation angular scale θ, the dispersion of the estimated parameters becomes larger. The pure-C assumption (Figure 4.9) shows different distributions between the north-sky and south-sky datasets. This tendency continues for the heavier pure-mass assumptions. For heavier assumptions, the south-sky datasets present 0% of the anisotropic fraction in any set of input parameters (Figures 4.10 and 4.11). In any dataset, the estimated parameters from the north-sky datasets are closer to those of the all-sky datasets than those of the south-sky datasets. This may due to the single CR contribution from the SBGs (M82) in the north sky.

Figure 4.12 is the same as Figure 4.7 but for the mixed mass composition in Section 4.1.2. In the mixed-mass assumption, the distributions of estimated parameters $(f_{\rm ani}, \theta)$ in all-sky, north-sky, and south-sky datasets do not agree with each other.

4.2.2 Offset of the GMF bias

In this section, I summarize the GMF bias shown in Section 4.2.

I have shown the offsets $(\Delta f_{\rm ani}, \Delta\theta)$ for the pure-mass datasets from Section 4.1.1 in Figures 4.7 - 4.11. The estimated parameters are not consistent with each other across the north-, south-, and all-sky datasets.

The offset $(\Delta f_{\rm ani}, \Delta\theta)$ for the mixed-mass composition datasets from Section 4.1.2 are shown in Figure 4.14. In any case, the estimated parameters for the south sky are

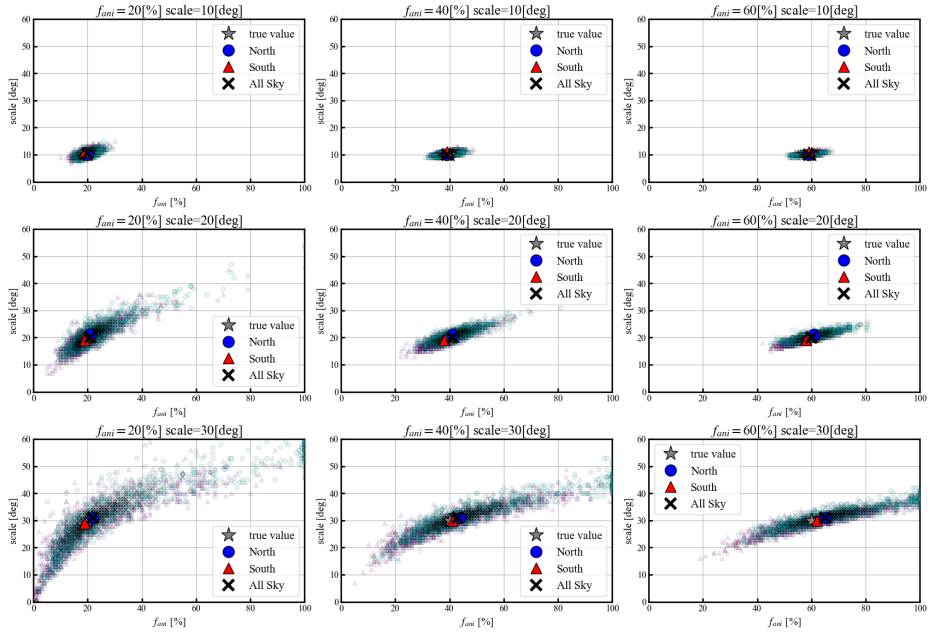

Figure 4.7: Results of the parameter estimation for the mock UHECR datasets with the pure-proton assumption. The gray star indicates the input parameter $(f_{\rm ani}^{\rm true}, \theta^{\rm true})$ that is used to generate the mock UHECR datasets. The black cross (crosses), blue circle (circles), and red triangle (triangles) in light (thick) color show the median value of the best-fit parameters of each (all 1000) all-sky, north-sky, and south-sky datasets, respectively.

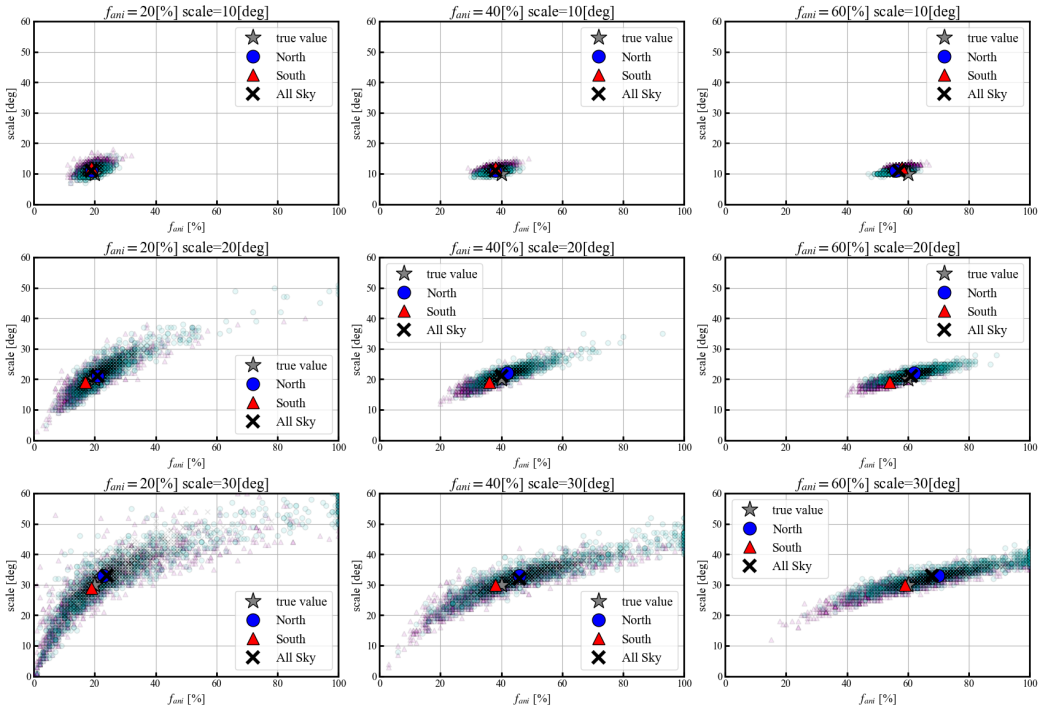

Figure 4.8: Same as Figure 4.7 but for the pure-He assumption.

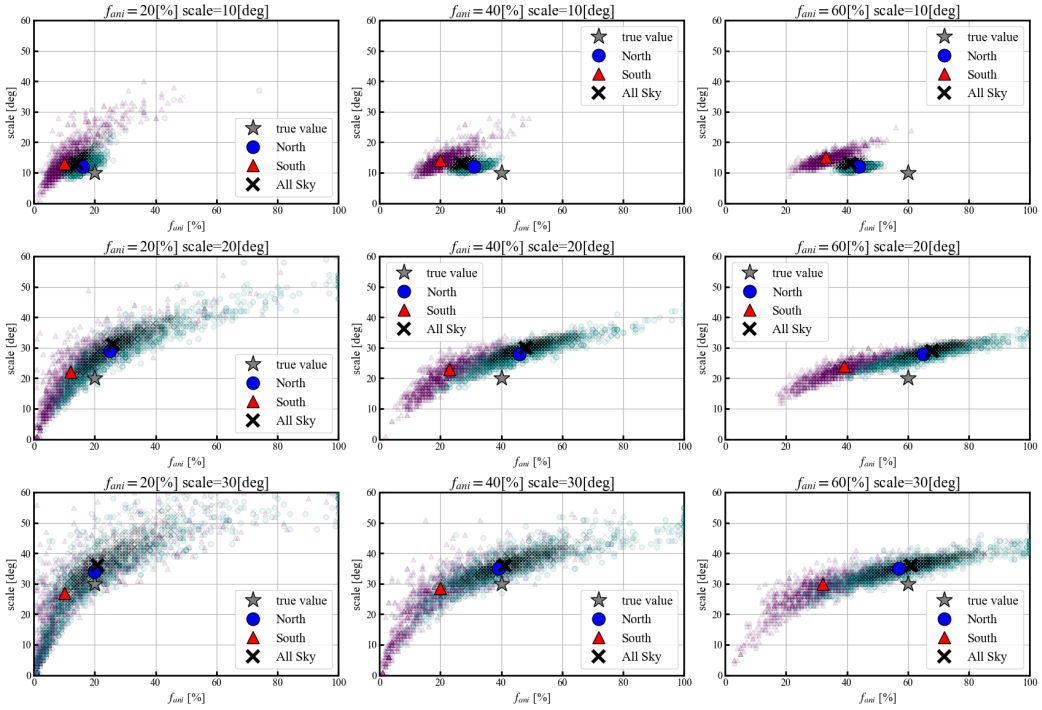

Figure 4.9: Same as Figure 4.7 but for the pure-C assumption.

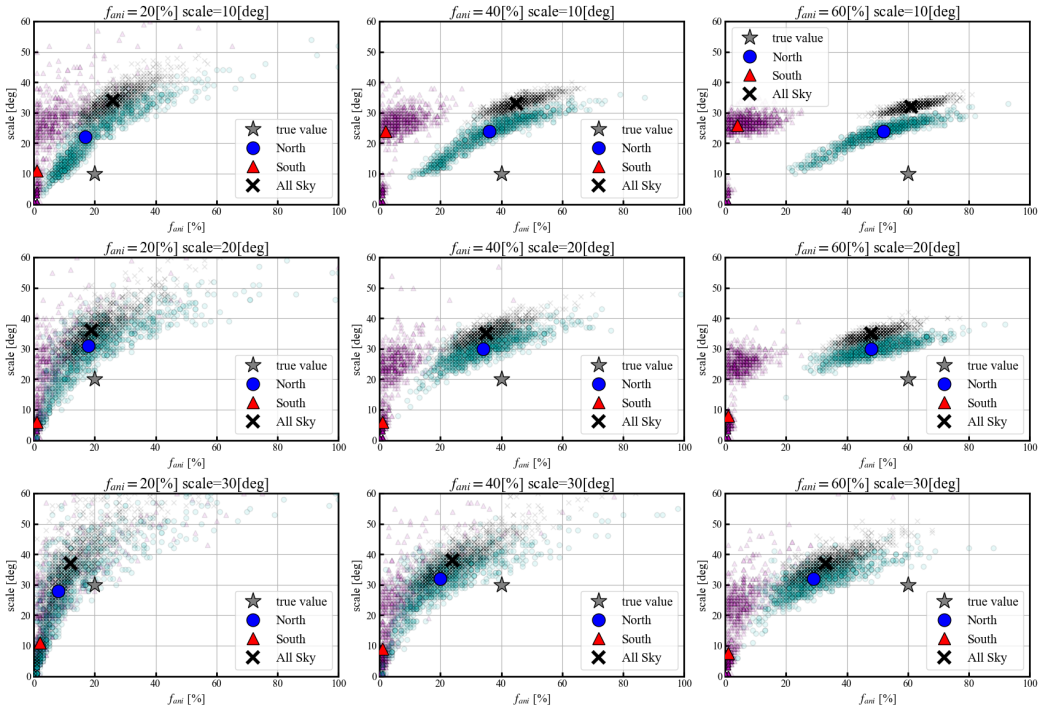

Figure 4.10: Same as Figure 4.7, but for pure-Si assumption.

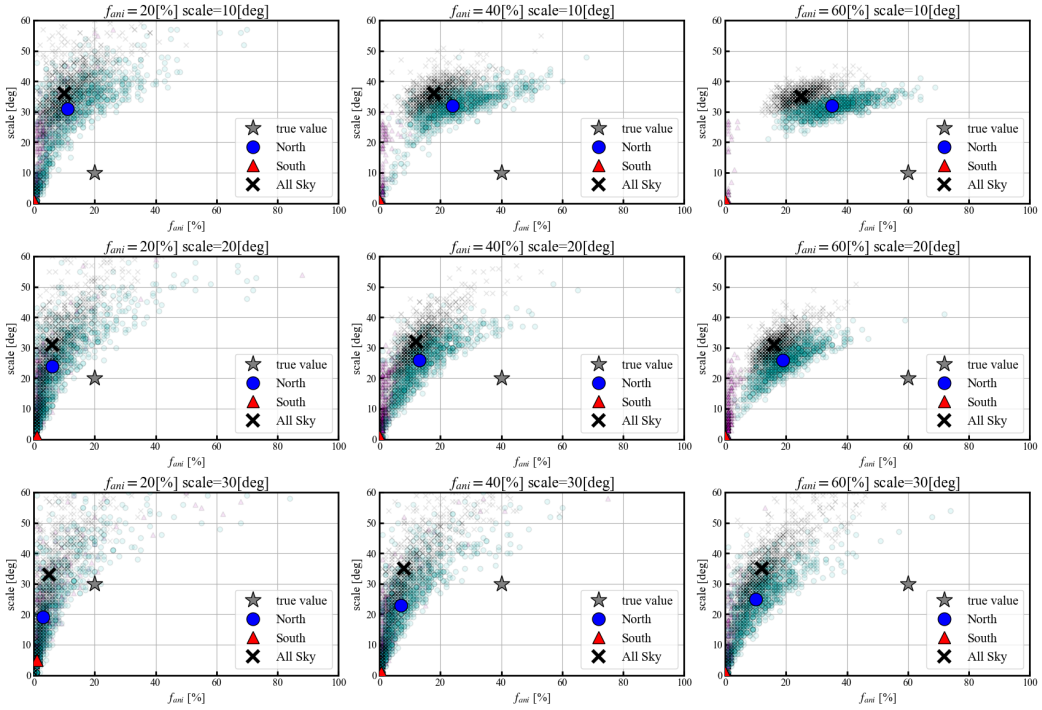

Figure 4.11: Same as Figure 4.7 but for the pure-Fe assumption.

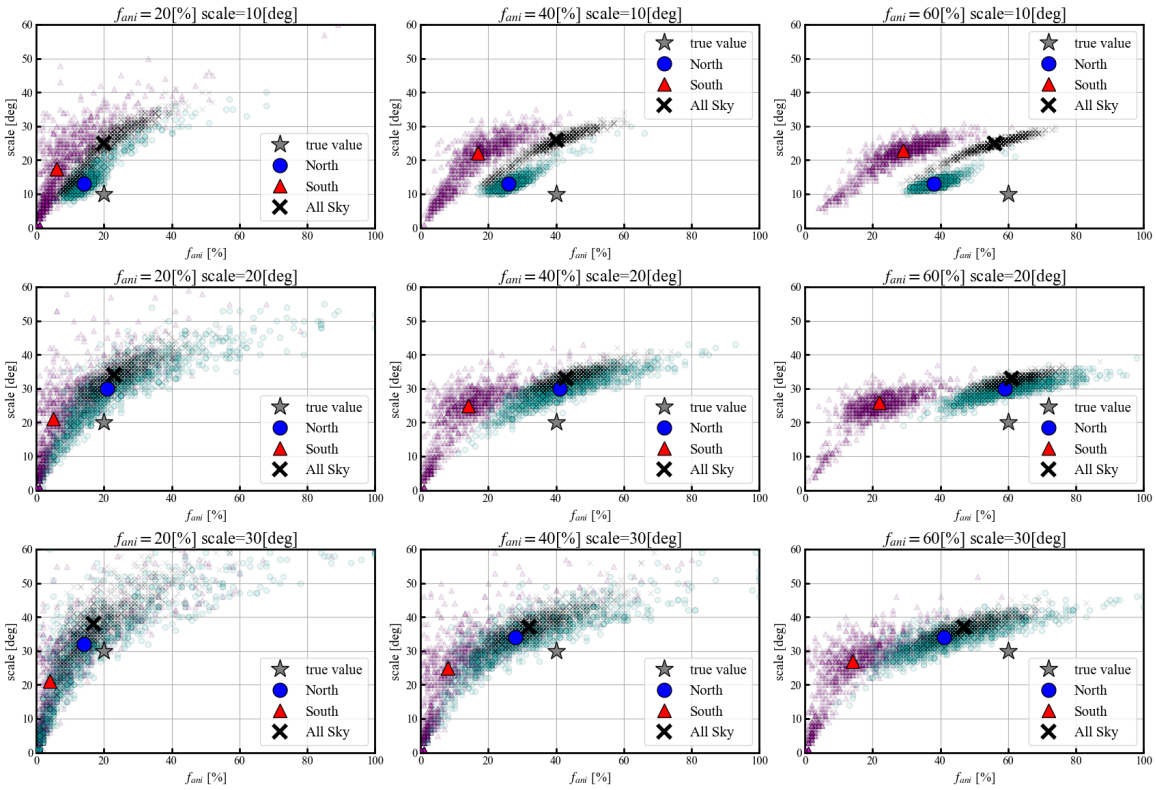

Figure 4.12: Same as Figure 4.7 but for the mixed-mass assumption.

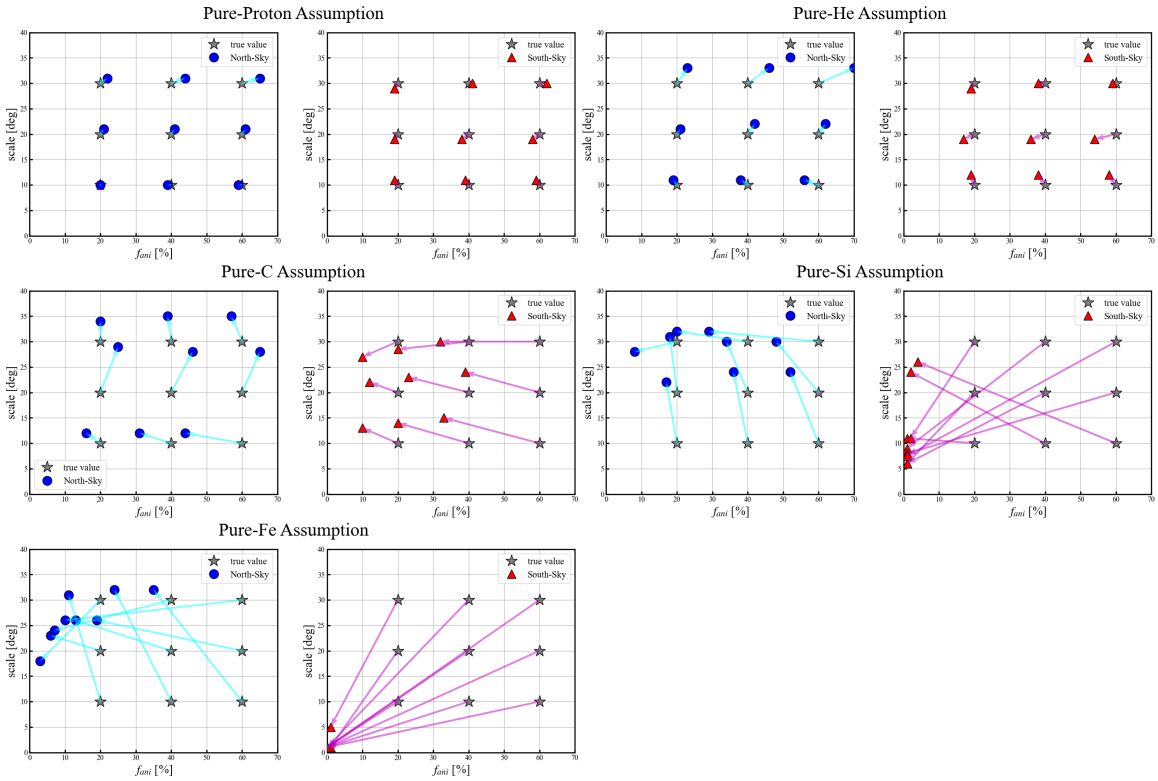

Figure 4.13: Offsets $(\Delta f_{\rm ani}, \Delta\theta)$ caused by the GMF bias in Figures 4.7 - 4.11. The gray star indicates the input parameter that is used to generate the mock UHECR datasets. The blue circles and red triangles show the median values $(\tilde{f_{\rm ani}}, \tilde{\theta})$ of all 1000 north-sky and south-sky datasets shown in Figures 4.7 - 4.11, respectively.

below 50% of $f_{\rm ani}^{\rm true}$. Regardless of the input parameters $(f_{\rm ani}^{\rm true}, \theta^{\rm true})$, the estimated parameters concentrate in a narrow region around $(f_{\rm ani}, \theta) = (5-30\%, 5-30\ {\rm deg})$. Interestingly, the best-fit parameters $(f_{\rm ani}, \theta) = (9.7\%,\ 12.9\ {\rm deg})$ obtained by Aab et al. (2018) are in this region. The true parameters may be strongly biased by the GMF. In the next step, the effect (GMF bias) needs to be examined (see Chapter 5).

4.2.3 The uncertainty of the GMF models

In this section, I discuss the effect of the uncertainty in the GMF models.

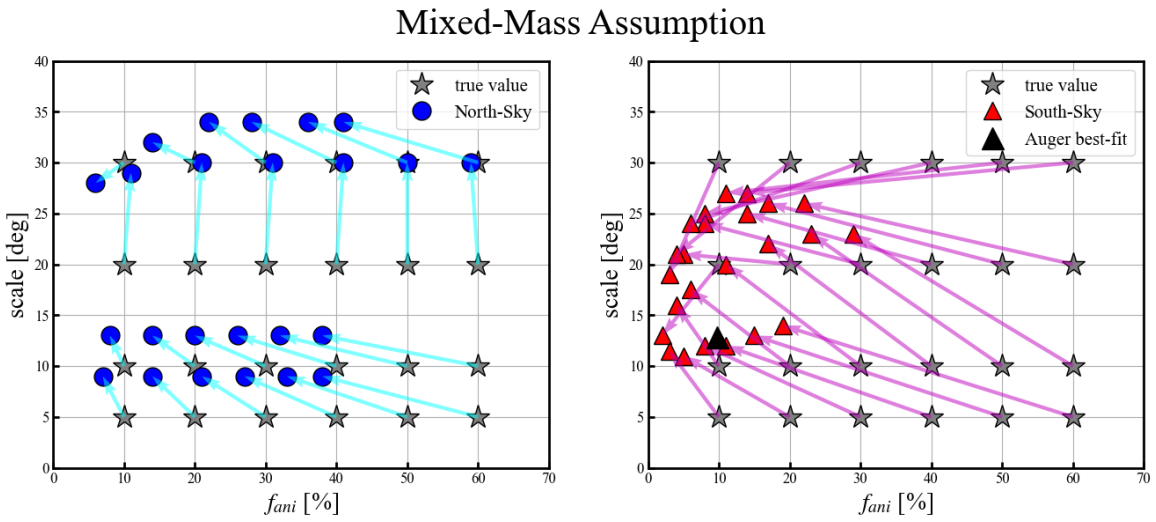

Figure 4.14: Same as Figure4.13, but for the mixed-mass assumption. The black triangle in the left panel indicates the Auger best-fit parameter $(f_{\rm ani}, \theta) = (9.7\%, 12.9\,{\rm deg})$.

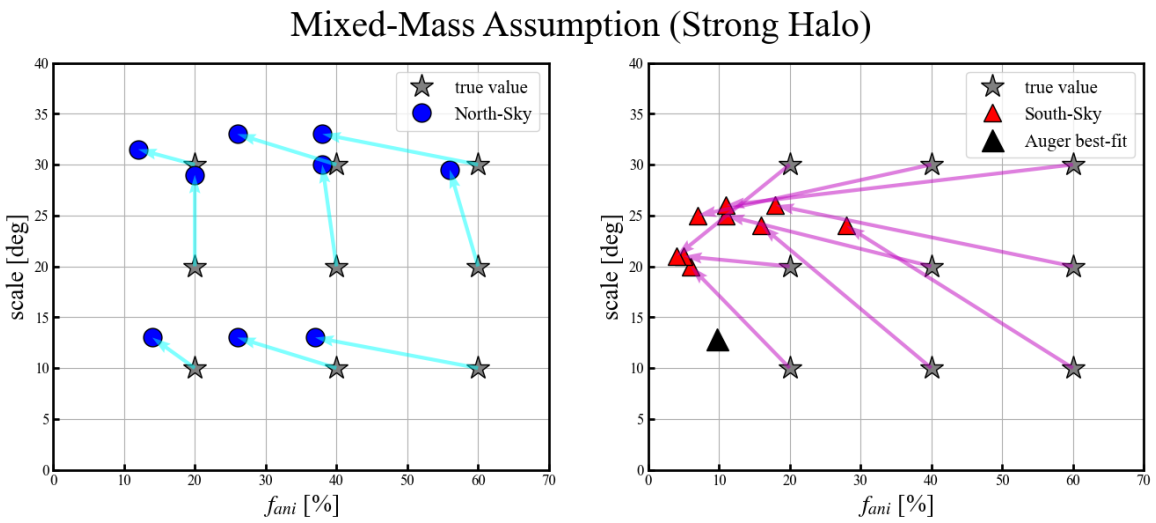

Figure 4.15: Same as Figure4.14, but for the strong halo model.

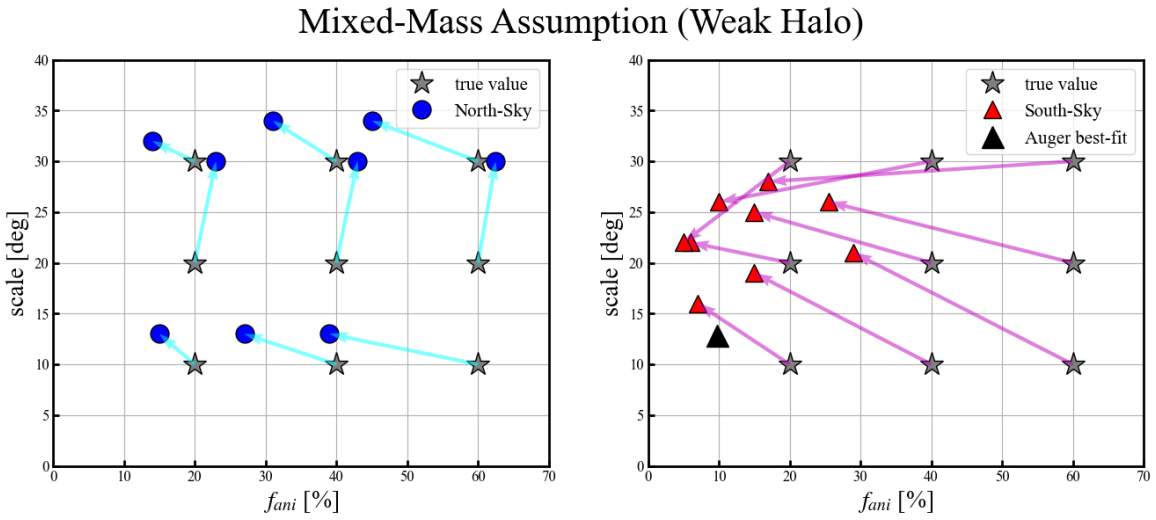

Figure 4.16: Same as Figure4.14, but for the weak halo model.

The uncertainty of the JF12 model

To test the effects caused by the uncertainty of the JF12 model, I conducted the same analysis in this chapter but changing the halo components in the model. I changed the toroidal and X-halo components stronger/weaker within 1σ uncertainties (the strong halo model / weak halo model) and generated the mock datasets with the mixed-mass assumption. For the strong (weak) halo model, I changed the set of parameters $(B_{\rm n}, B_{\rm s}, B_{\rm X}) = (1.4, -1.1, 4.6)$ μG to $(B_{\rm n}, B_{\rm s}, B_{\rm X}) = (1.5, -1.2, 4.9)$ μG ($(B_{\rm n}, B_{\rm s}, B_{\rm X}) = (1.3, -1.0, 4.3)$ μG). Figures 4.15 and 4.16 show the results of the analysis with the strong halo model and the weak halo model, respectively. It is found that the value of the halo components does not affect the offset values.

The independent analysis with the PT11 model

For an independent comparison with the JF12model, I performed the same analysis with the PT11 model. I generated the mock datasets based on the PT11 model, assuming the mixed-mass assumption. Except for the GMF model to generate the mock UHECR datasets, the other assumptions are the same. Figures 4.17 and 4.18 shows the results with PT11 model. Although the separation angular scale θ in the south-sky datasets gets smaller than those with the JF12model, the anisotropic

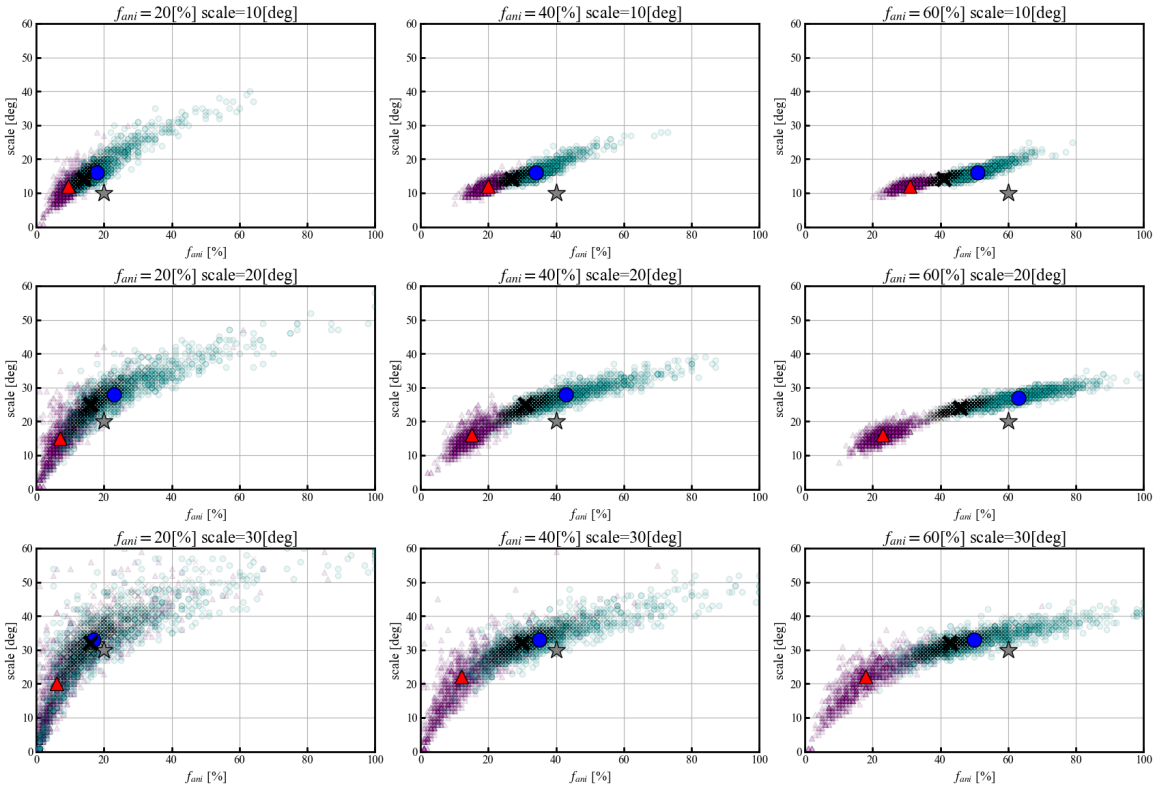

Figure 4.17: Same as Figure 4.12 but for the mock datasets generated with the PT11 model.

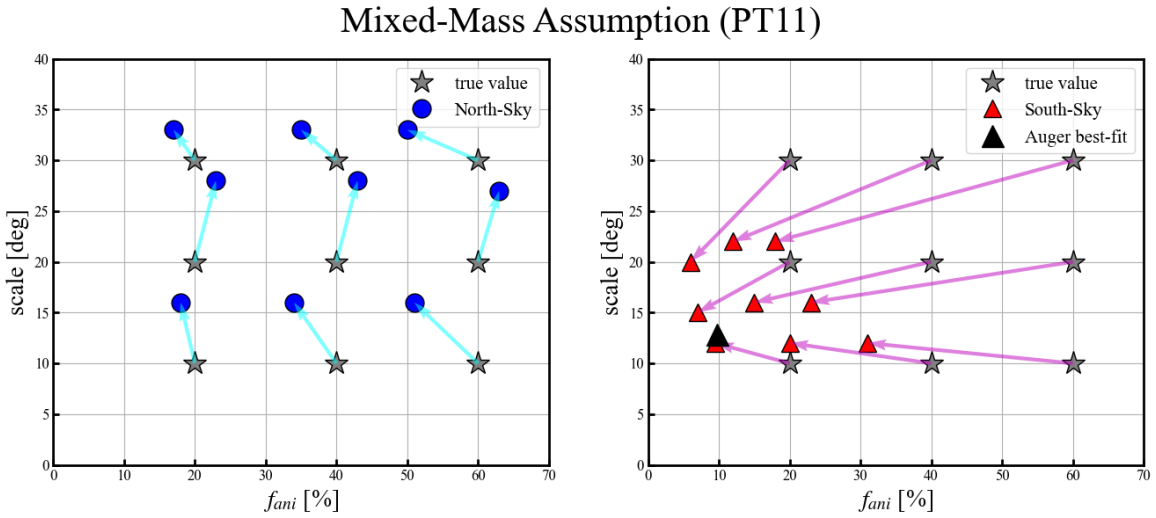

Figure 4.18: Same as Figure 4.14, but for the mock datasets generated with the PT11 model.

fractions $f_{\rm ani}$ also decrease less than $\sim 50\%$ of the true value $f_{\rm ani}^{\rm true}$.

4.2.4 Test statistics (TS) comparison

To determine the TS range that I would obtain from the observational datasets with SBG and isotropic models, I investigate the TS distributions of the mock observational datasets in the same manner as Abbasi et al. (2018). I generated the mock UHECR datasets with mixed-mass assumptions, the same number of events, and the threshold energy of those of the Auger 2015 and TA-11yr datasets as shown in Table 3.1. I refer to them as the mock Auger 2015 dataset and the mock TA-11yr dataset. Figures 4.19 and 4.20 show the TS distributions obtained for the mock Auger 2015 and TA 11yr datasets in previous parameter estimations. The TS values of the experimental data $TS_{\rm obs}$ are also indicated by arrows. Although the experimental test statistics $TS_{\rm obs}$ exceed the TS average of the isotropic model, it is not significantly high to support the SBG model. With a smaller anisotropic fraction $f_{\rm ani}$, previous parameter estimation could not separate the TS distributions of the SBG and isotropic models. In the next chapter, I discuss the separation of the TS distributions with consideration of the GMF bias and constrain the models.

4.3 Summary of this chapter

In this chapter, I applied the previous parameter estimation (Section 3.1) to the mock UHECR datasets with the pure-mass and mixed-mass assumptions. Using the rigidity-dependent flux maps developed in Section 3.4, the mock UHECR datasets were generated through the GMF coherent deflection, while the analysis does not consider this effect. In case of pure-proton and pure-helium assumptions, the estimated parameters well reproduce the true parameters $(f_{\rm ani}^{\rm true}, \theta^{\rm true})$. On the other hand, heavier assumptions resulted in strongly biased estimations or a loss of sensitivity to the true values, especially in the south-sky pure-iron case. In the mixed-mass case, regardless of the true parameters, the median values of the estimated parameters $(\tilde{f_{\rm ani}}, \tilde{\theta})$ are biased around the best-fit parameters $(f_{\rm ani}, \theta)$=(9.7%, 12.9 deg) of Aab et al. (2018) in the analysis of the south-sky datasets. I also conducted the

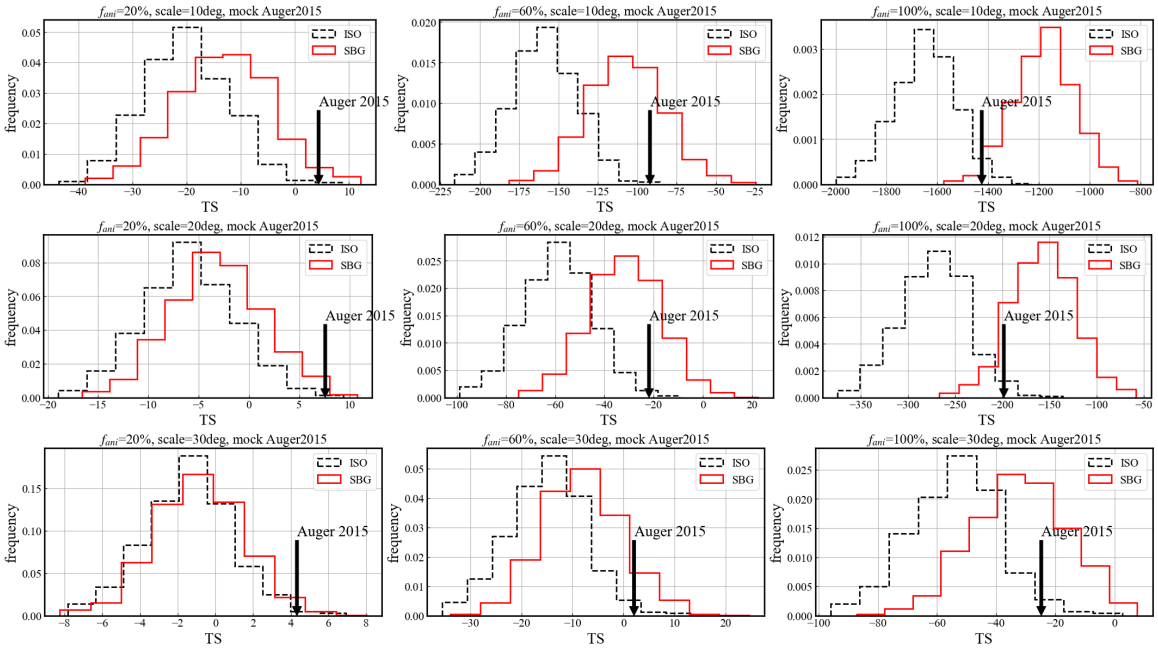

Figure 4.19: Examples of the TS distributions of the mock Auger 2015 datasets in the previous parameter estimation with the omission of the GMF bias. The TS distribution for the isotropic model and SBG model is shown using a black dashed line and a red solid line, respectively. Each panel shows the case with the true value of $(f_{\rm ani}^{\rm true}, \theta^{\rm true})$. The black arrow indicates the TS value of the observational dataset $(TS_{\rm obs})$.

analysis with the JF12 model changing the halo components within 1σ uncertainty and the PT11 model. Although there are small differences in estimated parameters, the qualitative tendencies are the same. It is concluded that the GMF bias is not negligible in the parameter estimations carried out using the SBG model.

I also checked the TS distributions of the mock observational datasets, which were generated from the isotropic model and SBG model. Here, the energy thresholds and the number of events in the Auger and TA analyses, as summarized in Table 3.1, are taken into account. As a result, it is found that the separation between the two models is difficult for the case of the Auger best-fit parameters. In the next chapter, we discuss the reduction of the GMF bias and the separation of the isotropic and SBG models using the TS distributions.

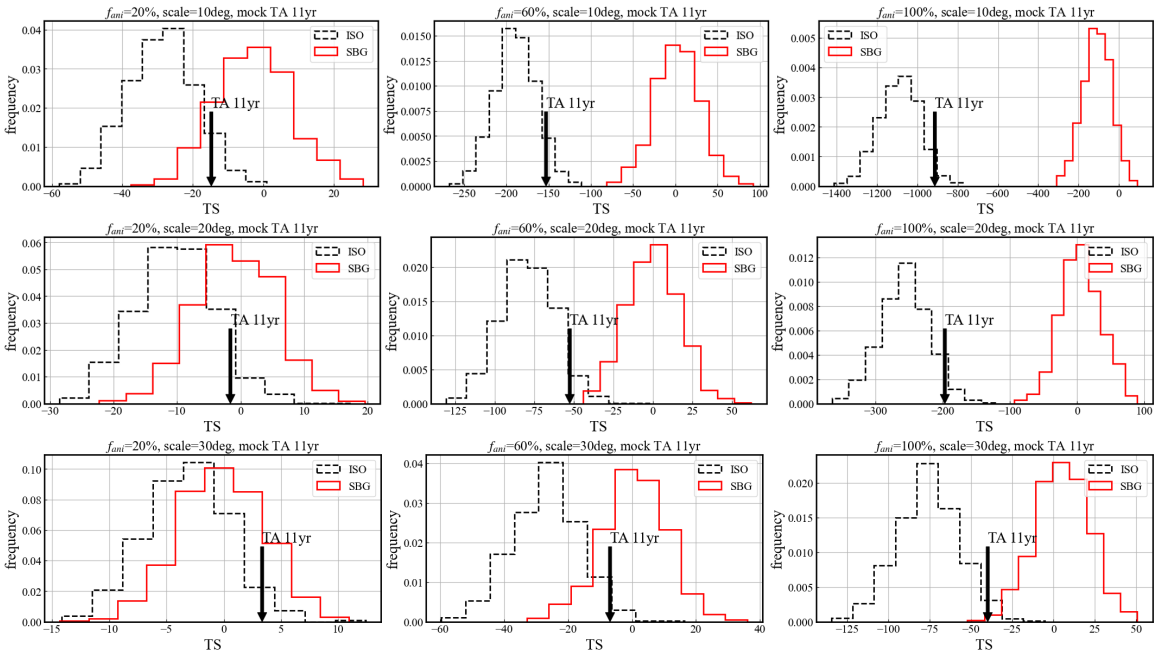

Figure 4.20: Same as Figure 4.19 but for the mock TA-11yr dataset (previous parameter estimation).

CHAPTER 5
NEW ANALYSIS METHODS WITH A REDUCTION IN THE GMF BIAS

In Chapter 4, I revealed the existence of the GMF bias and its features. In this chapter, I will discuss how the GMF bias can be reduced.

To reduce the GMF bias, I developed a new likelihood analysis with the convolution of the rigidity spectrum (Section 5.1). By applying the new technique to the same mock datasets in Chapter 4, I tested by how much the GMF bias can be reduced (Section 5.1.1). I also applied the technique to the actual observational datasets that were introduced in Section 3.1.3 (Section 5.2). By comparing the $TS_{\rm obs}$ and TS distribution of mock observational datasets, I tested the effect of the new technique (Section 5.2.4). I also conducted the estimation of parameter space $(f_{\rm ani}, \theta)$, where the SBG model can be excluded from the current observational datasets (Section 5.3).

I introduce the following three methods, which depend on the properties and constraints of the datasets and observations (Table 5.1).

Method 1: In an ideal scenario where the mass A (charge Z) and energy E of individual particle are known, we conduct an analysis with the convolution of the rigidity $R = E/Ze$ of each event (Section 5.1).

Method 2: In a realistic scenario where we do not know the event-by-event mass A but only the energy E, we sum the model CR flux pattern $F_{\rm earth}(R)$ with mass probability $p^A(E_{\rm CR}, Z^A_{\rm CR})$ and conduct the analysis (Section 5.2).

Method 3: For future prospects, we conduct the analysis from Method 1 that we know the event-by-event mass A with an uncertainty (Section 6.2 in Chapter 6).

In this chapter, I discuss Methods 1 and 2 in detail.

Table 5.1: Constraints on the methods of a new technique for the GMF reduction

	mass A	mass uncertainty $\Delta \ln A$ [b]	energy E
method 1	known	$\Delta \ln A = 0.0$	known
method 2	not known	$\Delta \ln A = \infty$	known
method 3	known [a]	$\Delta \ln A = 10\%$–70%	known

[a] With an uncertainty $\Delta \ln A$.

[b] We assume the Gaussian distribution of $\ln A$ with a standard deviation of $\Delta \ln A$.

5.1 Method 1: maximum likelihood analysis method with CR flux patterns on the earth

For the calculations of likelihood (Equation 3.5) and TS (Equation 3.4), I used the original model CR flux pattern $F_{\rm org}$ instead of the model CR flux pattern on the earth $F_{\rm earth}$ (Equation 3.2). This caused the GMF bias in the parameter estimations. To reduce the GMF bias in the previous parameter estimation, it is necessary to rewrite $F_{\rm org}$ to $F_{\rm earth}$ in Equation 3.2. We rewrite Equation 3.2 as follows:

$$F_{\rm norm}(\mathbf{n}, f_{\rm ani}, \theta, R) = f_{\rm ani} F^{'}_{\rm earth}(\mathbf{n}, \theta, R) + (1 - f_{\rm ani}) F_{\rm iso} \tag{5.1}$$

$$F^{'}_{\rm earth} = \frac{F_{\rm earth}(\mathbf{n}, \theta, R)}{\int_{4\pi} F_{\rm earth} d\Omega},\ F_{\rm iso} = 1/4\pi \tag{5.2}$$

Here, $F_{\rm earth}(\mathbf{n}_{\rm earth}, \theta, R)$ is obtained using Equation 3.18. Thus, we can rewrite the model CR flux patterns from the sources $F^{'}_{\rm earth}(\mathbf{n}, f_{\rm ani}, \theta, R)$ as

$$F^{'}_{\rm earth}(\mathbf{n}_{\rm CR}, f_{\rm ani}, \theta, R_{\rm CR}) = \frac{F_{\rm org}(A_{\rm BT}(\mathbf{n}_{\rm CR}, R_{\rm CR}), \theta)}{\int_{4\pi} F_{\rm org}(A_{\rm BT}(\mathbf{n}, R), \theta) d\Omega}. \tag{5.3}$$

The denominator $\int_{4\pi} F_{\rm org}(A_{\rm BT}(\mathbf{n}, R), \theta) d\Omega$ in Equation 5.3 is derived by integrating $F_{\rm earth}$, which is interpolated, in Equations 4.1 and 4.2 in Section 4.1.1.

5.1.1 Estimated parameters taking into account the GMF bias

I show the results of the likelihood analysis with $F_{\rm earth}$ (Method 1) for the pure-mass assumption in Figures 5.1 - 5.3. I applied Method 1 to the same datasets used in Chapter 4. The analysis of Method 1 is carried out assuming that we know the mass of each mock event.

In general, Method 1 improves the estimated parameters $(f_{\rm ani}, \theta)$. Even for cases of heavier particle, the anisotropic fraction $f_{\rm ani}$ does not biased to $f_{\rm ani} = 0\%$. Specifically, the GMF bias is reduced in smaller separation angular scales θ. For a larger separation angular scale, there is still a significant difference between the estimated parameters and the input parameters. For the heavier mass assumption, this difference becomes even greater. For the heavier mass and the larger separation angular scale, the estimated parameters in the south-sky datasets align with those of the all-sky datasets and the true parameters more than those of the north-sky datasets.

Figure 5.4 illustrates the results of the analysis for the mixed-mass assumption. Further, I summarize the offsets of the analysis (Method 1) in Figure 5.5. Although the offset caused by the regular component of the GMF is effectively reduced within 68 percentile, the dispersions caused by the random component and the statistical uncertainty are not significantly improved. Future observations with large statistics are expected to reduce the dispersion. The offsets at larger separation angular scales are expected to be reduced in the all-sky datasets (bottom panel in Figure 5.5).

I summarize the offsets $(\Delta f_{\rm ani}, \Delta\theta)$ in previous parameter estimations (Chapter 4) and those derived by Method 1 $(\Delta f_{\rm ani}^{\rm NEW}, \Delta\theta^{\rm NEW})$ in Table 5.2. If we assume the all-sky datasets, Method1 can improve the offset of the anisotropic fraction $\Delta f_{\rm ani}$ by less than 5% and that of the separation angular scale $\Delta\theta$ by less than 2 degrees.

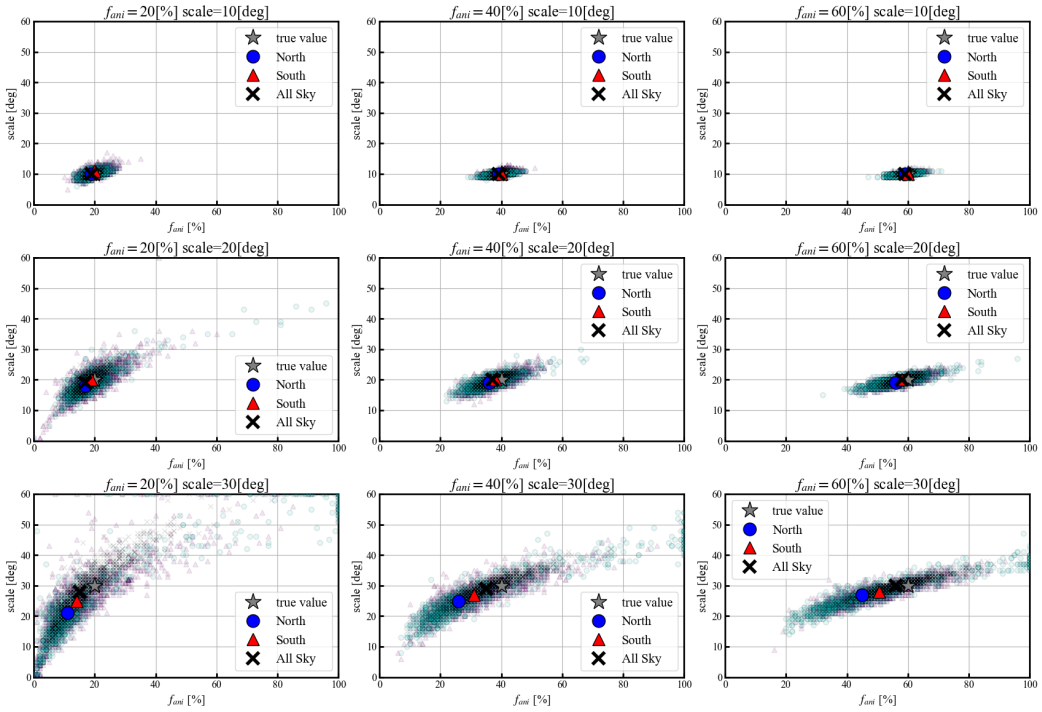

Figure 5.1: Same as Figure 4.7 but for the pure-C assumption and likelihood analysis with F_{earth}.

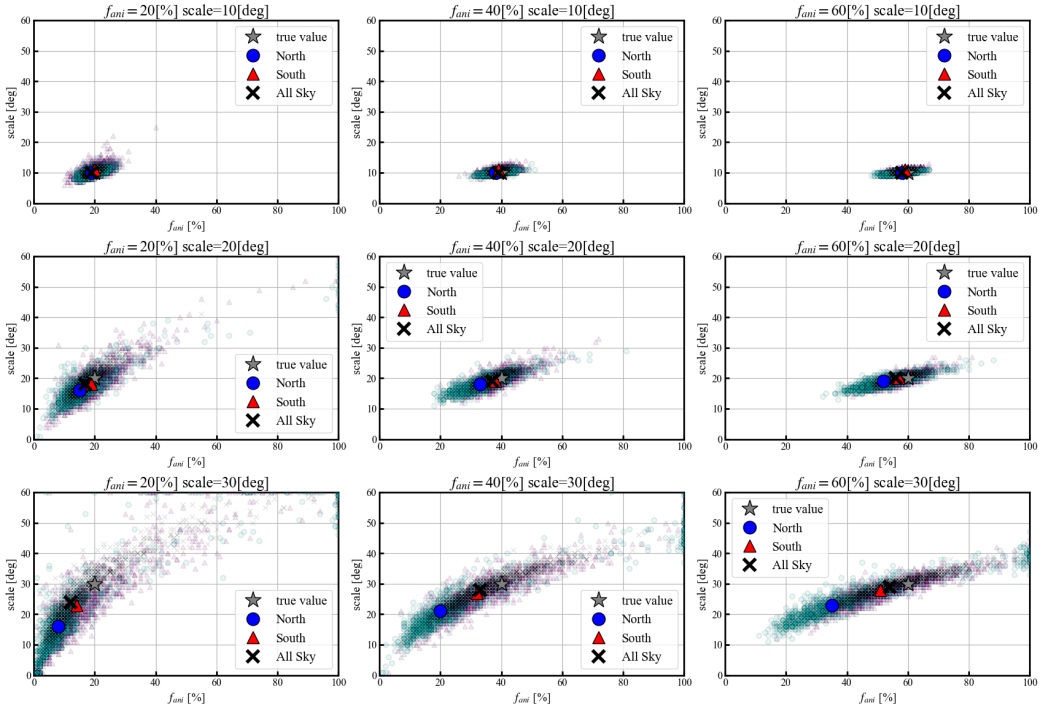

Figure 5.2: Same as Figure 5.1 but for the pure-Si assumption.

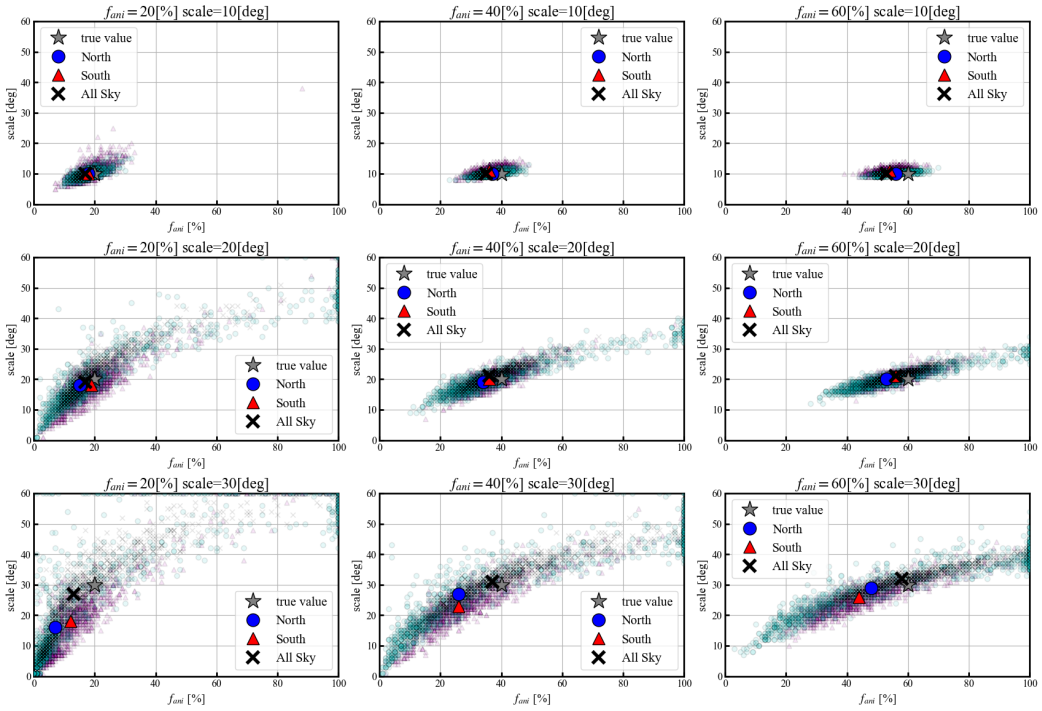

Figure 5.3: Same as Figure 5.1 but for the pure-Fe assumption.

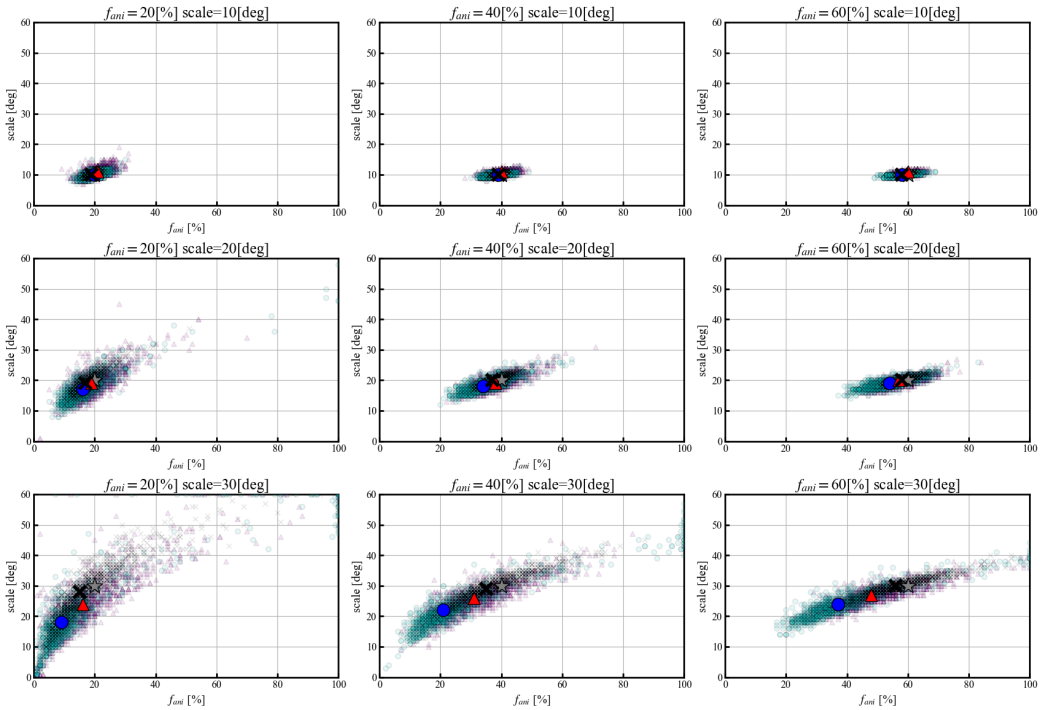

Figure 5.4: Same as Figure 5.1 but for the mixed-mass assumption.

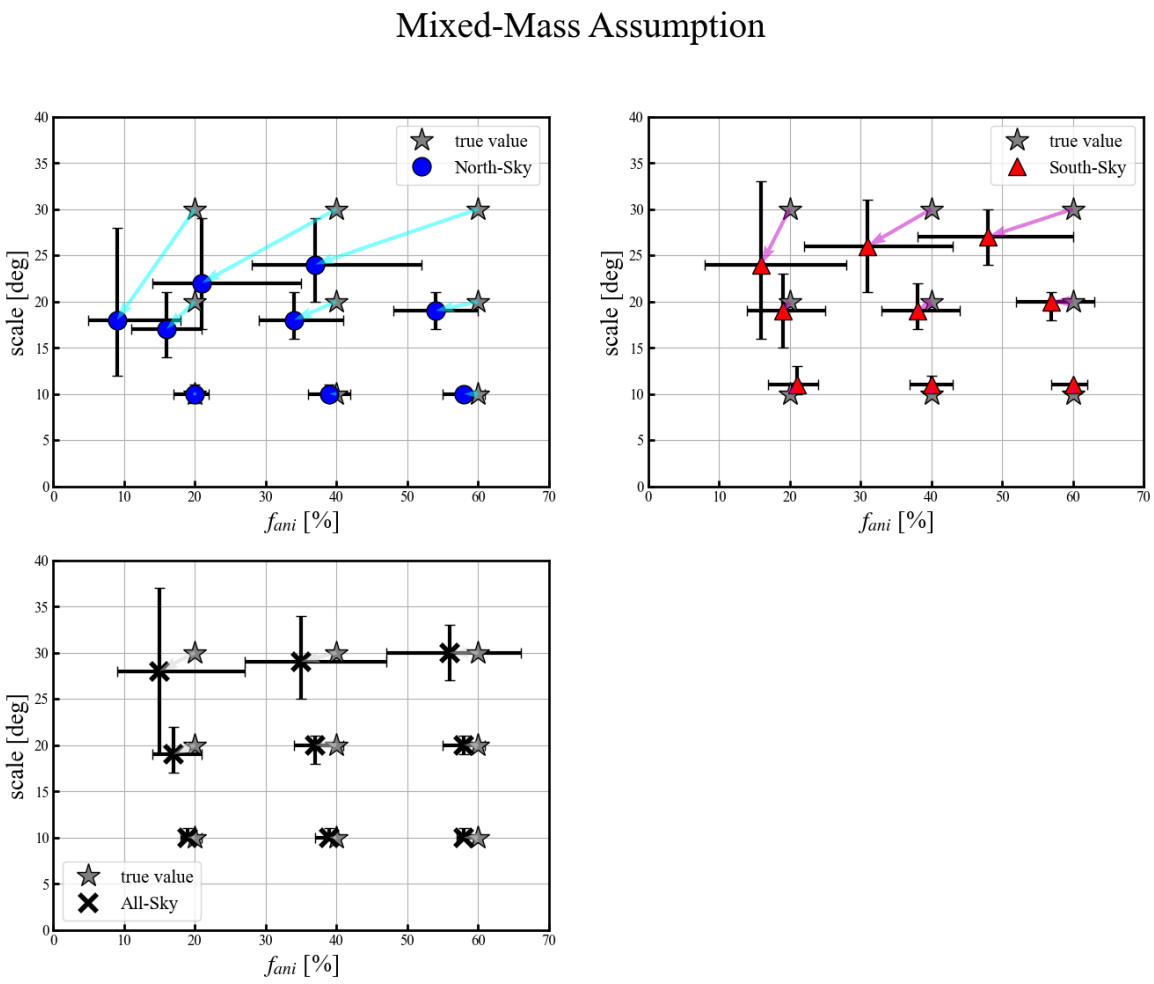

Figure 5.5: Same as Figure 4.14 but for the mixed-mass assumption in the new analysis method (method 1) shown in Figure 5.4. The top-left, top-right, and bottom panels show the offsets $(\Delta f_{\rm ani}^{\rm NEW}, \Delta\theta^{\rm NEW})$ of the median values in the north-sky, south-sky, and all-sky datasets, respectively. Black bars indicate the 68 percentile the median values.

Table 5.2: Offsets of mock UHECR datasets in the previous parameter estimations ($\Delta f_{\rm ani}, \Delta\theta$) and in the new technique ($\Delta f_{\rm ani}^{\rm NEW}, \Delta\theta^{\rm NEW}$)

true parameters		sky coverage	previous offset parameters		new offset parameters	
$f_{\rm ani}^{\rm true}$ [%]	$\theta^{\rm true}$ [deg]	—	$\Delta f_{\rm ani}$ [%]	$\Delta\theta$ [deg]	$\Delta f_{\rm ani}^{\rm NEW}$ [%]	$\Delta\theta^{\rm NEW}$ [deg]
20.0	10.0	All	$0.0^{+9.5}_{-9.5}$	$15.0^{5.0}_{-11.0}$	$-1.0^{+2.0}_{-1.0}$	$0.0^{+1.0}_{-0.0}$
		North	$-6.0^{+4.0}_{-3.0}$	$3.0^{+4.5}_{-2.5}$	$0.0^{+2.0}_{-3.0}$	$0.0^{+1.0}_{-1.0}$
		South	$-14.0^{+11.0}_{-5.0}$	$7.5^{+12.0}_{-10.5}$	$1.0^{+3.0}_{-4.0}$	$1.0^{+2.0}_{-1.0}$
20.0	20.0	All	$3.0^{+8.0}_{-8.0}$	$14.0^{+5.0}_{-5.0}$	$-3.0^{+4.0}_{-3.0}$	$-1.0^{+3.0}_{-2.0}$
		North	$1.0^{+23.0}_{-8.0}$	$10.0^{+9.0}_{-8.0}$	$-4.0^{+5.0}_{-5.0}$	$-3.0^{+4.0}_{-3.0}$
		South	$-15.0^{+15.0}_{-5.0}$	$1.0^{+11.0}_{-17.0}$	$-1.0^{+6.0}_{-5.0}$	$-1.0^{+4.0}_{-4.0}$
20.0	30.0	All	$-3.0^{+11.5}_{-6.5}$	$8.0^{+10.0}_{-8.0}$	$-5.0^{+12.0}_{-6.0}$	$-2.0^{+9.0}_{-9.0}$
		North	$-6.0^{+41.5}_{-9.5}$	$2.0^{+20.0}_{-14.0}$	$-11.0^{+9.0}_{-4.0}$	$-12.0^{+10.0}_{-6.0}$
		South	$-16.0^{+21.0}_{-3.0}$	$-9.0^{+24.0}_{-21.0}$	$-4.0^{+12.0}_{-8.0}$	$-6.0^{+9.0}_{-8.0}$
40.0	10.0	All	$0.0^{+8.0}_{-10.0}$	$16.0^{+3.0}_{-5.0}$	$-1.0^{+1.0}_{-2.0}$	$0.0^{+1.0}_{-0.0}$
		North	$-14.0^{+4.0}_{-3.0}$	$3.0^{+2.0}_{-1.0}$	$-1.0^{+3.0}_{-3.0}$	$0.0^{+1.0}_{-0.0}$
		South	$-23.0^{+8.0}_{-9.0}$	$12.0^{+3.5}_{-12.5}$	$0.0^{+3.0}_{-3.0}$	$1.0^{+1.0}_{-1.0}$
40.0	20.0	All	$3.0^{+8.0}_{-5.0}$	$13.0^{+3.0}_{-2.0}$	$-3.0^{+4.0}_{-3.0}$	$0.0^{+1.0}_{-2.0}$
		North	$1.0^{+16.5}_{-10.5}$	$10.0^{+4.0}_{-5.0}$	$-6.0^{+7.0}_{-5.0}$	$-2.0^{+3.0}_{-2.0}$
		South	$-26.0^{+10.0}_{-9.0}$	5.0^{+}_{-}	$-2.0^{+6.0}_{-5.0}$	$-1.0^{+3.0}_{-2.0}$
40.0	30.0	All	$-8.0^{+10.0}_{-6.0}$	$7.0^{+4.0}_{-3.0}$	$-5.0^{+12.0}_{-8.0}$	$-1.0^{+5.0}_{-4.0}$
		North	$-12.0^{+13.0}_{-10.0}$	$4.0^{+5.0}_{-7.0}$	$-19.0^{+14.0}_{-7.0}$	$-8.0^{+7.0}_{-5.0}$
		South	$-32.0^{+19.0}_{-4.0}$	$-5.0^{+11.0}_{-19.0}$	$-9.0^{+12.0}_{-9.0}$	$-4.0^{+5.0}_{-5.0}$
60.0	10.0	All	$-4.0^{+6.0}_{-8.0}$	$15.0^{+2.0}_{-3.0}$	$-2.0^{+2.0}_{-1.0}$	$0.0^{+1.0}_{-0.0}$
		North	$-22.0^{+3.0}_{-4.0}$	$3.0^{+1.0}_{-1.0}$	$-2.0^{+3.0}_{-3.0}$	$0.0^{+0.0}_{-0.0}$
		South	$-31.0^{+11.0}_{-12.0}$	$13.0^{+3.0}_{-9.0}$	$0.0^{+2.0}_{-3.0}$	$1.0^{+0.0}_{-1.0}$
60.0	20.0	All	$1.0^{+7.0}_{-5.0}$	$13.0^{+1.0}_{-2.0}$	$-2.0^{+3.0}_{-3.0}$	$0.0^{+1.0}_{-1.0}$
		North	$-1.0^{+9.0}_{-10.0}$	$10.0^{+2.5}_{-2.5}$	$-6.0^{+6.0}_{-6.0}$	$-1.0^{+2.0}_{-2.0}$
		South	$-38.0^{+7.0}_{-6.0}$	$6.0^{+3.0}_{-4.0}$	$-3.0^{+6.0}_{-5.0}$	$0.0^{+1.0}_{-2.0}$
60.0	30.0	All	$-13.0^{+8.5}_{-7.5}$	$7.0^{+3.0}_{-3.0}$	$-4.0^{+10.0}_{-9.0}$	$0.0^{+3.0}_{-3.0}$
		North	$-19.0^{+12.5}_{-11.5}$	$4.0^{+4.5}_{-3.5}$	$-23.0^{+15.0}_{-9.0}$	$-6.0^{+5.0}_{-4.0}$
		South	$-46.0^{+8.5}_{-12.5}$	$-3.0^{+5.0}_{-17.0}$	$-12.0^{+12.0}_{-10.0}$	$-3.0^{+3.0}_{-3.0}$

5.1.2 Uncertainties in the GMF model

To test the effects caused by the uncertainties in the GMF model, I conducted the same analysis in the same manner as in Section 5.1.1 but changing the GMF model.

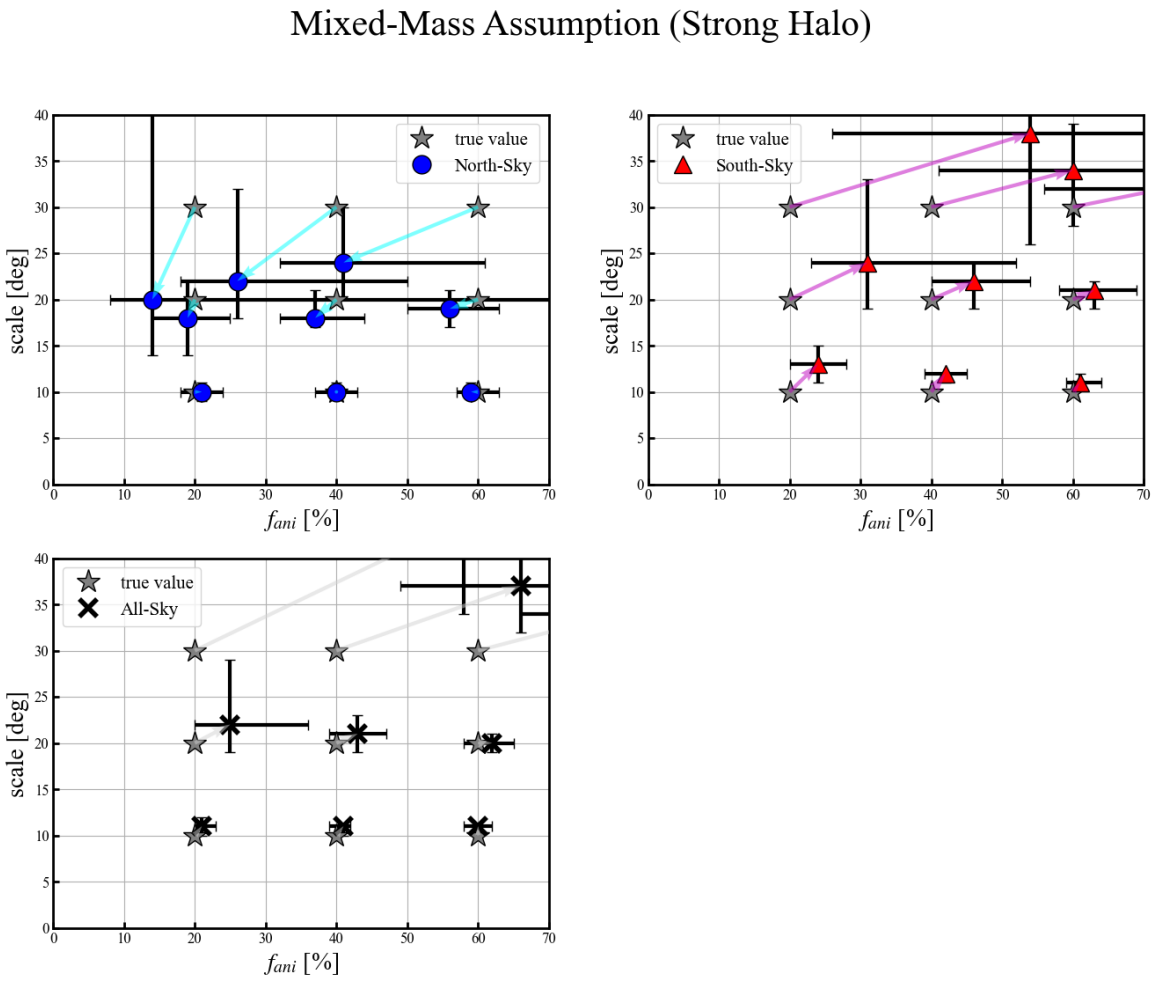

Figure 5.6: Same as Figure 4.14 but for the strong halo model in the new analysis Method 1. The mock datasets are the same as in Figure 5.5 which are generated with the original JF12 model. The parameters in this figure are estimated using the JF12 model whose halo components are stronger with 1σ uncertainty.

In the same manner as in Section 4.2.3, I changed the toroidal and X-halo components stronger/weaker within 1σ uncertainties (the strong halo model and weak halo model). I conducted the Method 1 analysis to the mock datasets (generated with the original JF12 model) with the strong halo model and weak halo model. Figures 5.6 and

5.7 show the results of the analysis with the strong halo model and the weak halo model, respectively. Even if the halo component in the JF12 model changes in 1σ uncertainty, the estimated parameters are within 68 percentile of the true parameters for a smaller separation angular scale. However, for a larger separation angular scale (ex. $\theta = 30\,\mathrm{deg}$), the estimated parameters cannot reproduce the true parameters. It suggests that the halo component of the GMF model affects the estimation, especially for the larger separation angular scale.

5.1.3 Independent test with the PT11 model

For an independent test of method 1, I conducted the same analysis as Section 5.1.1 only with the PT11 model. Different from Section 5.1.2, I applied Method 1 using the PT11 to the mock datasets generated with the PT11 model in Section 4.2.3. Same as the results with the JF12 model in Section 5.1.1, estimated parameters are consistent with the true parameters in 68 percentile.

5.2 Method 2: application of the new analysis method to the Auger and TA datasets

In this section, I will apply the new analysis method to the real observational datasets. In the current observational datasets, we do not know the mass A (charge Z) of each event. Thus, I modify Method 1 and apply it to the observational datasets (Method 2). In Method 2, I assume the probability of a mass of each event $p^A(E_{\mathrm{CR}}, Z^A_{\mathrm{CR}})$ and sum the model CR flux pattern F_{earth} weighted with the probability.

5.2.1 Application of the new analysis method to the real observational data (Method 2)

Based on the discussions in the previous sections, I consider the application of these methods to the actual data of the TA/Auger experiment. In the observational datasets, we cannot know the R_{CR} because we cannot determine the accurate value of the charge of CRs Z_{CR}. From the energy E_{CR}-dependent mass composition in

Equation 4.3, we derive the probability $p^A(E_{\rm CR}, Z^A_{\rm CR})$ that the charge of the UHECR event equals to $Z^A_{\rm CR}$:

$$p^A(E_{\rm CR}, Z^A_{\rm CR}) = \frac{J_A(E_{\rm CR})}{\sum_A J_A(E_{\rm CR})} \tag{5.4}$$

Here, J_A is combined-fit function from Equation 4.3 (Heinze & Fedynitch 2019). Because I assumed the nuclei ^{1}H, ^{4}He, ^{14}N, ^{28}Si, and ^{56}Fe, $Z^A_{\rm CR}$ is assumed to be $1, 2, 7, 14$, and 26. I assumed the rigidity of each event $R^A_{\rm CR} = E_{\rm CR}/Z^A_{\rm CR}e$ corresponding to each $Z^A_{\rm CR}$ and summed the flux $F_{\rm earth}(\mathbf{n}_{\rm CR}, \theta, R^A_{\rm CR})$ (derived in Equation 3.18 and $R^A_{\rm CR}$) with the weighted probability of $Z^A_{\rm CR}$: $p^A(E_{\rm CR}, Z^A_{\rm CR})$.

$$F_{\rm norm}(\mathbf{n}_{\rm CR}, f_{\rm ani}, \theta, R^A_{\rm CR}) = f_{\rm ani} \sum_A p^A(E_{\rm CR}, Z^A_{\rm CR}) F^{'}_{\rm earth}(\mathbf{n}_{\rm CR}, \theta, R^A_{\rm CR}) + (1 - f_{\rm ani}) F_{\rm iso}, \tag{5.5}$$

where $F^{'}_{\rm earth}$ and $F_{\rm iso}$ are shown as

$$F^{'}_{\rm earth} = \frac{F_{\rm earth}(\mathbf{n}_{\rm CR}, \theta, R^A_{\rm CR})}{\int_{4\pi} F_{\rm earth} d\Omega} \text{ and } F_{\rm iso} = 1/4\pi, \tag{5.6}$$

respectively. We substitute Equation 5.5 into Equation 3.5 and 3.4 to derive the TS.

5.2.2 Application of Method 2 to the mock UHECR datasets

Before applying the method discussed in Section 5.2.1 to the actual observational datasets, I applied it to the mock Auger 2015 and TA-11yr datasets from Section 4.2.4.

I present the results of the parameter estimations in Figure 5.9. As can be seen in Figure 5.4 for the larger statistical case, Method 2 can also reproduce the true values for the smaller separation angular scale θ. For the larger separation angular scale, the dispersion between the datasets becomes larger due to statistical uncertainties.

5.2.3 Application of Method 2 to the Auger 2015 and TA-11yr datasets

Figure 5.10 (5.11) shows the result of the application of the method discussed in Section 5.2.1 to the Auger 2015 (TA-11yr) dataset. The peak value of the TS for the Auger 2015 (TA-11yr) dataset is determined as $TS = 0.03$ (2.77). We cannot obtain an adequate TS value to support the SBG model with high significance. The best-fit parameters are calculated to be $(f_{\rm ani}, \theta) = (5\%, 34\,{\rm deg})$ $((f_{\rm ani}, \theta) = (3\%, 1\,{\rm deg}))$. Although the best-fit anisotropic fractions $f_{\rm ani}$ favor the isotropic model in both datasets, the small values of $TS_{\rm obs}$ need to be considered.

5.2.4 TS comparison using the mock datasets

Based on the values of the TS from the observational datasets $TS_{\rm obs}$ from Section 5.2.3, I compared the TS distribution of the mock datasets between the isotropic model and the SBG model in the same manner as has been done in Section 4.2.4. Figures 5.12 and 5.13 illustrate the TS of the observational dataset $TS_{\rm obs}$ and the TS distributions of the mock datasets derived using Method 2. The mock datasets are the same as those used in Sections 4.2.4 and 5.2.2. Compared to Figures 4.19 and 4.20, the separation of mock datasets between the isotropic and SBG models are improved. On the other hand, the observational test statistics $TS_{\rm obs}$ are consistent with the isotropic model.

5.3 Exclusion areas of $(f_{\rm ani}, \theta)$ in the SBG model

In Section 5.2.4, I could not obtain the $TS_{\rm obs}$ values to support the SBG model. Based on the application of Method 2 in Section 5.2.1, I calculated the exclusion areas of the parameters $(f_{\rm ani}, \theta)$.

The exclusion regions were estimated as follows:
The $TS_{\rm obs}$ for each parameter $(f_{\rm ani}, \theta)$ from the Auger 2015 and TA-11yr datasets were determined (Figures 5.10 and 5.11). For each parameters, I calculated the TS distribution of the mock Auger 2015 and TA-11yr datasets based on the SBG

model (Figures 5.12 and 5.13). I counted the number of mock datasets whose TS was smaller than that of the observational one ($TS < TS_{\rm obs}$) for each parameter set $(f_{\rm ani}, \theta)$. Figure 5.14 shows an example where $(f_{\rm ani}, \theta) = (60\%, 30\,{\rm deg})$ and the mock TA-11yr datasets. In this case, 98% of the TS are higher than those of the observational one ($TS > TS_{\rm obs}$).

In Figure 5.15, I have shown the percentages of the number of mock datasets whose TS was higher than that of the observational one. The black crosses in the same figure indicate the parameters $(f_{\rm ani}, \theta)$ that I tested, and the numbers show the percentage of datasets ($TS > TS_{\rm obs}$).

I excluded the parameter set $(f_{\rm ani}, \theta)$, whose percentage of datasets ($TS > TS_{\rm obs}$) exceeds 95%. Figure 5.16 displays the excluded areas of the SBG model from the Auger 2015 and TA-11yr datasets. From the observational datasets in this study, the gray regions exclude the SBG model.

5.4 Dependence on GMF models

In this section, I discuss the GMF model dependence in this Chapter. I estimated the effect of 1σ uncertainty of the JF12 model on the analysis in this chapter, using the strong/weak halo models in Sections 4.2.3 and 5.1.2. Figures 5.17 and 5.18 show the results of the analysis in Section 5.2.3 with the strong and weak halo models, respectively. Although TS values change, there are small differences in the 3σ contours. The anisotropic fraction $f_{\rm ani}$ also favors the isotropic model in both models. I conduct the Method 2 analysis using the strong/weak models for the same mock observational datasets in Section 5.2.4 and estimated the systematics of exclusion regions caused by the 1σ uncertainty of the JF12model in the same manner as Section 5.3.

5.5 Discussion for the SBG model

In Section 4.3, it was suggested that the anisotropy fraction was high when the SBG model was correct. On the other hand, Section 5.3 suggests that the expected area is rejected. In this section, I interpret these results.

The results are under a set of assumptions in the SBG model, GMF model, and mass composition (see Table 7.1 in Summary). I also note that the SBG model with a larger separation angular scale does not contradict the results in Section 5.3. For more physically-correct assumptions, we may need to consider the separation angular scale inversely proportional to rigidity for each particle.

If all parameter space for the SBG model is rejected, we may consider the correction for the source catalog and contribution of the SBG model or another steady source model. If any steady source model cannot explain the observed UHECRs (i. e. if $f_{\rm ani}$ remains small for any steady source candidates), we may consider the transient source models (Takami & Murase 2012).

5.6 Summary of this chapter

In this chapter, I developed a new technique for reducing the GMF bias. In this technique, I conduct the maximum likelihood method with the model CR flux patterns through the GMF, $F_{\rm earth}$, instead of those on the galaxy sphere $F_{\rm org}$ in previous parameter estimations.

First, I applied the analysis to the same mock datasets used in Chapter 4 with the assumption that the event-by-event mass A is known (Method 1, Section 5.2). In this case, the estimations are improved.

I evaluated the effect of uncertainties of the JF12 model using the strong/weak halo models in Section 4.2.3. The estimated parameters are the same as the true parameters in 68% tile for a smaller separation angular scale. On the other hand, for a larger separation angular scale (ex. $\theta = 30\,{\rm deg}$), the estimated parameters cannot reproduce the true parameters.

For an independent test of Method 1, I conducted the same analysis with the PT11 model for mock UHECR datasets generated based on the PT 11 model. Estimated parameters are consistent with the true parameters $(f_{\rm ani}^{\rm true}, \theta^{\rm true})$ in 68 percentile.

In the next step, I applied the analysis to the mock observational datasets and the observational datasets with the assumption that we do not know the mass A but know energies E (Method 2, Section 5.2.2 and 5.2.3). The effect of mass A is taken

into account in a probabilistic manner. I compared the TS distribution of the mock datasets with that of previous parameter estimations (Section 4.2.4) and suggested that the two models can be separated with a reduction in the GMF bias (Section 5.2.4). The $TS_{\rm obs}$ values taken from the Auger 2015 and TA-11yr datasets were consistent with the isotropic model for all the parameters that were tested ($f_{\rm ani}, \theta$) and inconsistent with the SBG model for certain parameter sets.

Based on the TS distribution, I estimated the 95% exclusion areas of the SBG model from the observational datasets (Section 5.3). This is the first study that constrains the source model from the observational datasets by considering the GMF bias.

I remind that the results are obtained under a set of models and assumptions which are summarized in Chapter 7.

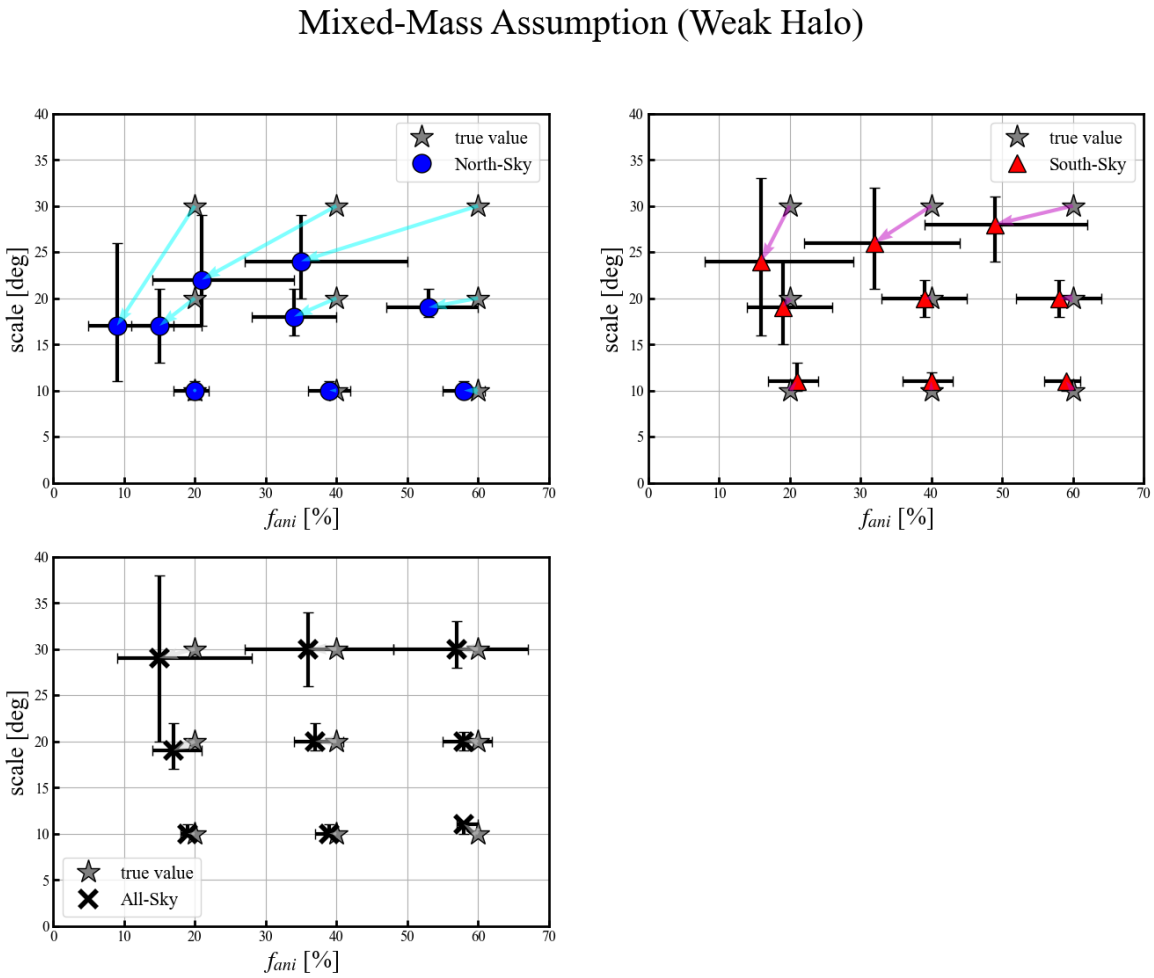

Figure 5.7: Same as Figure 4.14 but for the weak halo model in the new analysis Method 1. The mock datasets are the same as in Figure 5.5 which are generated with the original JF12 model. The parameters in this figure are estimated using the JF12 model whose halo components are weaker with 1σ uncertainty.

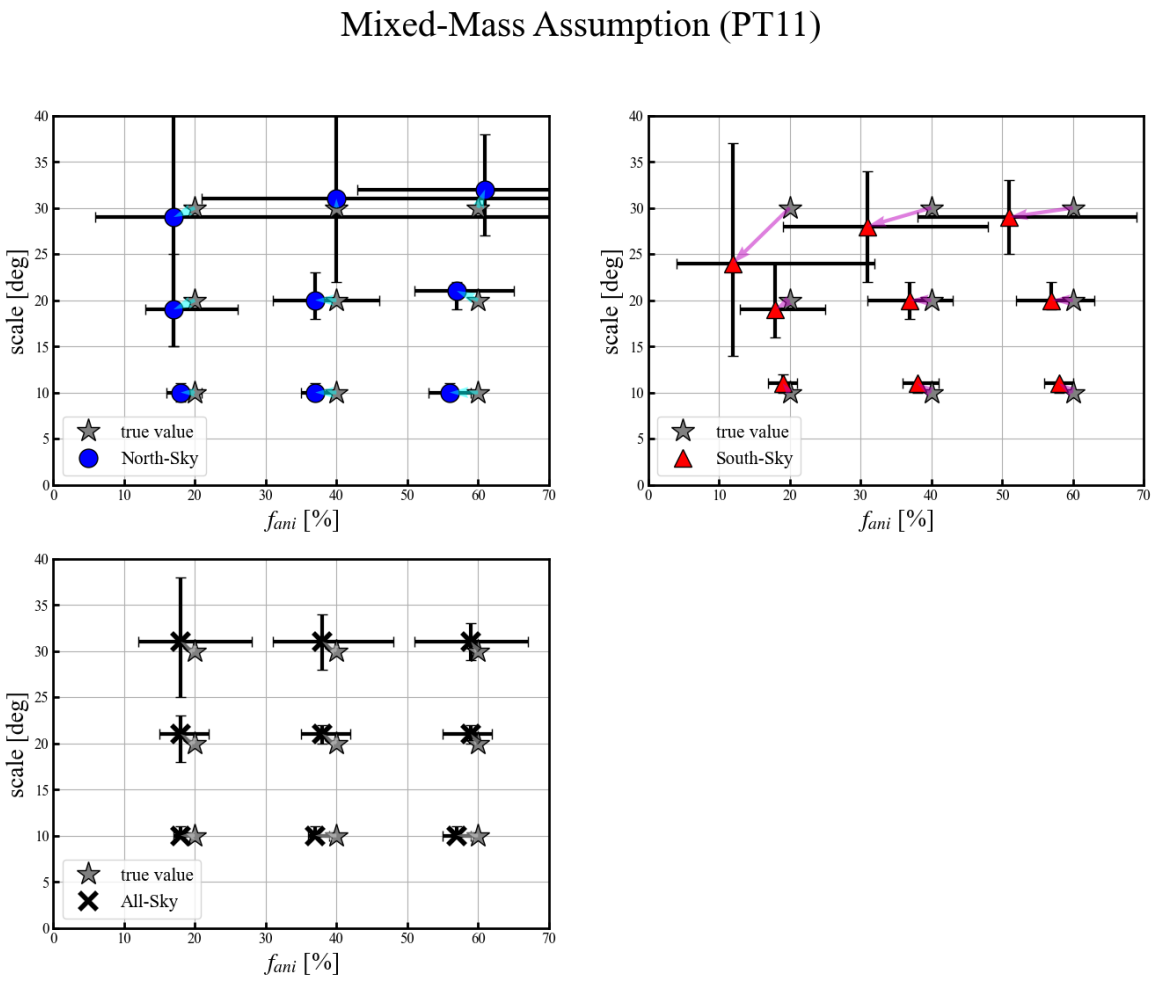

Figure 5.8: Same as Figure 4.14, but with the PT11 model. The mock datasets are the same as Figure 4.18 which are generated with the PT11 model. The parameters in this figure are estimated using the PT11 model, too.

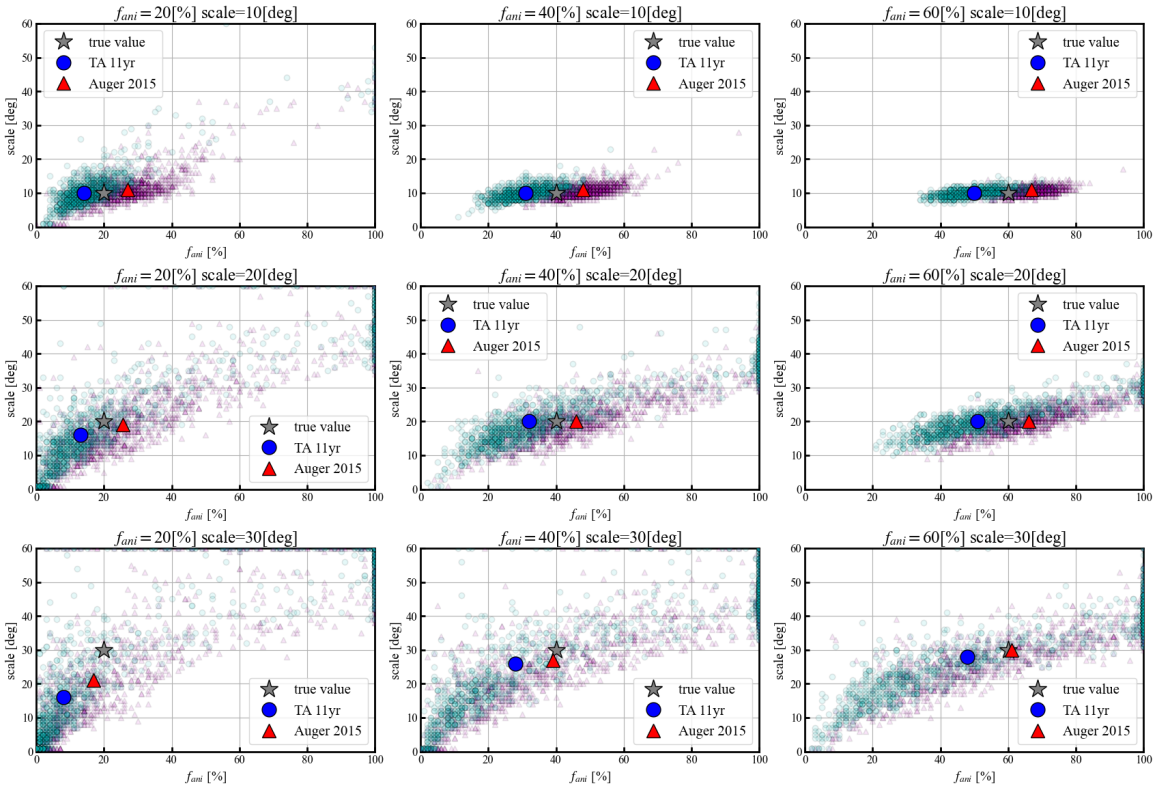

Figure 5.9: Distribution of the parameter estimation for the mock Auger 2015 and the mock TA-11yr datasets. The gray stars show the input parameters required to generate mock datasets. The magenta triangles (cyan circles) indicate the best-fit parameters of each dataset. The red triangle (blue circle) indicates the median value of the best-fit parameters.

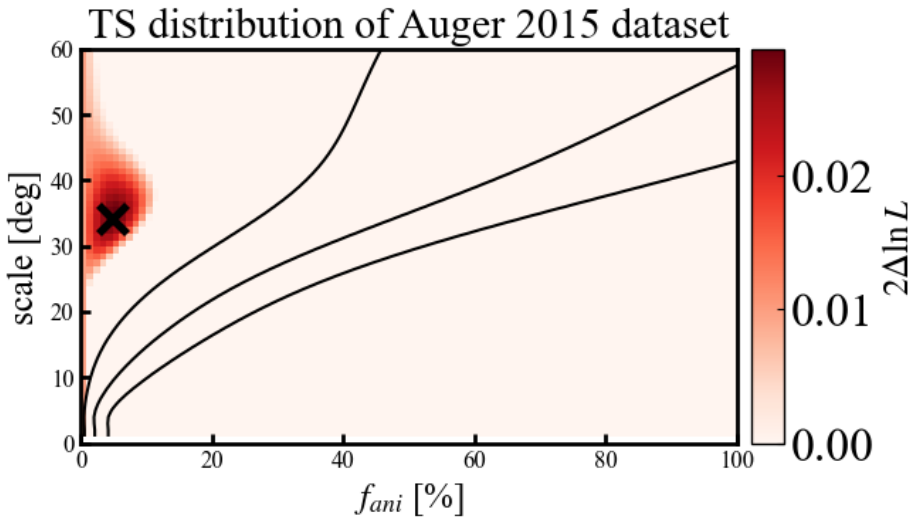

Figure 5.10: Result of the parameter estimation with the GMF bias for the Auger 2015 dataset. The black cross represents the best fit parameter of $(f_{\rm ani}, \theta) = (5\%, 34\,{\rm deg})$. The black contours indicate the confidence levels of 1–3σ.

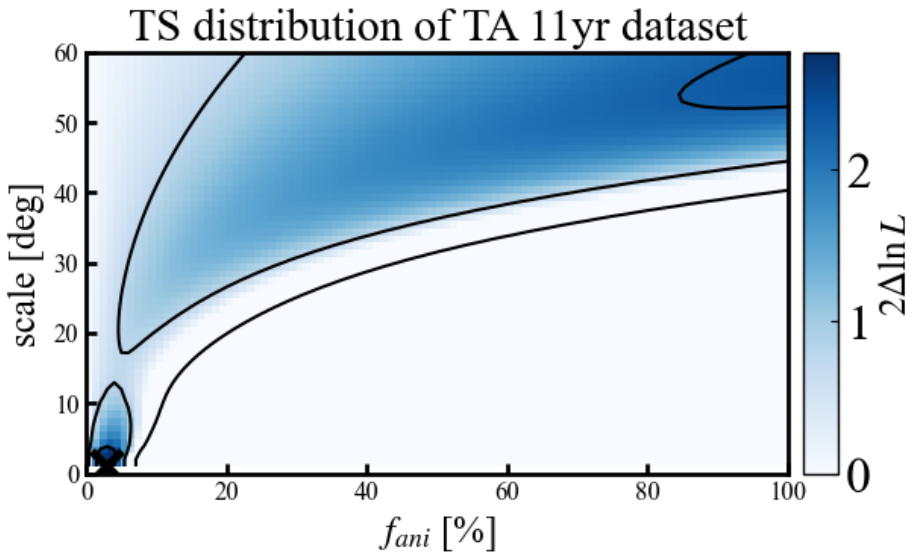

Figure 5.11: Same as Figure 5.10 but for the TA-11yr dataset. The black cross indicates the best-fit parameter of $(f_{\rm ani}, \theta) = (3\%, 1\,{\rm deg})$.

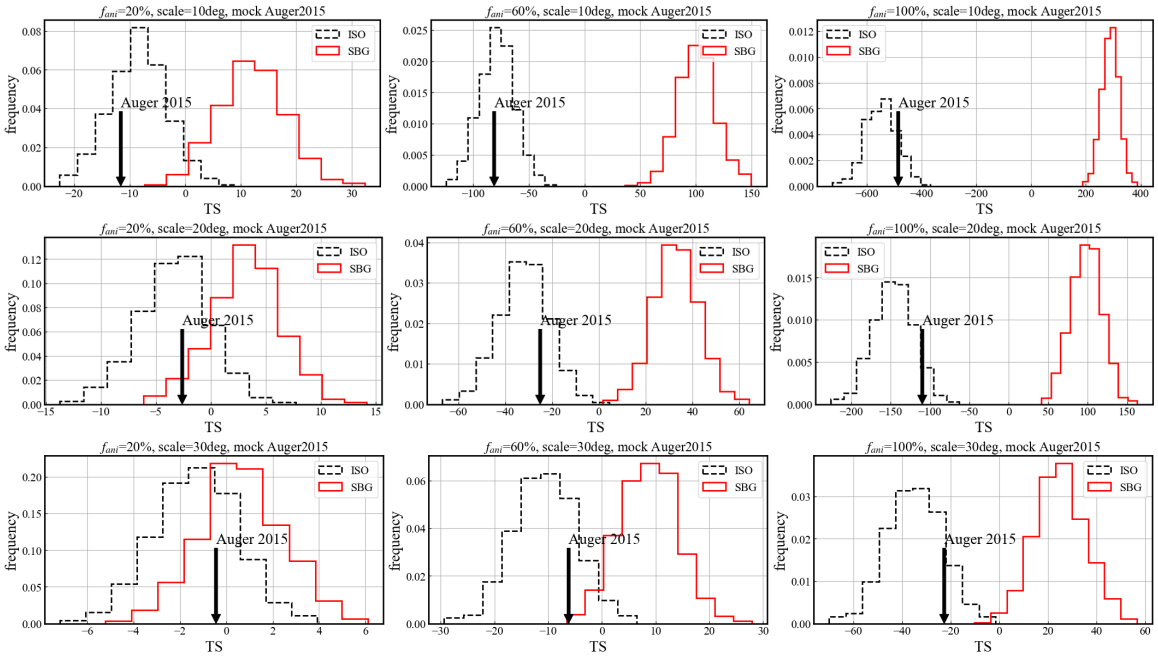

Figure 5.12: Same as Figure 4.19 but for the new parameter estimation with a reduction in the GMF bias (Method 2).

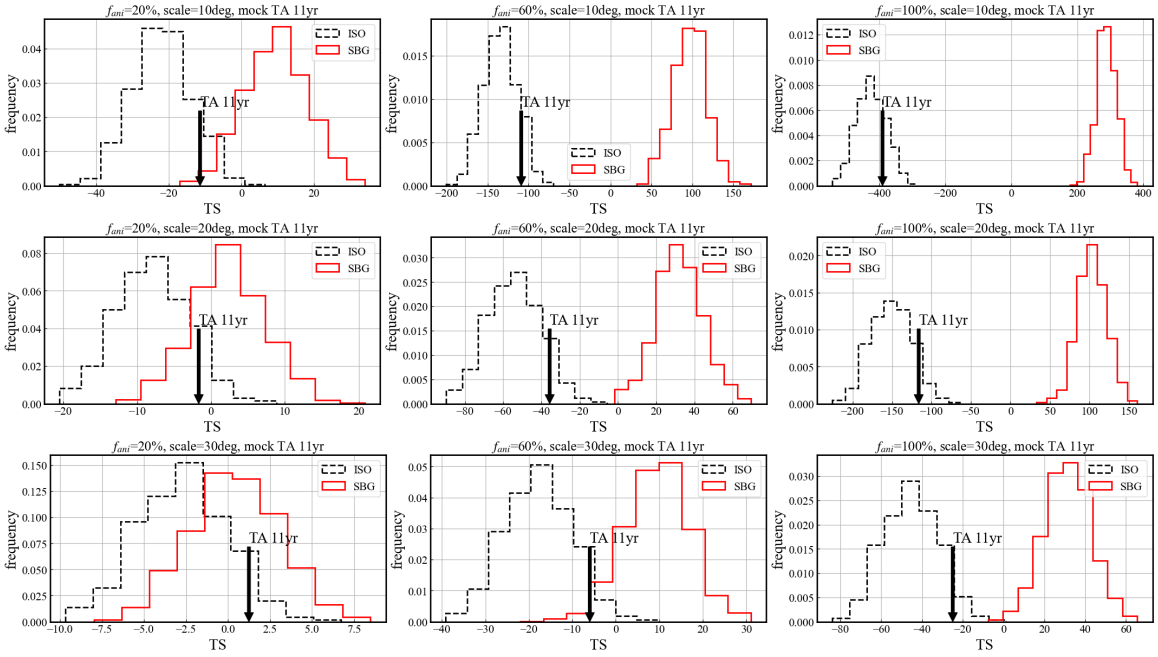

Figure 5.13: Same as Figure 5.12 but for the TA-11yr dataset with a reduction in the GMF bias (Method 2).

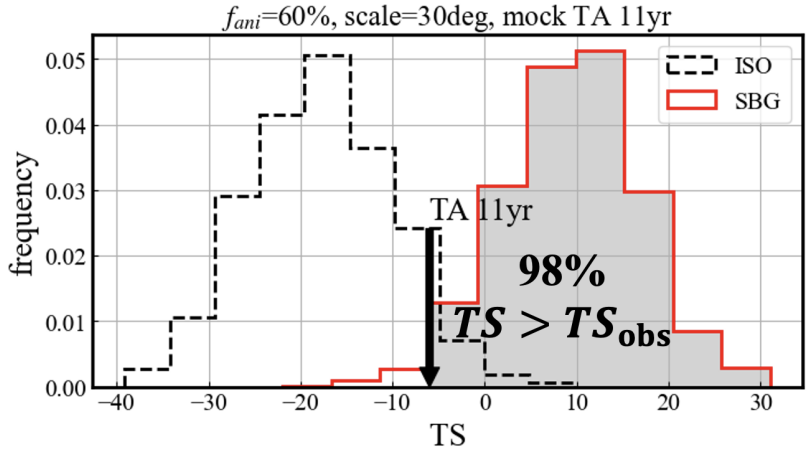

Figure 5.14: Example of an exclusion of datasets with the SBG model ($f_{\rm ani} = 60\%$, $\theta = 30$ deg, the mock TA-11yr dataset in this case). The red line shows the histogram of the TS values of the 1000 mock TA-11yr datasets with $(f_{\rm ani}, \theta)$=(60%, 30 deg) based on the SBG model. The light-gray region represents the datasets whose TS values exceed that of the TA 11-yr dataset (980 datasets).

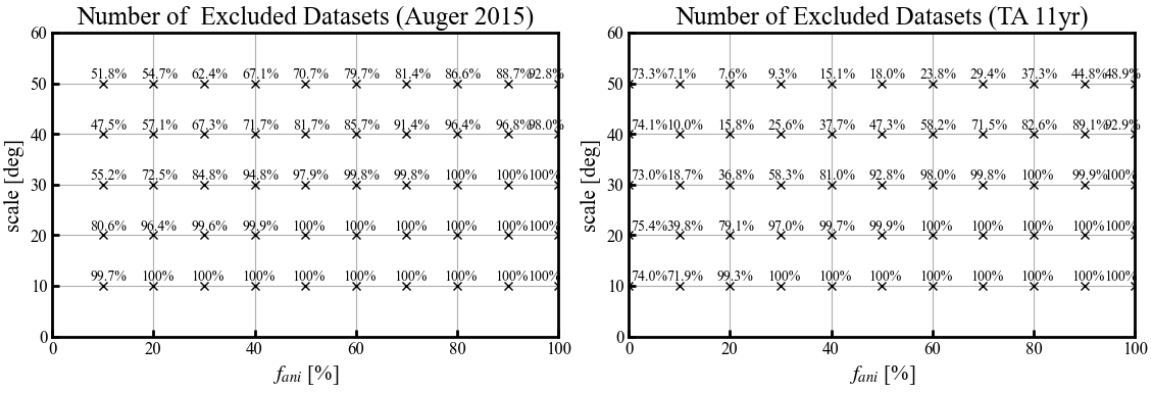

Figure 5.15: Number rates of the mock datasets with the SBG model whose TS value exceeds that of the observational dataset (left: the Auger 2015 dataset; right: the TA 11-yr dataset). The black crosses and numbers show the parameters $(f_{\rm ani}, \theta)$ and the number rates of datasets, respectively.

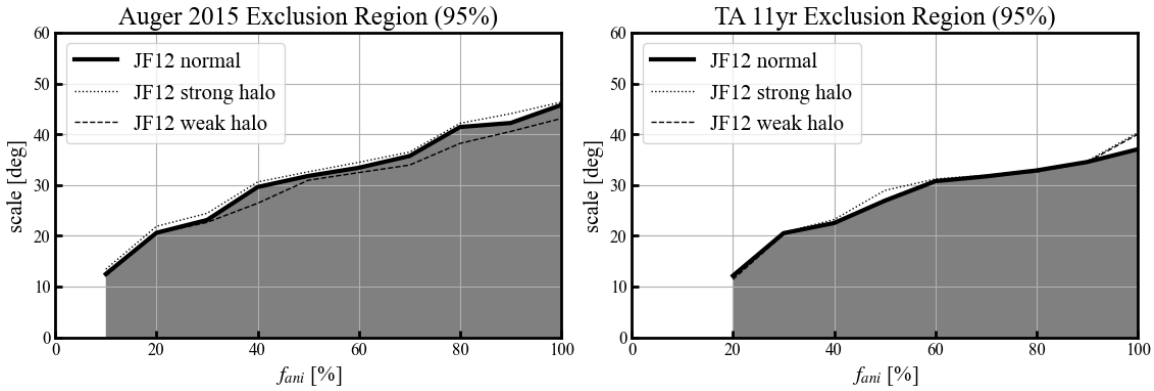

Figure 5.16: Exclusion area of the Auger 2015 dataset (left) and the TA-11yr dataset (right). The gray areas indicate the exclusion region with 95% CL. Black-solid, dotted and dashed lines show the exclusion regions derived with the original JF12 model, the strong halo model, and the weak halo model, respectively. The results are under a set of assumptions in the SBG model, GMF model, and mass composition (see text for detail).

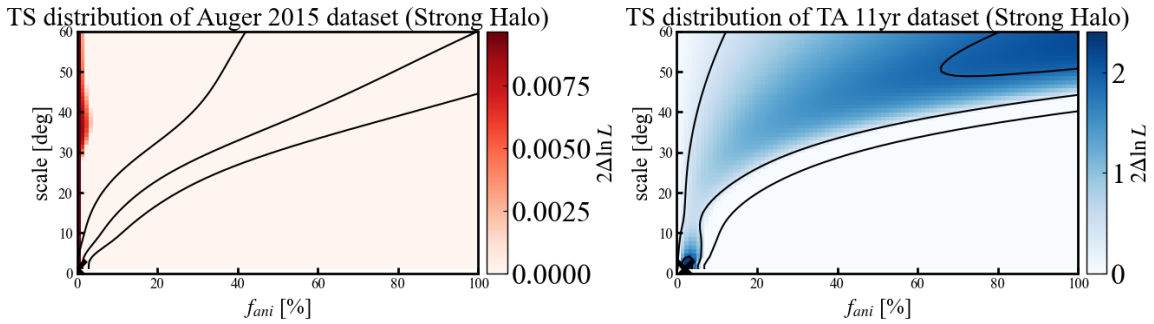

Figure 5.17: Left panel is same as Figure 5.12, but for the analyzed results with the strong halo model. Left panel is same as Figure 5.13, but for the analyzed results with the strong halo model.

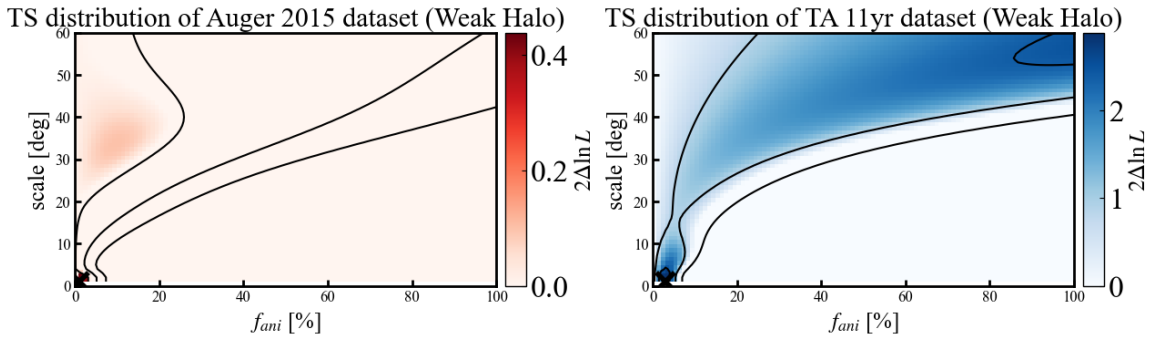

Figure 5.18: Same as Figure 5.17, but for the analyzed datasets with the weak halo model.

CHAPTER 6
DISCUSSION FOR THE FUTURE AND HIGH-RESOLUTION EXPERIMENTS

In addition to the TA and Auger experiments, UHECR observations with large statistics and high-mass resolutions are planned. In this chapter, I introduce the current representative plans for an UHECR observation in the 2020s and 2030s (Section 6.1).

From the perspective of future plans, I discuss the necessary statistics and mass resolution required to determine the source model of UHECRs (Section 6.2).

6.1 Future experiments

In this section, I will briefly summarize the future plans for UHECR observation with large statistics and high-mass resolutions.

6.1.1 Upgrades of the current experiments

The extension and upgrade for the TA and Auger experiments are ongoing as the TA×4 and AugerPrime experiments, respectively. These upgrades of the current experiments will provide us not only the larger statistics but also the science and technical requirements for the next-generation projects.

TA×4 experiment

As an extension of the TA experiment, the TA×4 experiment is ongoing (Abbasi et al. 2021a). In total, 500 SDs are placed at intervals of 2.08 km, and the total area covered would be 3000 km^2, including the area of the TA experiment (Figure 6.1). The TA×4 experiment started recording observations from 2019 using new 257 SDs, and the current effective area of the SDs is 2.5 times greater than that of the TA experiment.

The TA×4 experiment is expected to observe 384 events above 57 EeV by 2025 (Abbasi et al. 2021b).

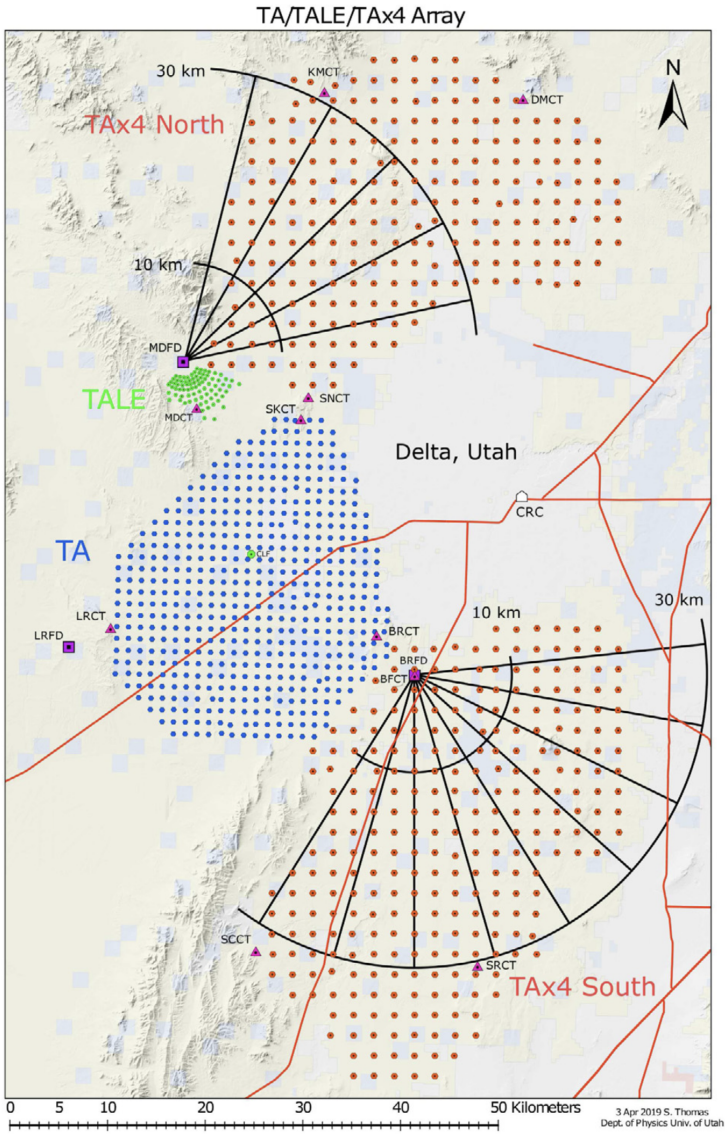

Figure 6.1: The layout of the TA×4 experiment, including the TA and TALE experiments (Abbasi et al. 2021a). The red, blue, and green markers show the position of the SDs of the TA×4, TA, and TALE experiments, respectively. The locations of the FDs in the TA and TA×4 experiments are shown by the magenta squares. The black lines indicate the FoV of the FDs in the TA×4 experiment.

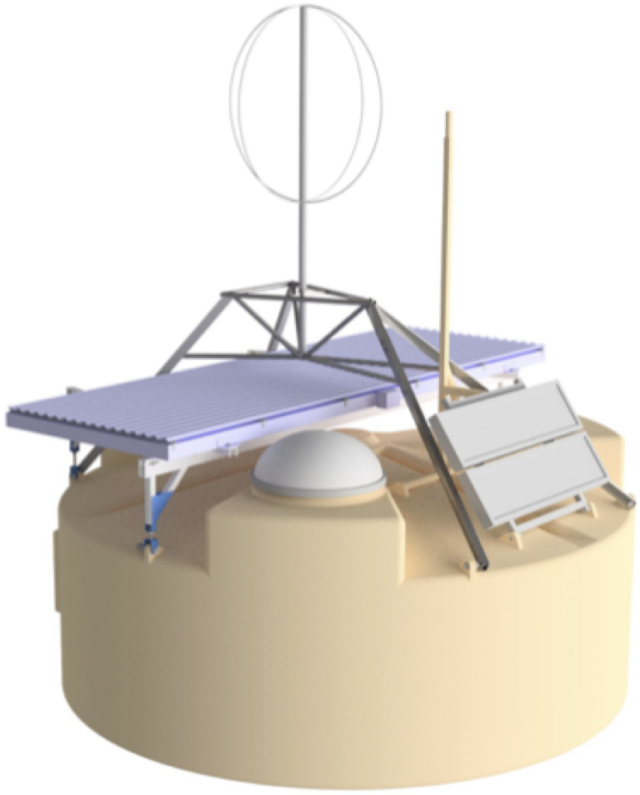

Figure 6.2: A design for an upgraded SD in the AugerPrime experiment (Figure 5 from Castellina & Pierre Auger Collaboration (2019)). A plastic scintillator similar to that of the TA experiment (Figure 2.5) is placed on the top of the existing water Cherenkov detector (Figure 2.7).

AugerPrime

AugerPrime (Castellina & Pierre Auger Collaboration 2019) is an upgraded version of the Auger experiment. In the AugerPrime experiment, a plastic scintillator will be placed on top of each SD station in addition to the existing water Cherenkov detector (Figure 6.2). The hybrid detection of the EAS with a plastic scintillator and a water Cherenkov detector will improve the sensitivity of the number count for muons and electrons, which leads us to a high-mass resolution UHECR observation with SDs. The full operation and observations are planned for 2020–2025.

6.1.2 Space telescope for a fluorescence light detection

To obtain a uniform and high exposure, it is an effective way to observe the fluorescence and Cherenkov lights of the EAS from space. Although the idea is proposed in the 1980s (Benson & Linsley 1981), it is still a challenging project today.

K-EUSO

The K-EUSO (Klimov & Casolino 2017) is a plan for placing a telescope on the Russian segment of the International Space Station (ISS). The K-EUSO experiment will observe the UHECRs whose energies are above 20 EeV with four times larger exposure than that in the Auger experiment. The launch of the K-EUSO is planned for 2022.

The Probe Of Extreme Multi-Messenger Astrophysics (POEMMA)

The Probe Of Extreme Multi-Messenger Astrophysics (POEMMA) is a project to observe the cosmic neutrinos above 20 PeV and the UHECRs whose energies are above 20 EeV (Olinto et al. 2019). In the POEMMA project, two identical satellites will conduct a stereo observation of UHECRs from the high altitude of 525 km (left panel in Figure 6.3). The POEMMA is expected to achieve the larger exposures for UHECRs by two orders of magnitudes than the TA/TA×4 and Auger experiments in the 2030s to 2040s (Olinto et al. 2021, Figure 6.3).

6.1.3 Future ground observations for UHECRs beyond the 2030s

With regard to the future prospects of astroparticle physics beyond the 2030s, the idea of the Global Cosmic Ray Observatory (GCOS) is being discussed (Hörandel 2021). The science and technical requirements are being discussed based on the current results from the TA and Auger experiments.

In workshops of GCOS, larger SD arrays and low-cost FD arrays are being discussed. For examples of low-cost FD arrays, technical tests for the CRAFFT and

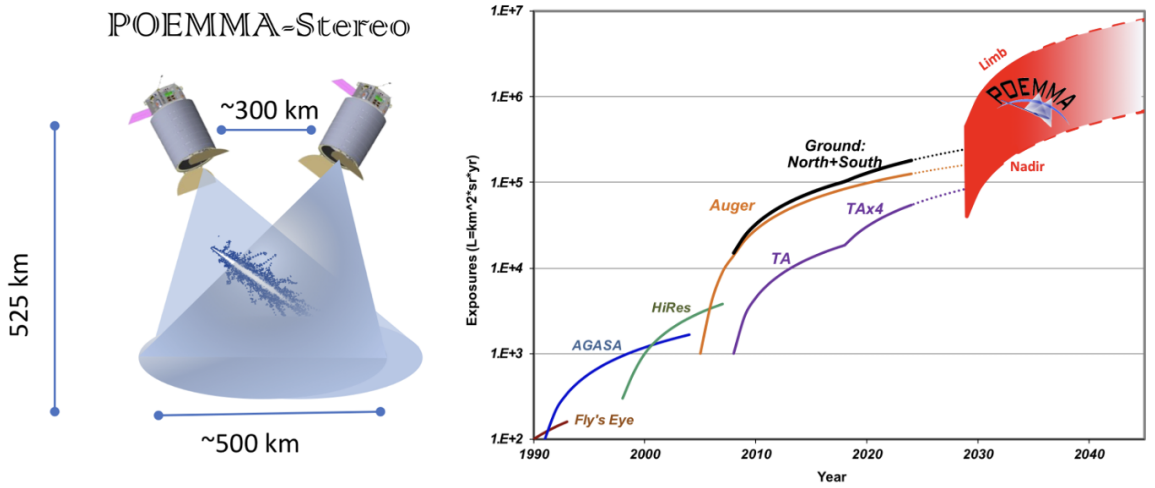

Figure 6.3: (Left) the stereo observation of UHECRs using the POEMMA (Figure 2 from Olinto et al. (2021)). (Right) the expected exposures obtained by the ground observations and the POEMMA (Figure 3 from Olinto et al. (2021)). Solid (dotted) lines show the exposures achieved (will be achieved by 2030) using the Fly's Eye, AGASA, HiRes, TA/TA×4, and Auger experiments. The red region indicates the expected exposure by the POEMMA.

FAST experiments are ongoing. The Cosmic Ray Air Fluorescence Fresnel lens Telescope (CRAFFT) is a future plan to build an FD array (Ikeda et al. 2020). Each FD will be made of 1 m^2 plastic Fresnel lens. The Fluorescence detector Array of Single-pixel Telescopes (FAST) is a next-generation UHECR observatory that consists of FD arrays (Malacari et al. 2020). These low-cost FD arrays are expected to achieve the event-by-event mass measurement of UHECRs.

6.2 Method 3: future prospects for large statistics and high-mass resolution experiments

In the previous chapter, I considered the methods that can be used to reduce the GMF bias in a maximum-likelihood analysis. We apply two methods depending on the constraints on the datasets.

Method 1: In an ideal case that all the mass A (charge Z) and energy E are known, we conduct an analysis with the rigidity dependence of the CR flux pattern (Section

5.1).

Method 2: In a realistic case where we do not know the event-by-event mass A but only know the energy E, we can sum the model CR flux pattern $F_{\rm earth}(R)$ with mass probability $p^A(E_{\rm CR}, Z^A_{\rm CR})$ and conduct the analysis (Section 5.2).

Methods 1 and 2 are extreme cases where we know all the event-by-event mass A and its energy E or we do not know mass A but only energies E.

As shown in Section 6.1, it is expected that future observations will enable us to observe large statistical observations and event-by-event mass estimation. In this section, I discuss the statistics that are required to achieve an event-by-event mass resolution $\Delta\ln(A) = \pm 10\%$–70% to separate the isotropic and SBG models. The reduction of the GMF bias needs to be applied with the assumption of the mass resolution (Method 3).

I conduct a maximum likelihood analysis on the same mock datasets used in Section 4.1 (mixed-mass composition and 1000/4000 events in all-sky). I carry out the analysis in the same manner as Method 1 (Section 5.2), but I randomly estimate the event-by-event mass A' with the uncertainty of the normal distribution ($\ln(A)$ with a standard deviation of $\Delta\ln(A)$). I assume a charge Z' of the event scaled to A'. I then calculate the event-by-event rigidity as $R' = E/Z'e$ and analyze it in the same manner as done in Method 1. Note that the estimated rigidity R' rarely obtains an extremely small (large) value due to the large fluctuation in the estimated charge Z'. In this case, I assume the event R' with $\log_{10}(R'/{\rm EV}) < 0.1$ ($\log_{10}(R'/{\rm EV}) > 3.0$) to be an event with $\log_{10}(R'/{\rm EV}) = 0.1$ ($\log_{10}(R'/{\rm EV}) = 3.0$). I set the true parameter as $(f^{\rm true}_{\rm ani}, \theta^{\rm true}) = (20\%, 30\,{\rm deg})$, which is in the allowed region of the Auger 2015 and TA-11yr constraints discussed in Section 5.2.3. To take statistical uncertainties into account, we assume the number of events to be 1000 and 4000 events all over the sky and analyze them as all-sky datasets.

The panels in Figure 6.4 show the TS distributions of the isotropic and SBG models with an assumption of the number of events $N = 1000/4000$ and mass resolution $\Delta\ln(A) = 0/10/30/50/70\%$. In any case, the higher mass resolution improves the separation of the TS distribution between the isotropic and SBG models. This

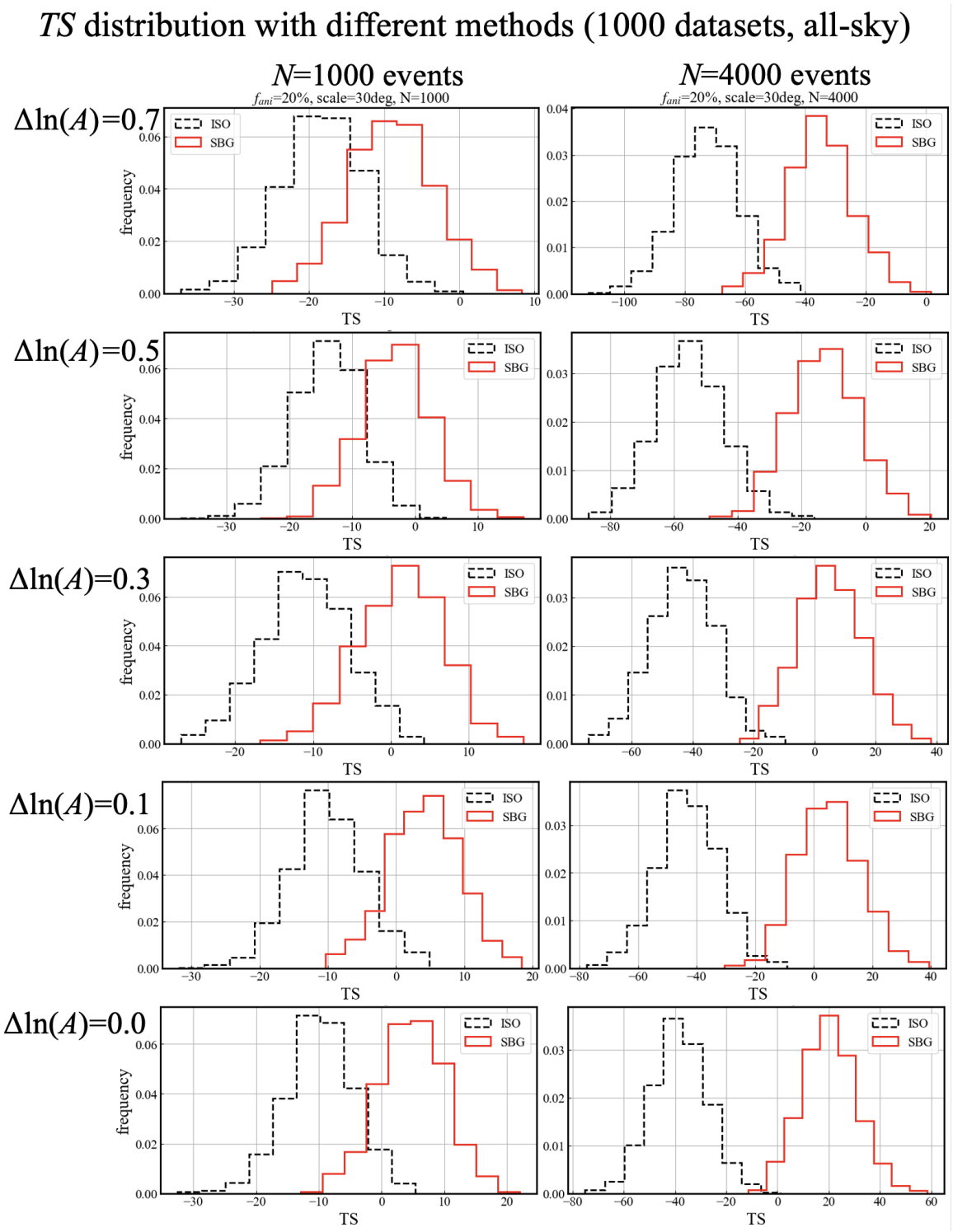

Figure 6.4: TS distributions of the all-sky mock UHECR datasets (left: 1000 events; right: 4000 events) in case with $(f_{\rm ani}^{\rm true}, \theta^{\rm true}) = (20\%, 30\,{\rm deg})$. From the top to bottom panels, the mass resolution is assumed to be $\Delta\ln(A) = 0.7$, 0.5, 0.3, 0.1, and 0.0. The TS distribution of the isotropic model and the SBG model is shown in black and red, respectively.

improvement is also seen from a comparison with the TS distributions for the same true parameters $(f_{\rm ani}^{\rm true}, \theta^{\rm true})$ in Figures 5.12 and 5.13. However, even if the number of events is $N = 1000$, we cannot separate the isotropic and SBG models even if we know all event-by-event mass A and the energy E ($\Delta\ln(A) = 0.0$). If the number of events is $N = 4000$, we can separate the models when the mass uncertainty is smaller ($\Delta\ln(A) < 0.3$). In this analysis, I concluded that we need more than 4000 events all sky and high-mass resolution with $\Delta\ln(A) < 0.3$ to separate the isotropic and SBG models at $(f_{\rm ani}^{\rm true}, \theta^{\rm true}) = (20\%, 30\,{\rm deg})$.

Note that I assumed all the anisotropic and isotropic events have the same mass composition in all analyses in this paper. At this moment we do not know whether the mass composition of the anisotropic events and that of the isotropic events are different. It is expected that the anisotropy of mass composition would be observed in future observations. Thus the higher event-by-event mass resolution observation will take an important role in future UHECR observations.

CHAPTER 7
SUMMARY

The UHECR anisotropies are suggested to correlate with the distribution of the UHECR sources. There are many studies that have investigated the association between the arrival directions of UHECR events and their source candidates. In a maximum-likelihood analysis in which an SBG source model is assumed, the Auger experiment derived the best-fit parameters of $(f_{\rm ani}, \theta) = (9.7\%, 12.9\,{\rm deg})$ and suggested that the nearby SBGs could be possible UHECR sources (Aab et al. 2018). The TA experiment also conducted the same analysis for UHECR events observed in the north sky and suggested that the result is consistent with the report obtained from the Auger experiment (Abbasi et al. 2018). These studies proposed that the SBG model is an interesting candidate for the source model of UHECRs.

In previous parameter estimations, however, the deflection by magnetic fields was approximated to a Gaussian-like scattering, and the coherent deflection caused by the structure of the GMF was not considered.

In this study, I investigated the bias created due to the coherent deflection by the GMF (the GMF bias) using a known GMF model. I also developed a new analysis technique to reduce the GMF bias and applied it to the observational datasets obtained through the Auger and TA experiments. To take the GMF bias into account, I considered the event-by-event energy E and the mass A (charge Z).

I generated the mock UHECR datasets with the assumptions in the source models, GMF model, energy spectrum, mass composition, and observation sites as summarized in Table 7.1.

Table 7.1: Assumptions for the generation of the mock UHECR datasets

topic	option	assumption	reference
source		the SBG model	Aab et al. (2018)
magnetic field	regular component of the GMF	the JF12 model	Jansson & Farrar (2012a,b)
	random component of the GMF	the Gaussian-like scattering	Fisher (1953)
	IGMF	the Gaussian-like scattering	Fisher (1953)
energy spectrum	pure-mass	a broken-power law broken at $E = 10^{19.81}$ eV[a]	Tsunesada et al. (2017)
	mixed-mass[b]	a product of a power law and exponential cutoff[c]	Heinze & Fedynitch (2019)
sky coverage	all-sky	independence on declinations	—
	north-sky	same as the TA experiment[d]	Sommers (2001)
	south-sky	same as the Auger experiment[e]	Sommers (2001)

[a] The spectrum is derived from the observational dataset obtained by the TA experiment (Tsunesada et al. 2017).

[b] A mass group (^{1}H, ^{4}He, ^{14}N, ^{28}Si, ^{56}Fe) is assumed.

[c] A combined-fit function for the observational dataset by the Auger experiment (Heinze & Fedynitch 2019). See also Equations 4.3 and 4.4.

[d] A latitude of an experiment $a_0 = 39.^{\circ}3$ and a maximum zenith angle $\theta_{\rm m} = 55^{\circ}$. See also Equations 3.6.

[e] A latitude of an experiment $a_0 = -35.^{\circ}2$ and a maximum zenith angle $\theta_{\rm m} = 60^{\circ}$. See also Equations 3.6.

For the mock UHECR datasets with assumptions in Table 7.1, I applied a maximum likelihood analysis with the SBG model in the same manner as Aab et al. (2018) and Abbasi et al. (2018).

I found that, in the previous parameter estimations of Aab et al. (2018) and Abbasi et al. (2018) the true value $(f_{\rm ani}^{\rm true}, \theta^{\rm true})$ cannot be correctly estimated. Particularly for the south-sky datasets, any true values of $f_{\rm ani}^{\rm true}$ reproduce the best-fit parameter reported in Aab et al. (2018). Even if the SBG model is correct, it is shown that we obtain an incorrect result when we ignore the coherent deflection caused by the GMF (the GMF bias). If we assume that the SBG model is correct, the true parameter $(f_{\rm ani}^{\rm true}, \theta^{\rm true})$ is estimated to be in a range of $(f_{\rm ani}, \theta) = (5\text{–}30\%, 5\text{–}30\,{\rm deg})$.

This tendency is the same when the halo component of the JF12 model increases or decreases in 1σ uncertainty, and an independent GMF model (the PT11 model) is used.

I also compared the TS distributions of the mock observational datasets (based on the isotropic and SBG source models) and the observational $TS_{\rm obs}$ in the same manner as Abbasi et al. (2018). In the current datasets and previous parameter estimation, I concluded that the separation between the isotropic models and SBG models is not as powerful as expected.

I developed a new technique to reduce the GMF bias that takes into consideration the CR flux patterns through the GMF. In this technique, I assume a dependence of the CR flux pattern on the rigidity of each UHECR event.

I used three new techniques to reduce the GMF bias based on the constraints of the datasets:

Method 1: In the ideal case where we know the mass A (charge Z) and energy E, we conduct an analysis with the rigidity dependence of the CR flux pattern (Section 5.1).

Method 2: In a realistic case where we do not know the event-by-event mass A and know only energy E, we sum the model CR flux pattern $F_{\rm earth}(R)$ with the mass probability $p^A(E_{\rm CR}, Z^A_{\rm CR})$ and conduct the analysis (Section 5.2).

Method 3: For future prospects, we conduct the analysis associated with Method 1 assuming that we know the event-by-event mass A with an uncertainty (Section 6.2 in Chapter 6).

Note that, for the new techniques, I used the same GMF model (JF12) as that used in the generation of the mock UHECR datasets (Table 7.1). To test the effect of the uncertainty of the GMF model used in the new techniques (Method 1), I conducted the same analysis for the same mock UHECR datasets, increasing and decreasing the halo component of the JF12 model. The estimated parameters are the same as the true parameters $(f_{\rm ani}^{\rm true}, \theta^{\rm true})$ in 68 percentile for a smaller separation angular scale. On the other hand, for a larger separation angular scale (ex. $\theta = 30\,{\rm deg}$), the estimated parameters cannot reproduce the true parameters. For an independent test of Method 1, I conducted the same analysis with the PT11 model for mock UHECR datasets generated based on the PT 11 model. Estimated parameters are consistent with the true parameters $(f_{\rm ani}^{\rm true}, \theta^{\rm true})$ in 68 percentile.

I also applied the same mixed mass assumption for Method 2 in Table 7.1. In both Methods 1 and 2, the all-sky parameter estimations with new techniques improve the offset of the GMF bias. I also applied Method 2 to the observational datasets (Auger 2015 and TA-11yr datasets). Although I searched the best-fit parameter $(f_{\rm ani}, \theta)$ to maximize the $TS_{\rm obs}$, I could not obtain the significant $TS_{\rm obs}$. By making a comparison with the TS distributions of the mock datasets from Method 2, I found that the new technique can determine the source models in a certain parameter space $(f_{\rm ani}^{\rm true}, \theta^{\rm true})$. Thus, I estimated the exclusion region of the SBG models of Aab et al. (2018) from the observational datasets obtained from the TA and Auger experiments. In this study, the large anisotropic fraction $f_{\rm ani}$ and small separation angular scale θ are excluded. This tendency is the same when the halo component of the JF12 model changes within 1σ uncertainties.

As for extensions of the TA and Auger experiments and next-generation plans, UHECR observations with large statistics and high-mass resolution are planned. For prospects, I execute the new technique with an assumption of a limited event-by-event mass resolution $\Delta\ln(A)$ (Method 3) and estimate the necessary number of events N

and mass resolution $\Delta\ln(A)$ to separate the isotropic and SBG models. I concluded that we need more than 4000 events all sky and high-mass resolution with $\Delta\ln(A) < 0.3$ to separate the isotropic and SBG models at $(f_{\rm ani}^{\rm true}, \theta^{\rm true}) = (20\%, 30\,{\rm deg})$.

Although this study is applied to a specific set of assumptions, the technique is applicable for any model and can be updated based on the future observations. Possible assumptions to be tested in the future are as follows:

- source model:
  - other source populations (ex. the AGN model in Aab et al. (2018))
  - assumption of different energy spectrum and mass composition for each source
- magnetic fields:
  - evaluation of random component of the GMF model
  - assumption of the IGMF
- energy spectrum and mass composition:
  - updated energy spectrum and mass composition values from the TA and Auger experiments

To improve the analysis of the datasets, we need to consider

- the all-sky parameter estimation instead of a separated analysis in the northern and southern hemispheres
- the difference in the mass composition between the anisotropic and isotropic UHECRs (the anisotropy of the mass composition).

For the all-sky dataset of UHECRs, it is important to consider the scaling of the reconstructed energies and the correction of the exposures in the TA and Auger experiments. For larger statistics, the extension of the TA and Auger experiments (TA×4 and AugerPrime) and next-generation UHECR observation will play an important role. Specifically, an event-by-event mass observation is important to investigate the

anisotropy of the mass composition. The techniques developed in this study and the future observations will reveal the origin of UHECRs.

ACKNOWLEDGMENTS

First, I want to thank my supervisor Sako Takashi for his support for my study. He spent a lot of time and effort not only on my research but also on presentations and my writing. I also thank my collaborators, Eiji Kido, Kazumasa Kawata, Toshihiro Fujii, Peter Tinyakov, Anatoli Fedynitch, and Noemie Globus for their discussions. I am grateful to all the members of the Telescope Array Collaboration.

This thesis was greatly improved with comments and suggestions by the referees: Katsuaki Asano, Masaki Ando, Takao Nakagawa Masahiro Teshima, and Junichi Yokoyama.

This study is supported by Research Fellowship for Young Scientists (DC2) organized by the Japan Society for the Promotion of Science.

My studies and life as Ph. D student did not be finished without supports from the staffs at the University of Tokyo. First I thank the staffs at ICRR, who always care about office procedures and encouragement for students and young scientists in ICRR. Especially in the hard times of the COVID-19 pandemic, my study and life have been supported by the efforts and kindness of the ICRR staffs and supporters. I also thank staffs at the Physics Department and the Disability Services Office of the University of Tokyo who supported and encouraged me to make reasonable accommodations for students with speech disorders (stuttering): from the entrance examination for the graduate school to Ph. D thesis defense. I am grateful to the staffs at the Student Support Office of the School of Science and the Health Service Counter at the University of Tokyo, too.

My residence in Tokyo during my Ph. D course is supported by Doumei-Gakuryo Dormitory (同盟学寮), which is established to support financially-difficult students who try to balance studying and working. From a certain point of view, my private hobbies encouraged me to continue my study in the hard times. I thank the STAR WARS series for always reminding me of my interest in the galaxy, far, far, away.

Lastly, I thank my friends and my family for their supports for my life in Tokyo. Especially, I thank my grandfather Akishige Okamoto, grandmother Kiyoko Okamoto, Junji Higuchi, and Miyuki Higuchi for the support and encouragement of my life.

REFERENCES

Aab, A., et al. 2015a, Nuclear Instruments and Methods in Physics Research, Section A: Accelerators, Spectrometers, Detectors and Associated Equipment, 798, 172

Aab, A., et al. 2015b, Astrophysical Journal, 804

Aab, A., et al. 2017, Phys. Rev. D, 96, 122003

Aab, A., et al. 2018, The Astrophysical Journal, 853, L29

Abbasi, R., et al. 2021a, Nuclear Instruments and Methods in Physics Research Section A: Accelerators, Spectrometers, Detectors and Associated Equipment, 165726

Abbasi, R., et al. 2021b, in Proceedings of 37th International Cosmic Ray Conference — PoS(ICRC2021), Vol. 395, 203

Abbasi, R. U., et al. 2014, Astrophysical Journal Letters, 790

Abbasi, R. U., et al. 2018, The Astrophysical Journal, 867, L27

Abbasi, R. U., et al. 2019, Phys. Rev. D, 99, 022002

Abbasi, R. U., et al. 2018, ApJ, 858, 76

Abbasi, R. U., et al. 2008, Phys. Rev. Lett., 100, 101101

Abbasi, R. U., et al. 2021c, Indications of a cosmic ray source in the perseus-pisces supercluster

Abbott, B. P., et al. 2017, The Astrophysical Journal, 848, L12

Abreu, P., Aglietta, M., & Aguirre, C. 2007, Science, 318, 938

Abreu, P., et al. 2012, Astrophysical Journal, Supplement Series, 203

Abreu, P., et al. 2010, Astroparticle Physics, 34, 314

Abu-Zayyad, T., et al. 2012, Nuclear Instruments and Methods in Physics Research A, 689, 87

Abu-Zayyad, T., et al. 2013, ApJ, 768, L1

Ackermann, M., et al. 2012, Astrophysical Journal, 755

Ackermann, M., et al. 2016, ApJS, 222, 5

Ahlers, M. 2014, Phys. Rev. Lett., 112, 021101

Anchordoqui, L. A. 2019, Physics Reports, 801, 1

Anjos, R. C. D., et al. 2018, Physical Review D, 98, 123018

Attallah, R., & Bouchachi, D. 2018, Monthly Notices of the Royal Astronomical Society, 478, 800

Batista, R. A., et al. 2019, Frontiers in Astronomy and Space Sciences, 6, 1

Batista, R. A., et al. 2016, Journal of Cosmology and Astroparticle Physics, 2016

Beck, R. 2009, Astrophysics and Space Science, 320, 77

Bellido, J., & Pierre Auger Collaboration. 2017, in International Cosmic Ray Conference, Vol. 301, 35th International Cosmic Ray Conference (ICRC2017), 506

Benson, R., & Linsley, J. 1981, in International Cosmic Ray Conference, Vol. 8, International Cosmic Ray Conference, 145

Berezinsky, V., Blasi, P., & Vilenkin, A. 1998, Phys. Rev. D, 58, 103515

Bird, D. J., et al. 1995, ApJ, 441, 144

Bradt, H., & Olbert, S. 2008, p. 1

Castellina, A., & Pierre Auger Collaboration. 2019, in European Physical Journal Web of Conferences, Vol. 210, European Physical Journal Web of Conferences, 06002

Coleman, S., & Glashow, S. L. 1999, Phys. Rev. D, 59, 116008

Cordes, J. M., & Chatterjee, S. 2019, Annual Review of Astronomy and Astrophysics, 57, 417

Cordes, J. M., & Lazio, T. J. W. 2002, arXiv e-prints, astro

di Matteo, A., et al. 2020, arXiv e-prints, arXiv:2001.01864

Durrer, R., & Neronov, A. 2013, Astronomy and Astrophysics Review, 21

Fang, K., Fujii, T., Linden, T., & Olinto, A. V. 2014, ApJ, 794, 126

Fang, K., & Murase, K. 2018, Nature Physics, 14, 396

Fang, K., & Olinto, A. V. 2016, ApJ, 828, 37

Fargion, D., Mele, B., & Salis, A. 1999, The Astrophysical Journal, 517, 725

Farrar, G. R. 2014, The galactic magnetic field and ultrahigh-energy cosmic ray deflections

Fermi, E. 1949, Phys. Rev., 75, 1169

Fisher, R. 1953, Dispersion on a sphere

Frail, D. A., Kulkarni, S. R., & Bloom, J. S. 1999, Nature, 398, 127

Gaisser, T. K., Engel, R., & Resconi, E. 2016, Cosmic Rays and Particle Physics (2 ed.) (Cambridge University Press)

Gold, B., et al. 2011, Astrophysical Journal, Supplement Series, 192

Greisen, K. 1966, Physical Review Letters, 16, 748

Grupen, C. 2013, Nuclear Physics B - Proceedings Supplements, 239-240, 19, Proceedings of the 9th workshop on Science with the New Generation of High Energy Gamma-ray Experiments: From high energy gamma sources to cosmic rays, one century after their discovery

Grupen, C. 2020, Astroparticle Physics (2 ed.), Undergraduate Texts in Physics (Springer, Cham)

Hayashida, M., et al. 2013, ApJ, 779, 131

Hayashida, N., et al. 1994, Phys. Rev. Lett., 73, 3491

He, H. N., Kusenko, A., Nagataki, S., Zhang, B. B., Yang, R. Z., & Fan, Y. Z. 2016, Physical Review D, 93, 1

Heck, D., Knapp, J., Capdevielle, J. N., Schatz, G., & Thouw, T. 1998, CORSIKA: a Monte Carlo code to simulate extensive air showers.

Heinze, J., & Fedynitch, A. 2019, The Astrophysical Journal, 873, 88

Hillas, A. M. 1984, ARA&A, 22, 425

Hörandel, J. R. 2021, Proceedings of 37th International Cosmic Ray Conference — PoS(ICRC2021), 395, 027

IceCube Collaboration, et al. 2018, Science, 361, eaat1378

Ikeda, D., Tameda, Y., Tomida, T., Yamazaki, K., Yamamoto, M., Iwakura, H., Nakamura, Y., & Kaino, Y. 2020, in Journal of Physics Conference Series, Vol. 1468, Journal of Physics Conference Series, 012079

Ivanov, D. 2017, Proceedings of Science, 0

Ivanov, D. 2019, in Proceedings of 36th International Cosmic Ray Conference — PoS(ICRC2019), Vol. 358, 298

Jansson, R., & Farrar, G. R. 2012a, Astrophysical Journal, 757

Jansson, R., & Farrar, G. R. 2012b, Astrophysical Journal Letters, 761, 1

Kawai, H., et al. 2008, Nuclear Physics B Proceedings Supplements, 175, 221

Kawata, K., et al. 2019, in International Cosmic Ray Conference, Vol. 36, 36th International Cosmic Ray Conference (ICRC2019), 310

Klein, U., & Fletcher, A. 2015, Galactic and Intergalactic Magnetic Fields (1 ed.), Springer Praxis Books (Springer, Cham)

Klimov, P., & Casolino, M. 2017, PoS, ICRC2017, 412

Krause, M. 2009, in Revista Mexicana de Astronomia y Astrofisica Conference Series, Vol. 36, Revista Mexicana de Astronomia y Astrofisica Conference Series, 25

Kronberg, P. P., & Newton-McGee, K. J. 2011, Publications of the Astronomical Society of Australia, 28, 171

Kuznetsov, M., & Tinyakov, P. 2021, Journal of Cosmology and Astroparticle Physics, 2021, 065

Letessier-Selvon, A., & Stanev, T. 2011, Reviews of Modern Physics, 83, 907

López-Barquero, V., Farber, R., Xu, S., Desiati, P., & Lazarian, A., 830, 19

Lorimer, D. R., Bailes, M., McLaughlin, M. A., Narkevic, D. J., & Crawford, F. 2007, Science, 318, 777

Malacari, M., et al. 2020, Astroparticle Physics, 119, 102430

Ogio, S. 2018, Telescope Array Low energy Extension: TALE, JPS Conference Proceedings (Journal of the Physical Society of Japan)

Ogio, S., Tsunesada, Y., & Sagawa, H. 2019, RADIOISOTOPES, 68, 843

Olinto, A., et al. 2021, Journal of Cosmology and Astroparticle Physics, 2021, 007

Olinto, A. V., Adams, J., Aloisio, R., Anchordoqui, L., Bergman, D., & Bertaina, M. 2019, in International Cosmic Ray Conference, Vol. 36, 36th International Cosmic Ray Conference (ICRC2019), 378

Peng, F.-K., Wang, X.-Y., Liu, R.-Y., Tang, Q.-W., & Wang, J.-F. 2016, ApJ, 821, L20

Pshirkov, M. S., Tinyakov, P. G., Kronberg, P. P., & Newton-McGee, K. J. 2011, ApJ, 738, 192

Rouillé d'Orfeuil, B., Allard, D., Lachaud, C., Parizot, E., Blaksley, C., & Nagataki, S. 2014, A&A, 567, A81

Sagawa, H. 2020, Journal of Instrumentation, 15, C09012

Sokolsky, P., & Thomson, G. 2020, Introduction to ultrahigh energy cosmic ray physics (2nd ed ed.), Frontiers in physics (CRC Press)

Sommers, P. 2001, Astroparticle Physics, 14, 271

Soriano, J. F., Anchordoqui, L. A., & Torres, D. F. 2019, arXiv e-prints, arXiv:1907.06207

Stecker, F. W. 2003, Journal of Physics G Nuclear Physics, 29, R47

Sun, X.-H., & Reich, W. 2010, Research in Astronomy and Astrophysics, 10, 1287

Sun, X. H., Reich, W., Waelkens, A., & Enßlin, T. A. 2008, A&A, 477, 573

Supanitsky, A., & Medina-Tanco, G. 2019, Journal of Cosmology and Astroparticle Physics, 2019, 036

Swordy, S. P. 2001, Space Sci. Rev., 99, 85

Takami, H., & Murase, K. 2012, The Astrophysical Journal, 748, 9

Takeda, M., et al. 1998, Phys. Rev. Lett., 81, 1163

Tang, Q.-W., Wang, X.-Y., & Tam, P.-H. T. 2014, ApJ, 794, 26

Taylor, A. R., Stil, J. M., & Sunstrum, C. 2009, The Astrophysical Journal, 702, 1230

The Pierre Auger Collaboration, et al. 2016, arXiv e-prints, arXiv:1604.03637

Tinyakov, P. G., & Tkachev, I. I. 2001, Journal of Experimental and Theoretical Physics Letters, 74, 1

Tokuno, H., et al. 2012, Nuclear Instruments and Methods in Physics Research A, 676, 54

Tsunesada, Y., AbuZayyad, T., Ivanov, D., Thomson, G., Fujii, T., & Ikeda, D. 2017, in International Cosmic Ray Conference, Vol. 301, 35th International Cosmic Ray Conference (ICRC2017), 535

van Vliet, A., Palladino, A., Taylor, A., & Winter, W. 2021, Monthly Notices of the Royal Astronomical Society, 510, 1289

Zatsepin, G. T., & Kuz'min, V. A. 1966, Soviet Journal of Experimental and Theoretical Physics Letters, 4, 78

Zhang, B. T., & Murase, K. 2019, Phys. Rev. D, 100, 103004

Zhang, B. T., Murase, K., Kimura, S. S., Horiuchi, S., & Mészáros, P. 2018, Physical Review D, 97